AUTOMATIC DIGITAL HOLOGRAPHIC ANALYSIS OF NEAR-FIELD AERATED LIQUID JETS IN CROSSFLOW

By
DAVID S. OLINGER

Master of Science
Oklahoma State University
Stillwater, Oklahoma
2004

Bachelor of Science
Colorado State University
Fort Collins, Colorado
2002

Submitted to the Faculty of the
Graduate College of the
Oklahoma State University
in partial fulfillment of
the requirements for
the Degree of
DOCTOR OF PHILOSOPHY
May, 2012

AUTOMATIC DIGITAL HOLOGRAPHIC ANALYSIS OF NEAR FIELD AERATED LIQUID JETS IN CROSSFLOW

Dissertation Approved:

Khaled Sallam

Dissertation Adviser

Andy Arena

Qi Cheng

Jay Hanan

L.L. Hoberock

Sheryl A. Tucker

Dean of the Graduate College

Table of Contents

List of Tables

List of Figures

Nomenclature

d = diameter, in context of drop or injector

A = area

GLR = aerating gas-to-liquid mass flow rate ratio

M = Mach number in relation to flow conditions or magnification factor in relation to optics

q = Momentum flux ratio, $(\rho v^2)_{jet}/(\rho v^2)_\infty$

ρ = density

x = downstream or streamwise coordinate

y = vertical coordinate

z = spanwise coordinate (distance normal to image plane)

u = velocity component in x direction

v = velocity component in y direction

w = velocity component in z direction

t, *t* = time

SMD = Sauter Mean Diameter, mass averaged diameter

$\tilde{u}$ = mass averaged velocity in x direction

$\tilde{v}$ = mass averaged velocity in y direction

Δx = difference in two x values

TP = true positive detection rate (%) of the algorithm to find drops within a hologram

FP = false positive detection rate (%) of the algorithm to find drops within a hologram

ε = uncertainty

$\langle x \rangle$ = spatially averaged x data points

Subscripts

Jet, j = the physical property referring to the liquid jet in the experiment

∞ = the physical property referring to the air (crossflow) in the wind tunnel

d = number of diameters

Chapter I. Background and Introduction

1.1 Introduction

Liquid sprays are an active area of interest in multi-phase fluids research. Increasingly stringent mandates on fuel efficiency and emissions are driving improvements in traditional fuel injection applications. Advanced aerospace propulsion technology and national defense initiatives further the demand for knowledge of spray physics. Aerated liquid (AKA barbatoge or effervescent) jets (see Sovani et al., 2001) are a possibility for ramjets and scramjets because of their excellent mixing potential (Lin et al., 1999 and 2002). This class of injector is further explored in the Experimental Results Chapter. Experimental data is required for design engineers, numerical modelers, and physicists alike. Unfortunately, existing diagnostic methods are unable to satisfactorily map the flow field near the injector. This "near field" is critical to spray atomization, as all downstream characteristics are governed by the primary and secondary breakup mechanisms that dominate the near field, namely, droplet size, three dimensional droplet distribution, and corresponding droplet velocities. Data from this region is needed to enable design engineers to reliably control atomization quality, and it is required for numerical modelers to create programs with accurate initial conditions and test baselines.

1.2 Spray Experimental Techniques and Limitations

Unfortunately, experimental options for near injector spray analyses are limited. Shadowgraphy is a classical technique for visualizing sprays; but, it is an inherently 2D approach with limited applicability to the turbulent, 3D, system of sprays. Furthermore, it can have trouble resolving small spray structures and droplets. Phase Doppler Particle Analysis (PDPA) and Laser Doppler Velocimetry (LDV) are potentially very powerful. However, they are restricted from the near field because of the ellipsoidal shaped droplets and unknown droplet orientations in the near field. Typically, current methods restrict PDPA to about one hundred injector diameters from the injector. Other methods, such as Particle Image Velocimetry (PIV), can be adapted to track drops. Unfortunately, this is another inherently 2D technique. Planar illumination methods can detect vectors normal to the camera, but the depth of field is very restricted. Recent developments in Stereoscopic PIV (3D PIV) use multiple cameras to visualize 3D velocity vectors. However, separate shadowing methods must still be incorporated to find droplet sizes. High intensity x-rays (such as Kastengren et al., 2010) can be used to capture 2D information in optically dense regions, but they do not produce 3D maps anywhere in the spray.

Holography is an established method for studying sprays (e.g. Jones et al., 1978, Santangelo and Sojka, 1995, Palero et al., 2007, Sallam et al., 2006) in the near injector region (Lee et al., 2007, Miller, 2006, Miller et al., 2006, Miller et al., 2008). Digital holography is particularly effective at mapping the 3D spray field. 3D droplet distributions, sizes, and velocity vectors can be calculated, regardless of droplet shape. Note that individual droplets are measured; time and mass averaged properties can be calculated afterward.

Sprays are good candidates for experimental diagnostics using holographic imaging. The Sauter Mean Diameter (SMD) is a commonly used and readily measured parameter in multiphase fluids. The SMD is the ratio of the particle volume to the particle surface area. Effectively the SMD is a size-weighted measurement of the diameter. It frequently correlates closer to combustion characteristics than the diameter alone. It is given by Crowe et al. (1998):

$$SMD = \frac{\int_0^{Max.Diam.Particle} D^3 f_n(D)dD}{\int_0^{Max.Diam.Particle} D^2 f_n(D)dD} \tag{1.1}$$

where D is the particle diameter and $f_n(D)$ is the size distribution function. This is convenient for the experimenter as larger droplets are easier to detect and less error is introduced when smaller, hard to measure droplets are missed.

A series of holograms is superior to other results in that it can map the entire three dimensional spray test section, and complete it near the injector (Miller et al., 2008). However, traditional holography is very time consuming and requires manually developing, with wet chemistry, the holograms. Digital holography alleviates these problems through numerically developing the holograms. Unfortunately, digital holography is computationally intensive and it is not very effective in the near field. Furthermore, because of excessive visual interference, effective image analysis routines for the near injector region have not been developed. In other words, the signal / noise ratio is too weak in the near field.

If digital holographic image processing routines were matured enough to handle the difficult near injector region, the impact on spray engineering would be substantial and immediate. Spray holographic methods could be freed from their limited research role into a useful tool for design and engineering.

1.3 Problem Statement

There is an opportunity to expand digital holographic microscopy in analyzing the spray near the injector. Holography's intense image processing and lack of automation for droplet analysis prevents it from expanding out of academia and into industry. The current methods of mapping out the test section by hand (and eye) is extremely time consuming. Several research groups have suggested automated image processing approaches for holography. Unfortunately, there is no comprehensive algorithm for near field spray analysis. Particularly, the difficult issues of optically dense sprays, fast drops in cross flow, noisy holograms, and very large depths of focus due to limited optical access must be resolved. Any algorithm must be robust and run quickly in order to create statistically significant correlations, especially for the distance of a drop to the camera. The goal of the current research is to create an algorithm to automatically analyze holograms of the near field, and then employ it to advance the study of near field sprays. Any advances that enable the study of sprays closer to the injector will be of great value.

Chapter II. Literature Review

2.1 Introduction to Holography

A hologram is a 3D image in which the third dimensional information is stored within interference fringes within the image plane. A hologram is created when the wave front of a light source interferes with an object and is then compared to the original wave front; see Figure 2.1 for a simple setup for sprays.

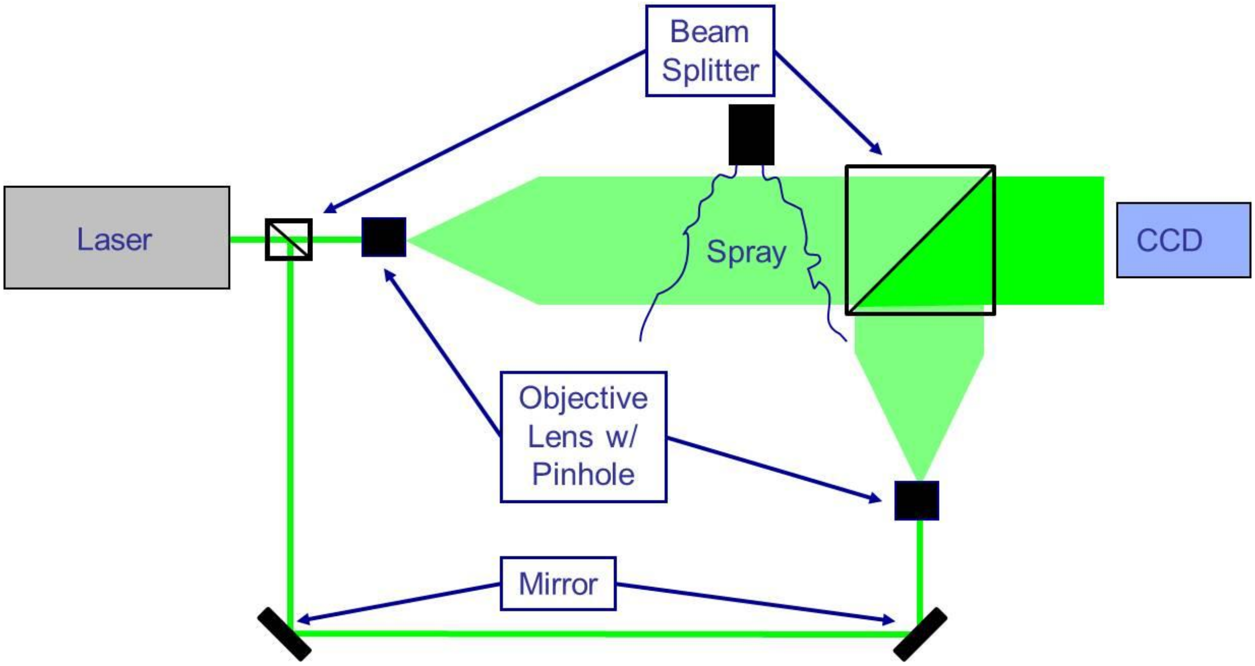

Figure 2.1 Basic Holography Experimental Setup.

Here, the light source (a 532nm Nd:YAG laser is common) is split into two, identical, beams by the first beam splitter. One beam is expanded and directed through the test section. Its wave front will be changed as it passes by and interferes with the object being imaged. Here the objects are the individual drops within the spray cone. The second beam is routed around the test section. Since it never interferes with the spray, it maintains the original wave front. These object and reference beams are recombined by the second beam splitter. Since it has been changed, the object beam's wave front will constructively and destructively interfere with the reference beam. This is viewed as a pattern of interference fringes by the camera. Note the camera does not have a lens. A sample hologram of dripping water is given in Figure 2.2 (Lee et al. 2007).

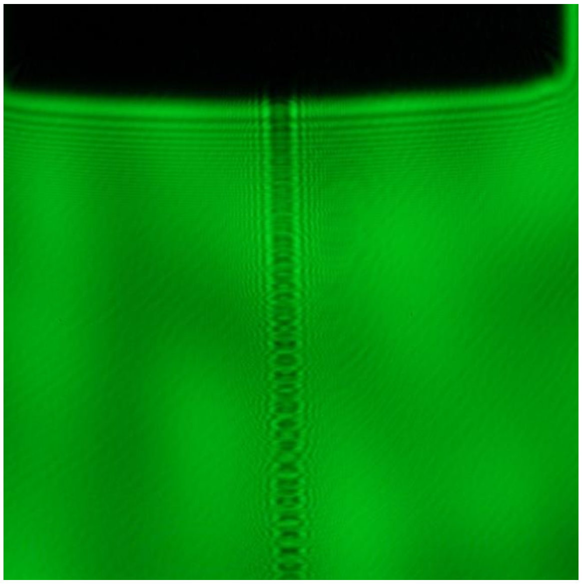

Figure 2.2 Sample Hologram / Test Case #1 (Lee et al., 2007).

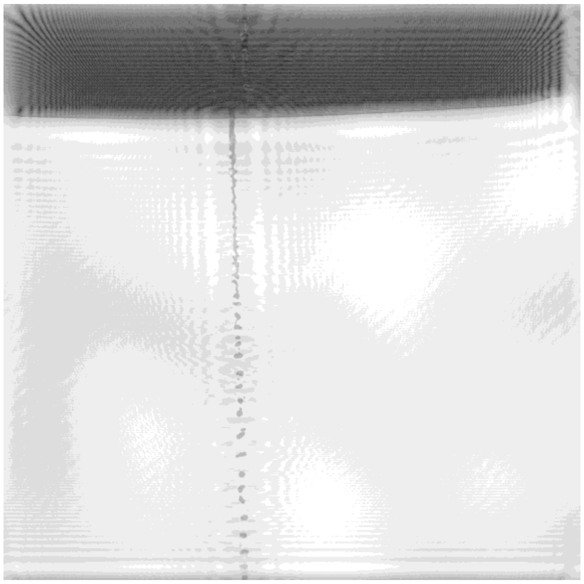

Figure 2.3 Sample Reconstruction (Centerline).

The black region at the top of Figure 2.2 is the injector assembly. The blurred stripe coming down the center of the hologram is a stream of drops. The power of holography becomes clear when the hologram in Figure 2.2 is reconstructed along the center line of the injector; see Figure 2.3. The mathematics behind the reconstructions are discussed in Chapter III. The reconstructed "slices" act as the focused image for the hologram at the specified distance from the camera. The interference fringes and the geometry of the experiment are used to provide detailed 3D information of the test volume. Image processing techniques are then used to find the droplets within the 3D space.

2.2 Early Development of Holography

In order to resolve the issues of holographic analysis in the near field, it is instructive to understand the history and current applications of holography. Holography has a diverse past in a variety of advanced technologies and has been used to study a range of physical systems. The concept of holography was first proposed by Gabor (1948) and improved by Leith and Upatnieks (1965) with off-axis setups. Since, others have advanced the technology to include different optical arrangements and specific imaging methods. Early work in inline holography was pushed into the submicron area with Royer (1977). While fluids measurements are the current research focus, holographic techniques have been used in industry (Conley, 1992) and in a variety of mechanical experiments; for example, measuring strain (Ara and Sirohi, 2006), measuring rotating objects (Pedrini and Tiziani, 1995), and difference displacements of a membrane (Gombkoto et al., 2002). Reconstructed Fresnel holograms have even been used in three-dimensional object recognition software (Nelleri et al., 2006).

2.3 Traditional (Nondigital) Holography

To better grasp the problem of automating digital holography, the following sections demonstrate a traditional setup and discuss results from a variety of research groups. This section shows that traditional holography is an established experimental method with a variety of applications; it is a robust system with the capability to be fully automated.

Hariharan (2002) explains a variety of holographic methods and their setup. Pu and Meng (2005) provide a comprehensive example of a holographic apparatus; see Figure 2.4. In traditional holography, the experimental setup is to have a laser, run through a series of mirrors, plates, and a collimating lens, fired through a test section; see Figure 2.4. A separate reference beam may be used if the test section is too dense. The holographic plate is usually set at an angle (off-axis holography) so the object and virtual image are not on top of each other. A CCD camera may even be used, but it does not take a direct picture of the flow field. Rather, the flow field image is captured on the photographic plate and the CCD camera mechanically scans the plate (Pu and Meng, 2000 and Pu et al., 2000, Katz et al., 1999).

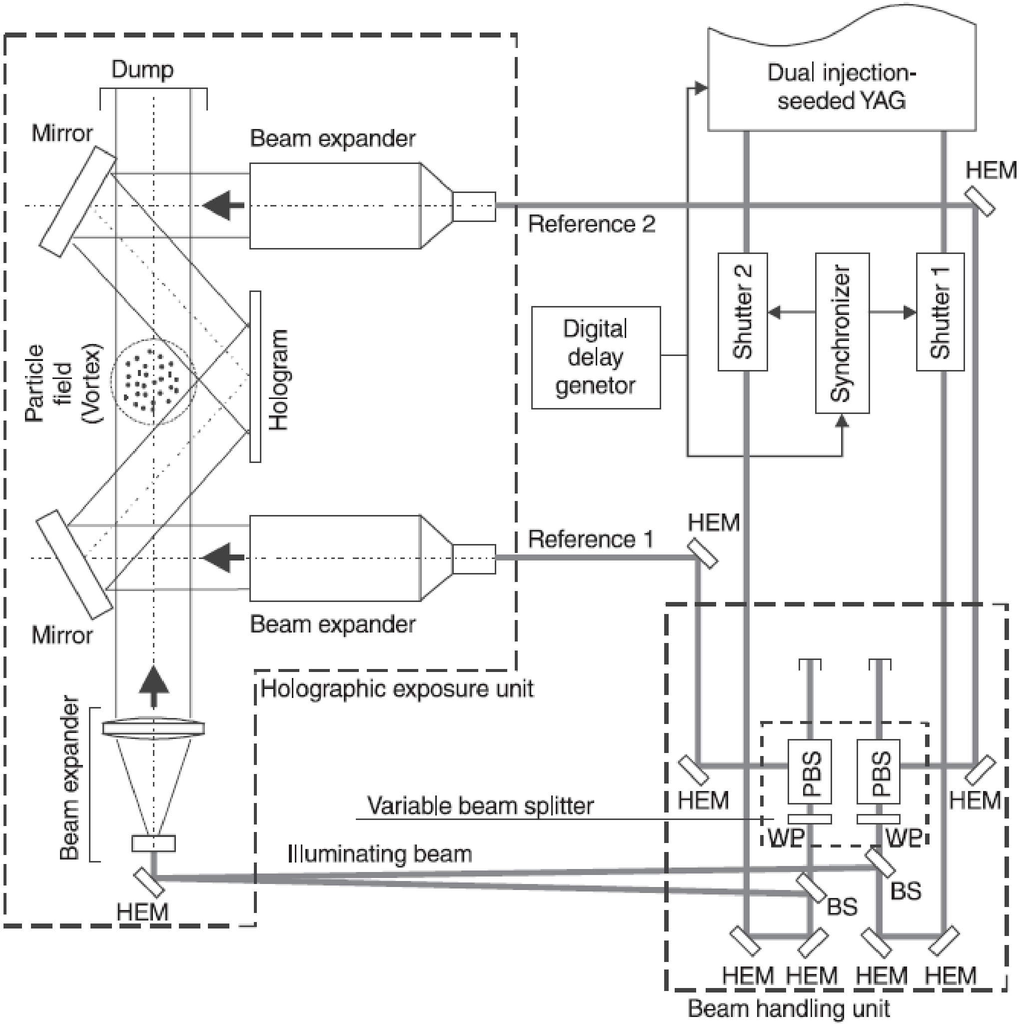

Figure 2.4 Configuration of Traditional Off-Axis Holography (Pu and Meng, 2005).

Much of the fluid dynamics related holography literature is devoted to holographic particle image velocimetry (HPIV). That is, a standard PIV technique is used for seeding a flow field (not just sprays) with particles. Then, the standard 2D imaging suite and analysis techniques are replaced with one suitable to holographic analysis. For example, Pu and Meng (2000) and Pu et al. (2000) use a very complex setup, with three laser beams and a multi-axis control system to drive a ninety-degree off-axis HPIV system. Without the limitations that digital holography contain, Pu and Meng (2000) and Pu et al. (2000) are able to attain much higher resolution in the reconstructed image, with much tighter spatial resolution in the depth of field.

Despite the disadvantages of manual holography, good experimental results are obtainable. Pu and Meng (2000) obtain impressive images of vortex rings and Pu et al. (2000) obtain very detailed images of fine particle distributions. Yang et al. (2001) produce PIV results of hairpin vortices. Some research has been done in multi-phase flows with bubbles. For example, Lauterbornd and Hentschel (1986) have used high-speed holography and holocinemetagraphy to record cavitation bubble dynamics in a liquid flow. By using a frame size of only a few square millimeters, frame rates of 300,000 f.p.s. were recorded. This enabled Lauterbornd and Hentschel (1986) to capture the acoustic waves passing through a series of cavitation bubbles as they formed and collapsed. Convection has been studied using HPIV (Corvaro and Paroncini (2006) and Skarman et al. (1998)); by incorporating interferometry, plumes from heat sources are detected and temperature measurements can be made.

Alfieri et al. (2006) made color digital holograms of an object by taking simultaneous holograms with two cameras set apart by some distance. Two lasers, one red and one green, were combined and used to illuminate the test section. One hologram was then reconstructed, with bias towards the green wavelength while the other hologram was reconstructed, biased towards the red wavelength. The object in the image was identical, so when the two images were superimposed, a color image was created.

Traditional HPIV is still an active area of research. In fact, recent theoretical finds have occurred. As inline holography is limited by excessive speckle noise (Meng et al., 1993), Pu et al. (2002) advocate off-axis holography. Pu et al. (2002) quantitize the capacity limits and accuracy of off-axis HPIV through Mie scattering theory. They find the signal to noise ratio (SNR) is a function of the ratio of the particle's intensity and the mean-noise intensity. Forward recording (the object laser, test section, and photographic equipment is aligned- the reference laser still has an incident angle) produces the optimal intensity ratio. The optimal intensity ratio is a function of the inverse of the: wavelength squared, seeding number density, and depth of the test section (Pu and Meng, 2005).

2.4 Digital Holography

For all its successes, traditional optical methods are still restricted by two major shortcomings. The holograms must be reconstructed manually, subjecting them to visual errors from the experimenter; and the holograms are created using wet chemistry. These problems have significant costs in time and in using chemicals. Once mature, automated digital holography will remove these constraints and allow the experimenter to focus on the experiment rather than creating and analyzing holograms.

Most of the background and knowledge base needed for digital holography is provided by Schnars and Jueptner (2005) and Asundi (2002). In terms of the physical setup, digital holography is very similar to other forms of holography. Referencing Figure 2.4, to make the experiment “digital”, the photosensitive plate is replaced by a lensless CCD camera and its accompanying computer controls. Then the hologram can be captured in a digital format and reconstructed numerically rather than with wet chemistry. While it may be desirable to alter the experiment in other ways, no other rearrangement is required to run completely digital holography.

Typical results for digital holography depend on using seeded particles for holographic PIV (for example, Elavarasan and Meng, 2000) or using edge detection routines instead to find existing particles. For example, Katz et al. (1999) took advantage of not requiring seeding particles in their submersible inline digital holography rig used for measuring velocity distributions of plankton. Velocities were calculated using the centroids of the imaged objects. Other research investigated densities of settling pollen particles (van Hout and Katz, 2004). More diverse results include Choi and Puri (2000 and 2001), who used digital holography to characterize pre-mixed flames. They ran experiments to describe the effects of flame stretching (2000), reported flame speeds, and used interferometry to deduce the temperature and chemical reaction rates (2001). Soria and Atkinson (2008) used a tomographic approach to implement HPIV. While all of this research has leveraged computers to digitize parts of the experiment, mapping the flow field, from hologram reconstruction to charting the location of the recorded objects, must be still be fully automated.

van Hout and Katz (2004) encountered many of the same technical problems that are encountered in automating holography for spray diagnostics. van Hout and Katz (2004) used digital inline holography (as opposed to digital inline holographic microscopy) to find the density of irregularly shaped pollen particles. Similar to that taken by Miller (2006) and Miller et al. (2008), their approach is:

a) Identify the hologram reconstruction equations. Given different experimental setups, different equations are used. Many researches use the Fresnel equations. van Hout and Katz (2004) used the Fresnel-Huygens diffraction equations. Miller (2006) and Miller et al. (2008) use the Rayleigh-Sommerfeld convolution equations (Schnars and Jueptner, 2005).

b) Reconstruct the hologram to different depths until focused particles (pollen granules for van Hout and Katz) are found. As the reconstruction is linear, across the depth of the holograph, van Hout and Katz (2004) reduce reconstruction time by collapsing the hologram data into one plane. This prevents the pollen from ever being in focus, but such data is unnecessary for finding the velocities of particles moving in one plane. Clearly this simplification does not apply to 3D spray analysis.

c) Isolate the particle using Matlab's image processing toolbox (van Hout and Katz, 2004):

   i. Subtract the background to increase the signal to noise ratio
   ii. Run "Canny" edge detection to trace the outline of the pollen (Miller, 2006 and 2007 uses "Sobel" edge detection)
   iii. Use Matlab commands to fill in the image
   iv. Find the area of the 2-D image of the pollen, presumably with Matlab's image area commands
   v. Calculate the equivalent diameter from the equation:

$$d_A = 2\sqrt{A_p / \pi} \tag{2.1}$$

This is equivalent to the formula used by Matlab (Gonzales et al., 2004).

To improve the quality of the holograms, digital holographic microscopy is favored over digital holography. Digital holographic microscopy differs from digital holography in that no collimating lens is used. Instead, the wave front expands through the test section. Just before entering the test section, the laser passes through a pinhole objective. This restriction only allows the portion of the laser most in-line with the objective and pinhole to expand with a hemispherical wave front. This enables easy magnification of the hologram, but necessitates a change in the convolution equations used by most researchers. This method relies on a large percentage of the wave front not interfering with the spray so that it can act as the reference beam.

This simplification results in cleaner images than traditional holography (Miller, 2006). This is due to the reduced number of optical components and therefore, reduced aberrations and speckles. This simplification will ease automatic edge detection software. The drawback to this configuration is the reference beam may be blocked. Dense sprays may not let enough laser beam through the test section unobstructed; thus, preventing a clear interference pattern from forming. It is inherently magnified, at the cost of reduced field of view. However, it possesses a higher resolution then comparable photography which enables the better detection of fluid structures.

Inline holography has the important advantage over off-axis holography of having lower resolution requirements. This result is an extension of Shannon's sampling criteria. This is critical as the CCD cameras currently used to implement fully digital methods do not have the resolution of standard holographic plates. Commercially available digital cameras can be used for taking single holographs of the flow field for image reconstruction (Lee et al., 2007); unfortunately, they do not possess the cycling speed necessary to create PIV images (like an interline CCD).

Several papers have suggested improvements to the typical outline given in van Hout and Katz (2004) that would reduce errors caused by signal noise and equipment limitations. Digital holography can be improved by techniques that are already common in other areas of image processing. The following provide several examples.

Speckle is the randomly distributed scattering of very small black dots created by imperfections in the coherent illumination and the discretezation of the hologram signal. It is generally viewed as random noise. It is generally not a problem if the objects of interest are much larger than the pixels. Garcia-Sucerquia et al. (2005) review reducing speckle noise, through digital methods (after imaging by the CCD camera as opposed to purely optical methods in the test facility), of Fresnel holograms. They cover two general methods, median filtering and matrix reduction.

Matrix reduction is in effect a smearing of the intensities of the pixels in the image; see Figure 2.5. Given the existing hologram pixel array, a new, smaller array is created. Each pixel in the new array is an average of four corresponding pixels surrounding that point in space in the original hologram.

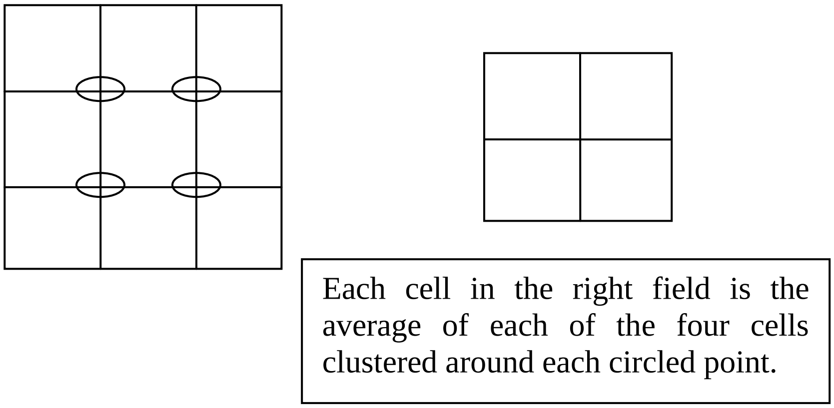

Each cell in the right field is the average of each of the four cells clustered around each circled point.

Figure 2.5 Matrix Reduction Approach from Garcia-Sucerquia et al. (2005).

Given that near field drops have very small diameters (<10 pixel diameter is not uncommon), a matrix reduction of any size would quickly impact the veracity of any edge detection results. However, the current study did find that matrix reduction does offer enormous savings in processing times for larger droplets.

Median filters are a type of averaging filter. Each pixel's intensity is reset to the median of its neighbors. Median averaging is used instead of mean averaging because the median intensity of a set of pixels is less sensitive to spikes in intensity (Gonzales et al., 2004). In Garcia-Sucerquia et al. (2005), the filter is weighted towards reducing localized spikes in the intensity while preserving the background. Ultimately, Garcia-Sucerquia et al. (2005) suggests a combined approach of using a 7 pixel by 7 pixel median filter combined with matrix reduction. They do caution that the 7x7 optimum value would be highly dependent on the image in question.

Because of the CCD sensor's low resolution and the virtual and object image potentially overlapping, digital holograms can be hard to read in even otherwise perfect experimental conditions. Several methods have been proposed to reduce the error imposed on the distorted interference fringes from the background noise.

The reference beam is regular while the object beam is speckled. These speckles move stochastically as the recorded object moves (Demoli et al., 2003). By subtracting a stochastically changed image from another image, the zero-order disturbance is eliminated. Other methods for reducing the zero-order term are through adjusting the phase. For example, Zhang et al. (2004) suggests adding a filter to the experimental setup to eliminate zero order diffraction.

Kreis and Jueptner (1997a&b) offer the most straightforward method. They propose to filter the image through what amounts to a high-pass filter with a low cutoff frequency; hence, the, zero-order, “DC term” will be eliminated. This is done by subtracting the image’s average intensity from each pixel’s intensity (Kreis and Jueptner, 1997b). This is the same method used by Miller (2006) and Miller et al. (2008). This smoothes the background by suppressing all of the pixel intensities in the image. In theory, it simplifies edge detection.

The classical approach to locating focused droplets is centered on the droplet intensity. For example, Choo and Kang (2006) and Yang et al. (2008) characterize the intensities of in and out of focus particle images and offer a correlation approach for finding the particle’s focal plane. And Gire et al. (2008) discuss solutions to typical problems encountered when measuring the intensity. Pan and Meng (2003) suggest a new way of determining a droplet’s location in the z-direction. Pan and Meng (2003) use the complex amplitude from the hologram reconstruction. By minimizing the variance in the complex amplitude, they identify the focused location. They claim it is a more accurate identifier of the depth of field. Note that Pan’s and Meng’s research was for HPIV, in which the particle size and shape are known beforehand. Also, because of the very short depth of focus, there are few out of plane particles appearing in any one image.

Miller (2006) found that holographic microscopy produces cleaner images than traditional arrangements. This is logical as the expanded wave front of the light source reduces the number of out of focus drops and related irregularities in neighboring slices. Sheng et al. (2006) charted this effect of high expansion angles of the object beam through the test section give short depths of focus. However, the high expansion angle may not be available or desired given an optical setup. Additionally, optical access may be limited so that a high expansion angle of the laser wave front interferes with the test setup or some surrounding structure. This is compounded because, as the CCD is moved further from the microscope lens, the hologram's depth of field is reduced. A smaller magnification will reduce this effect. While not as great a concern in a fully automated system, a very short depth of focus hinders detecting the droplet existence in that more reconstruction slices are needed so as not to miss drops in extreme circumstances. Xu et al. (2003) suggest using the hologram itself (or summed slices) as the basis for droplet detection, but this will not always be possible. For example, the near field holograms are too noisy to easily combine slices. Suffice it say there will be times when single view holograms generated with low magnification objective lenses will require processing. Holographic microscopy should be used when possible, but the spray analysis algorithm should be able to accommodate low expansion angles.

2.5 Alternatives to Holography

HPIV is not the only visualization method to use holograms. Hariharan (1992) is a comprehensive source for interferometry. Pan and Meng (2003) mention several alternatives to HPIV, including stereoscopic particle tracking (Virant and Dracos, 1997), defocusing digital particle image velocimetry (DDPIV) (Pereira and Gharib, 2002), and forward scattering particle image velocimetry (FSPIV) (Ovryn, 2000). None of these are as promising as HPIV in that they are limited to small fields of view or a small number of particles.

2.6 Hardware Improvements

The area that will affect all aspects HPIV is the hardware used to record the hologram. Besides using high quality optics and clean equipment, fast lasers and high resolution cameras offer major areas for improvement. And because of the limited field of view and heavy image processing, any hardware improvements which can improve the quantity of holograms required or their processing times would be very helpful.

Very short laser pulses give the best results; the shorter duration allows less light to create extraneous interference fringes from the droplets, viewing ports of the test volume, and all of the lenses and mirrors. This cleaner image results in a higher Signal to Noise Ratio (SNR). Nicolas et al. (2006) experiment with a femtosecond laser beam in an inline digital holography setup to measure particles. Unlike most lasers used in fluid diagnostics, ultra-short laser pulses are not monochromatic. They exhibit a Gaussian spectrum and have a low coherence length (Nicolas et al., 2006). Due to the low coherence length, a reduction of parasitic fringes increases the SNR. For hologram reconstruction, Nicolas et al. (2006) use the two-dimensional fraction Fourier transformation (FRFT) instead of the traditional Fresnel transform. This is because the classical methods do not account for the astigmatism caused by the laser's random spectrum. The result was several very clear holograms of individual particles with many interference fringes. The holograms were reconstructed using the FRFT, although the group did experience some difficulty when the laser beam itself was not symmetric. Femtosecond lasers would also benefit high speed spray fields (i.e. scramjet combustion) as longer lasing times cause the drops to streak.

Improvements in reconstruction speed and characterization of the PIV space can also be made at the hardware level. Few examples have been found in the literature. But, Roth et al. (1995) used a motion estimation processor attached to their camera equipment to speed creation of their PIV maps. As graphics card level image pre-processing becomes more available, hardware level hologram analysis will become possible.

2.7 Droplet Velocity Measurements

Particle Image Velocimetry (PIV) calculates the velocity vector of a particle by finding the displacement over a known time step from a pair of pulsed images. Traditionally, PIV relies on a collection of seeded particles which give a statistically significant sample. However, the current work aspires to calculate the velocity vector of a small number of droplets. Instead of statistically, droplets must be tracked individually. In the literature, this is a sub-class of PIV known as Particle Tracking Velocimetry (PTV). Typically, high particle density PIV is used when the surrounding flow field is of primary interest; whereas, low particle density PTV is used when the actual particles (or droplets or bubbles) is the research focus.

In most PTV setups, the image is divided into search areas. Image pairs are searched for within these boxes. Unfortunately, this tends to bias results towards lower velocity results. This is due to the decreasing likelihood of finding pairs within the same search area as the velocity increases (Grant, 1997). Careful sizing of the search area can prevent this. It stands to reason this would be more difficult if there is a wide range of particle velocities. Lower density images are more susceptible to this bias effect (Grant, 1997). Grant (1997) offers several guidelines for sizing the areas:

a) $N > 10 - 20$ (increase the particle density within an image, Grant, 1997). Obviously, increasing the number of droplets is not possible in this research. The search area could be increased.

b) Where u, v are the in plane velocity components, Δt the pulse delay, d is a characteristic dimension of the search area, and M is the magnification, the following relation should be used (Grant, 1997):

$$\left(u^2 + v^2\right)^{1/2} \Delta t < \frac{d}{4M} \tag{2.2}$$

So large velocities, long time delays, and high magnification all approximately equally directly affect the minimum search area.

c) Where Δu is the variation in velocity across an image pair, the following relation should be used (Grant, 1997):

$$\frac{|\Delta u|}{|u|} < 0.2 \tag{2.3}$$

This is in effect a droplet acceleration term limited by the time delay, the spray flow field, and the search area.

Another approach not listed by Grant (1997) is to simply search the image twice by shifting the search area by half of its size. This will not completely remove the problem, but it does reduce the chance of an error. Other approaches include biasing the image pairing algorithm by supplying it the free stream velocity vector or by optimizing all possible velocity vectors.

Further research in applying neural networks to optimizing the velocity vector is suggested by Grant (1997). Other groups, for example, Hassan and Blanchat (1999), effectively pair images by minimizing the standard deviation of all of the bubbles' velocity vectors, sizes, and average grey scales (image intensities).

2.8 Literature Review Summary

To explore holography for further fluids and combustion research requires electrical engineering and image processing. Several works are useful for understanding the detailed problems inhibiting holography, and what approaches can be used to overcome them. There is a wide range of applications for digital holography with similar problems to sprays. Unfortunately, none of these examples are exactly the same.

A true PIV application is not possible because a statistically valid number of particles (drops) are not available. Furthermore, a separate routine must be used to find the individual droplet's distance from the camera. Using the complex amplitude is attractive for this, but that would require creating an entirely new matrix when computational resources are already at a premium. Other research has stopped at the intensity value or its average across the drop image. Unlike many of these applications, the size and shape are not known a priori. Finally, near field sprays holograms vary widely in quality and clarity. Going back to the underlying problem, the issue is one of image processing. Large numbers of holograms must be processed to go beyond exploring the spray fundamental physics. And, droplet images can (but are not required to) have a very long depth of focus and their focused locations are obscured by surrounding image artifacts and noise. Finally, the physical restrictions of optical access may make the experiment difficult.

2.9 Specific Research Objectives

Currently, no other methods work with sufficient speed to analyze more than a handful of near injector spray images, making it extremely difficult to draw universal conclusions regarding the spray structure. Hence, the specific objectives of this project were to:

- Incorporate the existing digital hologram reconstruction process into an overarching image processing algorithm for spray analysis.

- Develop subroutines to:

- Identify droplets, including search parameters for size and horizontal and vertical position.

- Address the depth of focus problem inhibiting the measurement of a drop’s span wise location. Use the results of this study to develop a subroutine to calculate the drop’s span wise location.

- Pair droplet images from double view holography (when applicable).

- Calculate individual drop 3-D velocity vectors, including spatial and temporal search criteria.

- Validate the new algorithm using simple and complex holograms.

- Demonstrate the algorithm by analyzing near injector sprays of interest.

Chapter III. Experimental Methods

3.1 Digital Hologram Creation

Because Sheng et al. (2006) demonstrated that an increased expansion angle significantly shortens a particle's depth of focus, and hence Miller (2006) found digital inline holographic microscopy to produce cleaner holograms, this project exclusively uses digital inline holographic microscopy. The exact arrangement varies with the spray under consideration and optical access limits; see Section 3.3 and Section 3.4. However, a 532nm Nd:YAG laser in combination with a pinhole objective (spatial filter) was always used. As available, a research grade interline CCD camera or a consumer grade commercial digital camera were used. The holograms produced were then reconstructed (see Section 3.2) and used to evaluate the methodology that will be presented in Chapter IV.

3.2 Digital Hologram Reconstruction

While the mathematics describing hologram reconstruction were developed for optical methods and wet chemistry (e.g. Goodman, 1996), they can easily be thought of as image processing and convolution using modern methods. The 3D information stored in a hologram is retrieved through numerical reconstruction (Schnars and Jueptner, 2005, Lee et al., 2009, Miller et al., 2008). The digital hologram is reconstructed along planes parallel to the hologram. These "slices" act as a focused image at a specified distance from the hologram plane. Using the hologram from Figure 2.2, a reconstructed slice along the focal plane of the drops can be calculated; see Figure 2.3. Note the interference fringes surrounding each drop. These will cause the image processing algorithm problems as the droplets become obscured.

Figure 2.2 is reconstructed through the numerical methods developed in Schnars and Jueptner (2005) and Kreis et al. (1997a&b) and followed in Miller, et al. (2008). The geometry of the reconstruction is given in Fig. 3.1. The hologram plane image is defined in (x,y) coordinates. Reconstruction distance away (d), the reconstruction image is defined in (ξ,η) coordinates. The z axis is common to both images and is parallel to d. ρ is the Euclidean distance between any two points in the two images. In digital holography, ρ is the point to point distance between any two pixels.

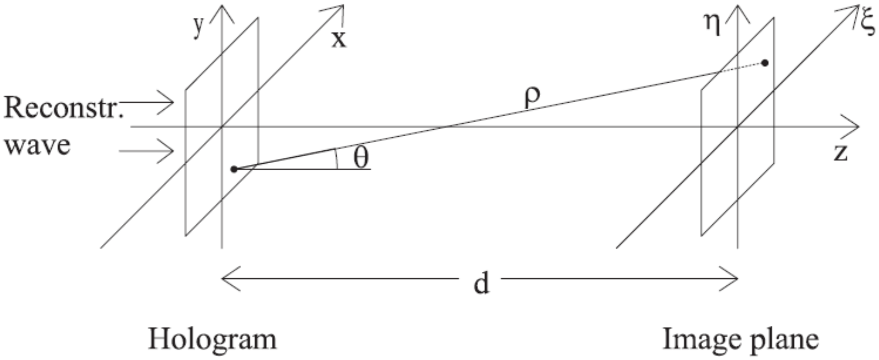

Figure 3.1 Geometry of Hologram Reconstruction (Schnars and Jueptner, 2005).

Recall that the interference is the superposition of the object and reference wave fronts combined on the hologram (Goodman, 1996). From Schnars and Jueptner (2005), and based on Huygen's principle that any point of a wave front acts as a source point for new wave fronts, the basic image equation is:

$$\Gamma(\xi,\eta) = \int_{-\infty}^{\infty}\int_{-\infty}^{\infty} h(x,y)E_R^*(x,y)g(\xi,\eta,x,y)dxdy \tag{3.1}$$

where

$$g(\xi,\eta,x,y) = \frac{i}{\lambda}\frac{e^{\frac{-i2\pi}{\lambda}\sqrt{d^2+(x-\xi)^2+(y-\eta)^2}}}{\sqrt{d^2+(x-\xi)^2+(y-\eta)^2}} \tag{3.2}$$

Eqn. 3.1 is the undistorted diffraction of a light wave at an aperture (hologram); see Kreis (1997a&b) for a detailed derivation of the equations applied to digital reconstructions. h is the hologram object wave, E is the reference wave that is used for reconstruction, and g is an impulse function accounting for the laser wavelength (λ) and point to point distance (ρ). E^* is the conjugate of E. Schnars and Jueptner (2005) simplify Eqn. 3.1 by identifying it as a Fourier Transform of a convolution equation. By definition, Eqn. 3.1 is a convolution between hE_R^* and g:

$$\left(hE_R^*\right)\otimes g = \int_{-\infty}^{\infty}\int_{-\infty}^{\infty} hE_R^* g \, dxdy \tag{3.3}$$

which can be solved because the Fourier transform of the convolved terms is the product of the Fourier transform of the terms:

$$\mathscr{F}\{\Gamma\} = \mathscr{F}\{(\mathrm{h}E_R^*)\otimes \mathrm{g}\} = \mathscr{F}\{(\mathrm{h}E_R^*)\}\cdot\mathscr{F}\{\mathrm{g}\} \tag{3.4}$$

Schnars and Jueptner (2005) provide that $\mathscr{F}\{\mathrm{g}\}$ has an analytical solution, h and E are inherently discritized by the CCD sensor, and the spherical reference wave front is a function of reconstruction distances within each image coordinate system:

$$E_R = \exp\left(\frac{-2\pi i}{\lambda}\sqrt{d^2+(x-\xi)^2+(y-\eta)^2}\right) \tag{3.5}$$

Therefore numerical reconstruction is implemented through the inverse Fourier transform of Eqn. 3.4. The reconstruction intensity map (e.g. Fig. 2.3) is then calculated by squaring Γ (Schnars and Jueptner, 2005, Goodman, 1996);

$$I(x,y) = \left|\Gamma(x,y)\right|^2 \tag{3.6}$$

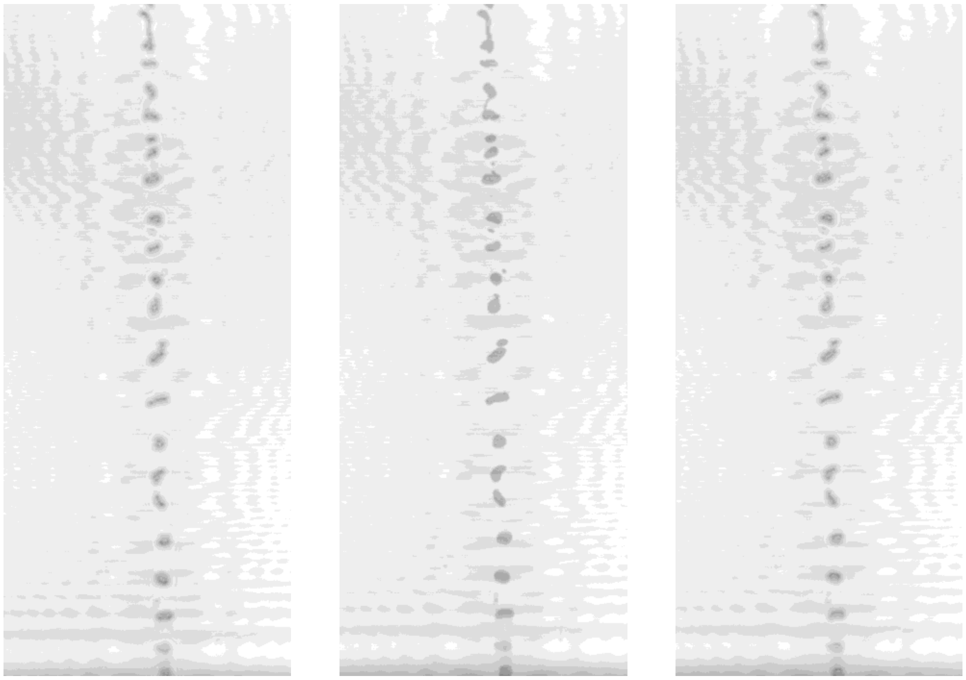

(a) (-5mm) **(b)** (centerline) **(c)** (+5mm)

Figure 3.2 Sample Reconstructions Going In and Out of Focus.

The reconstructed slices have been created; see Figure 3.2, and the search for droplets with the measurement algorithm can begin. This process is intuitive when looking at Figure 3.2, which is Figure 2.3, cropped around the droplets for clarity. In it, it is clear how droplets start unfocused when viewed at a reconstruction distance short of the focal plane (Figure 3.2a). As one moves towards the centerline of the column of drops, the drops come into focus (Figure 3.2b). Continuing past the focal plane forces the drops to go back out of focus (Figure 3.2c). So, knowing the experiment’s geometry, the algorithm can recreate the depth of field (z-direction, away from the sensor) by using the interference pattern created by a portion of the laser as it passes around a droplet.

3.3 Test Cases

As the issues involved in this project are primarily ones of image processing, a droplet's true diameter is not a driving factor in an algorithm's defining parameters. Rather, a driving factor is the droplet's projected size on the CCD sensor; it is the number of pixels that is of concern to the image post processing. That being said, drops that truly have a large diameter will in turn have a very long depth of focus. Therefore, to enable the evaluation of alternatives, three cases are used that will test the algorithm's range and ability to measure the size and location of low pixel count / short depth of focus and high pixel count / long depth of focus drops.

3.3.1 Test Case #1: Clean Hologram with Short Depth of Focus Drops

The first test is of a micro-injector dripping drops straight down; see Figure 2.2 for the hologram. This hologram is much cleaner (high signal/noise ratio) than most spray holograms. This test configuration and its holograms were originally studied by Lee et al. (2007). A standard Air Force resolution target (such as Figure 3.3a) was aligned with the injector so the hologram centerline could be easily ascertained by finding the reconstruction slice with the highest resolution (example in Figure 3.3b). This slice corresponds to the dripping drop's focal distance. As a 100μm injector is used, the drops produced take up very little of the CCD area. Furthermore, this setup gives holograms with a fairly short depth of focus. The experimental setup is given by Figure 3.4.

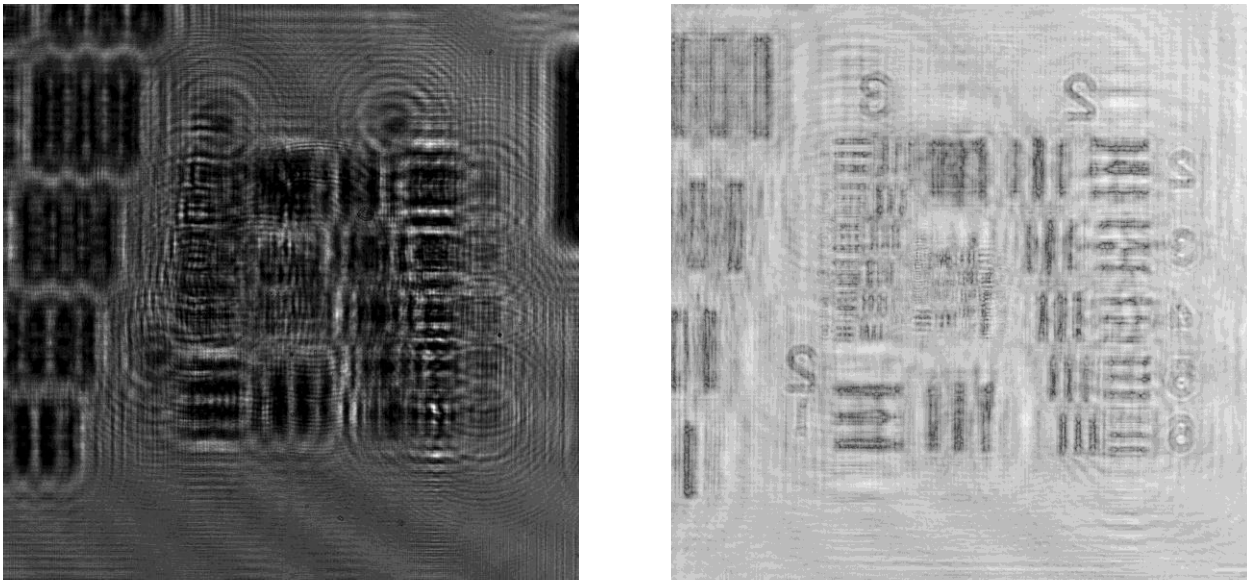

(a) **(b)**

Figure 3.3 AF Resolution Target Hologram and Focused Reconstruction.

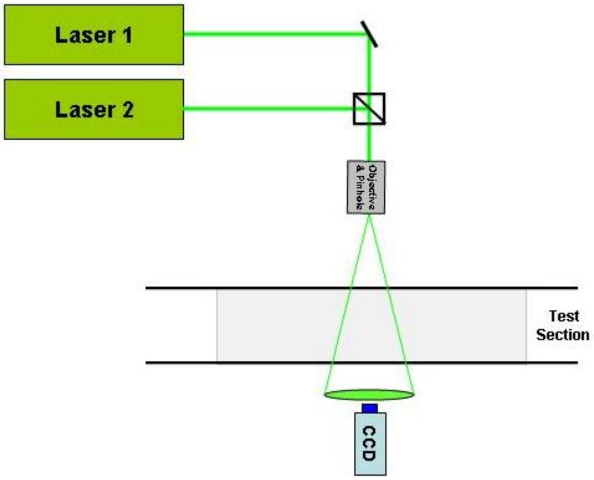

Figure 3.4 Test Case #1 and AFRL Experimental Setup.

3.3.2 Test Case #2: Clean Hologram with Long Depth of Focus Drops

Test Case #2 requires double view holography because the large depths of focus of the drops make it difficult to visually verify the correct focused distance; see Figures 3.5 and 3.6. This case is noisier than Section 3.3.1, but still clearer than typical near field reconstructions. What noise does exist in this test hologram is mitigated by the large drop size; see Figures 3.7

and 3.8. The second case produces large drops with a much higher pixel count and long depth of focus. The experimental setup for double view holographic microscopy is shown in Figure 3.13.

3.3.3 Test Case #3: Noisy Hologram with Long Depth of Focus Drops

The third test case uses the same experimental setup as Test Case #2, Section 3.3.2; see Figures 3.9 through 3.12. However, this case uses an atomizer that produces a larger number of small drops. This case produces noisy holograms because of common experimental concerns of interfering fringes, damaged pixels, and random image artifacts. Note that even these smaller drops still have a much larger depth of focus than the first test case. The experimental setup for double view holographic microscopy is shown in Figure 3.13.

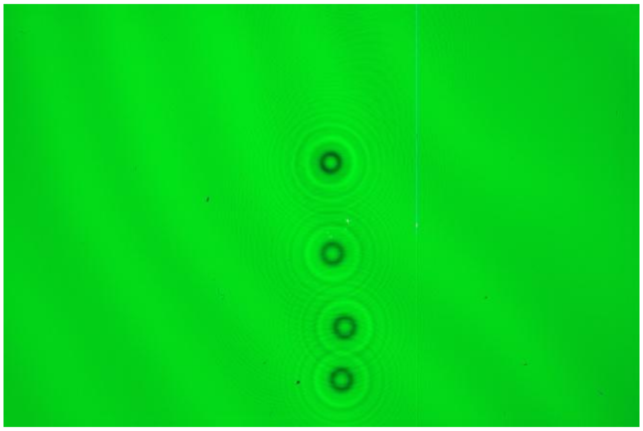

Figure 3.5 Test Case #2 / Left View.

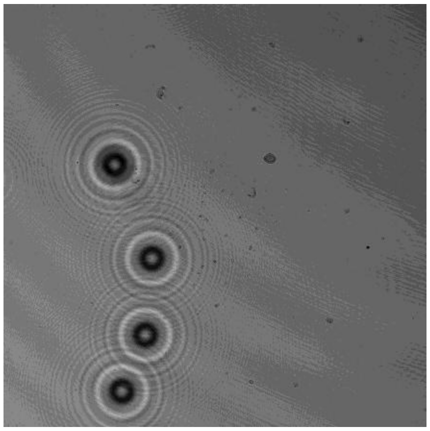

Figure 3.6 Test Case #2 / Right View.

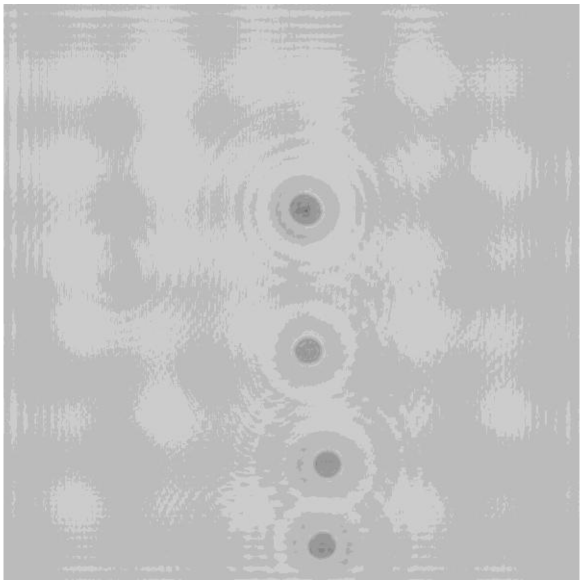

Figure 3.7 Test #2 / Left View Reconstruct.

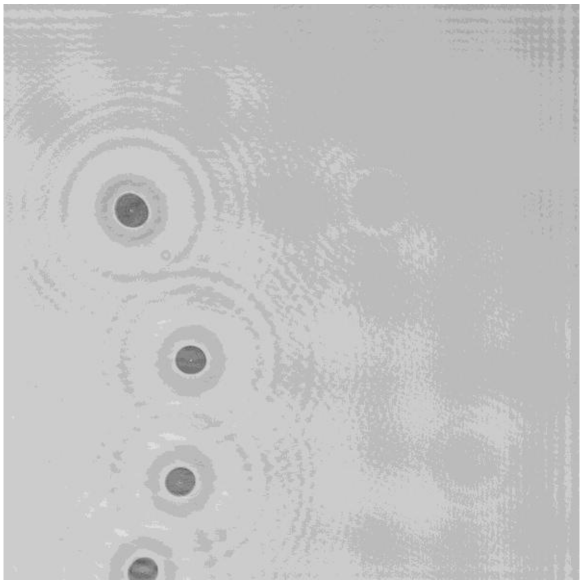

Figure 3.8 Test #2 / Right View Reconstruct.

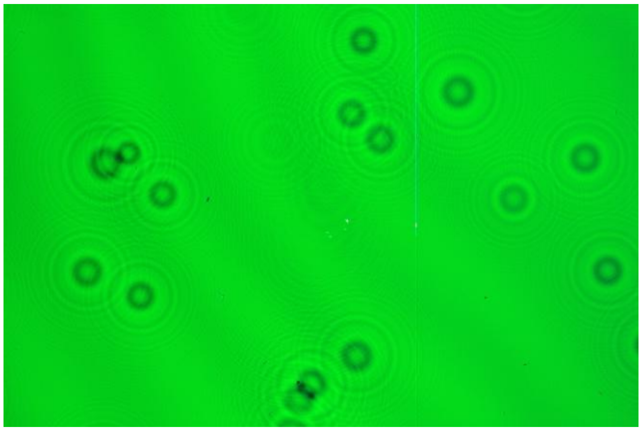

Figure 3.9 Test Case #3 / Left View.

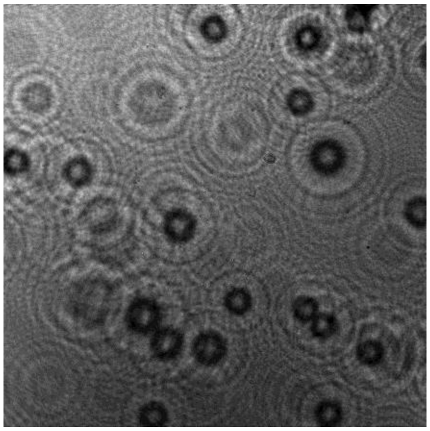

Figure 3.10 Test Case #3 / Right View.

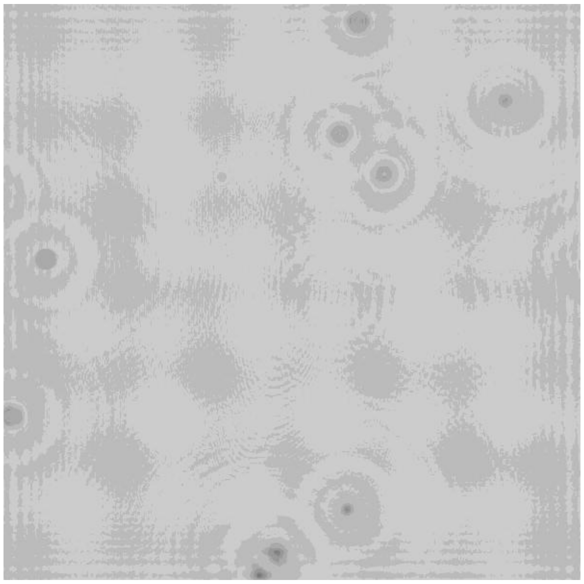

Figure 3.11 Test #3 / Left View Reconstruct.

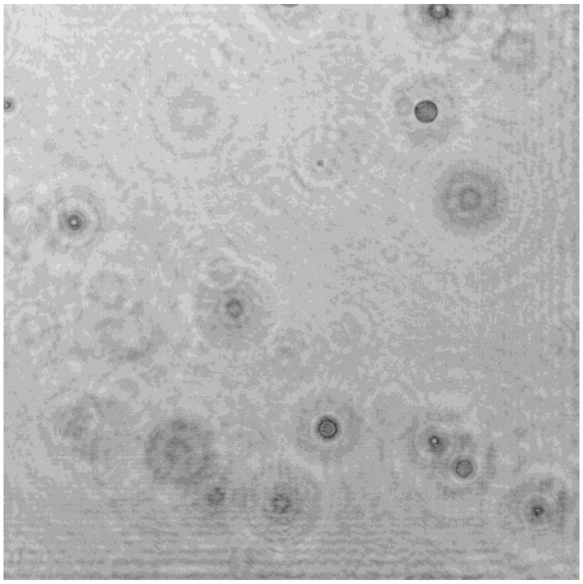

Figure 3.12 Test #3 / Right View Reconstruct.

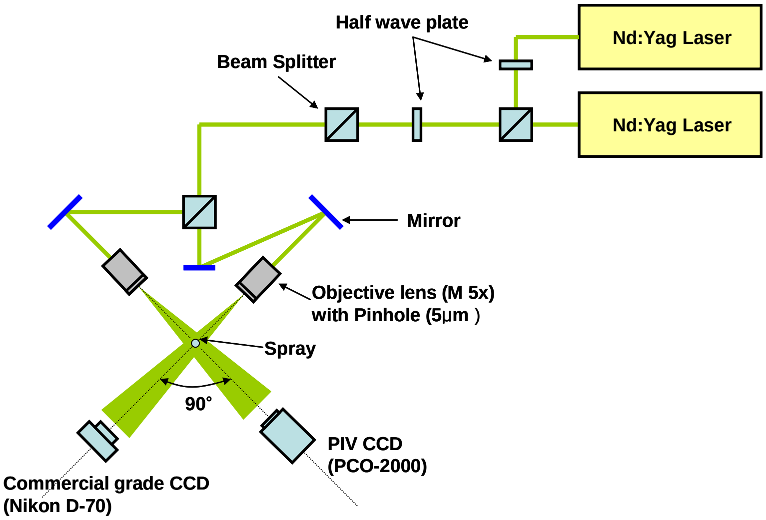

Figure 3.13 Test Case #2 & #3 Experimental Setup (Double View Holography).

3.4 Applied Sprays and Final Code Development

Final development is done on actual sprays of interest. The algorithms that are developed on Test Cases #1 - #3 are applied to a real spray to evaluate practical considerations such as run times and the impact on overall uncertainty of results. Validation is provided in Chapter IV and compiled results are presented in Chapter V. This series of holograms were produced on aerated liquid jets at the Air Force Research Lab-Propulsion Lab (AFRL). Air cross flow Mach numbers of 0.3 and 0.6 were used along with gas/liquid ratios (GLR) from 0 to 8% (refer to the test matrix in Table 3.1). Nitrogen was the aerating gas and water was the liquid. The momentum flux ratio, $(\rho v^2)_{jet}/(\rho v^2)_\infty$ was held constant at 10. The 1-mm-diameter (d) injector sprayed up into the cross flow. The spray field was imaged from the injector to 25 diameters downstream, as well as downstream locations of 50 and 100 (x/d = 0…25, 50, 100). The uncertainty of the CCD location was +/-0.001in. The uncertainty of M, q, and GLR were all within +/- 5%. The spray was tracked to capture the flow field from the edge of the spray down to the tunnel floor.

Table 3.1 AFRL Test Matrix.

Test	GLR (%)	Mach #
A	0	0.3
B	4	0.3
C	8	0.3
D	0	0.6
E	4	0.6

Single view holographic microscopy, akin to Test Case #1, was used for these experiments; see Figure 3.4 for setup. Two Nd:YAG lasers (Continuum Surelite) operating at a 10 Hz pulse repetition frequency illuminated the test section; the laser beams were combined into the same path using a simple 50/50 splitter/combiner. Before entering the test section, the laser beams were focused through a pinhole to improve the homogeneity of the laser spatial profile. The holograms were recorded on a 16 Mpixel interline-transfer CCD camera (Redlake EC16000, 4872 x 3248 pixels) operating in double-exposure mode. Control of the beam energy was accomplished with a combination of Q-switch timing delay, a polarization beam splitting cube, and neutral density filters. A Uniblitz shutter was employed to select a single pair of pulses for camera exposure. System timing was managed by a pulse generator (Labsmith LC880). The time between laser pulses was varied between 1 μs and 6 μs, depending on the crossflow Mach Number. The entire optical system was placed on an optical breadboard beneath the transonic wind tunnel; the breadboard is mounted to a 3-axis translator so that the probe location, relative to the injector exit, can be varied.

Results of the near-injector holograms, meshed together for test condition B (aerated liquid jet, 4% GLR, 0.3 Mach cross flow), are shown in Figure 3.14. Each image covers a 5mm x 5mm area. A detail hologram is also shown. Note the circular interference fringes around each drop. Slices of the hologram, at different distances from the sensor, are reconstructed by using the digital reconstruction techniques of Schnars and Jueptner (2005). Three slices have been reconstructed in Figure 3.15 from the highlighted hologram shown in Figure 3.14. These images are reconstructed at the spray central plane and 3mm in front of and behind the central plane. The fine droplets in the upper right hand corner of the first image are in focus. These go out of focus with increasing depth into the spray (hologram). Because of the long depth of focus, out of focus images of surrounding drops appear in each image. The focal distance can be determined by the intensity distribution of the droplet image. The focal distance to each drop corresponds to its distance from the camera (span wise coordinate). The entire span of the wind tunnel is captured in one image. The reconstructed images can be meshed together to recreate the spray field. For example, the spray field of a pure liquid jet with a 0.3 Mach cross flow (test condition A from Table 3.1) is show in Figure 3.16. Likewise, the spray fields for the increased gas/liquid ratios of test conditions B and C are given in Figure 3.17 and Figure 3.18. The higher Mach number 0.6 spray fields of test conditions D and E are given in Figure 3.19and Figure 3.20.

The image space for these holograms was calibrated using the procedures outlined in Lee et al. (2009). The reconstruction distances to individual calibration pins were related back to the diameters of the pins. Measurements for multiple sets of images of the pins were plotted and the linear calibration curve relating the real space to the reconstruction space was fitted; see Figure 3.21.

From the figures, it is clear that these are difficult sprays to analyze because the jet core is near the edge of light transmission. There are drops of many sizes and sometimes clustered together. There are overlapping interference fringes, especially far from each drop's focal point which can falsely identify very large drops.

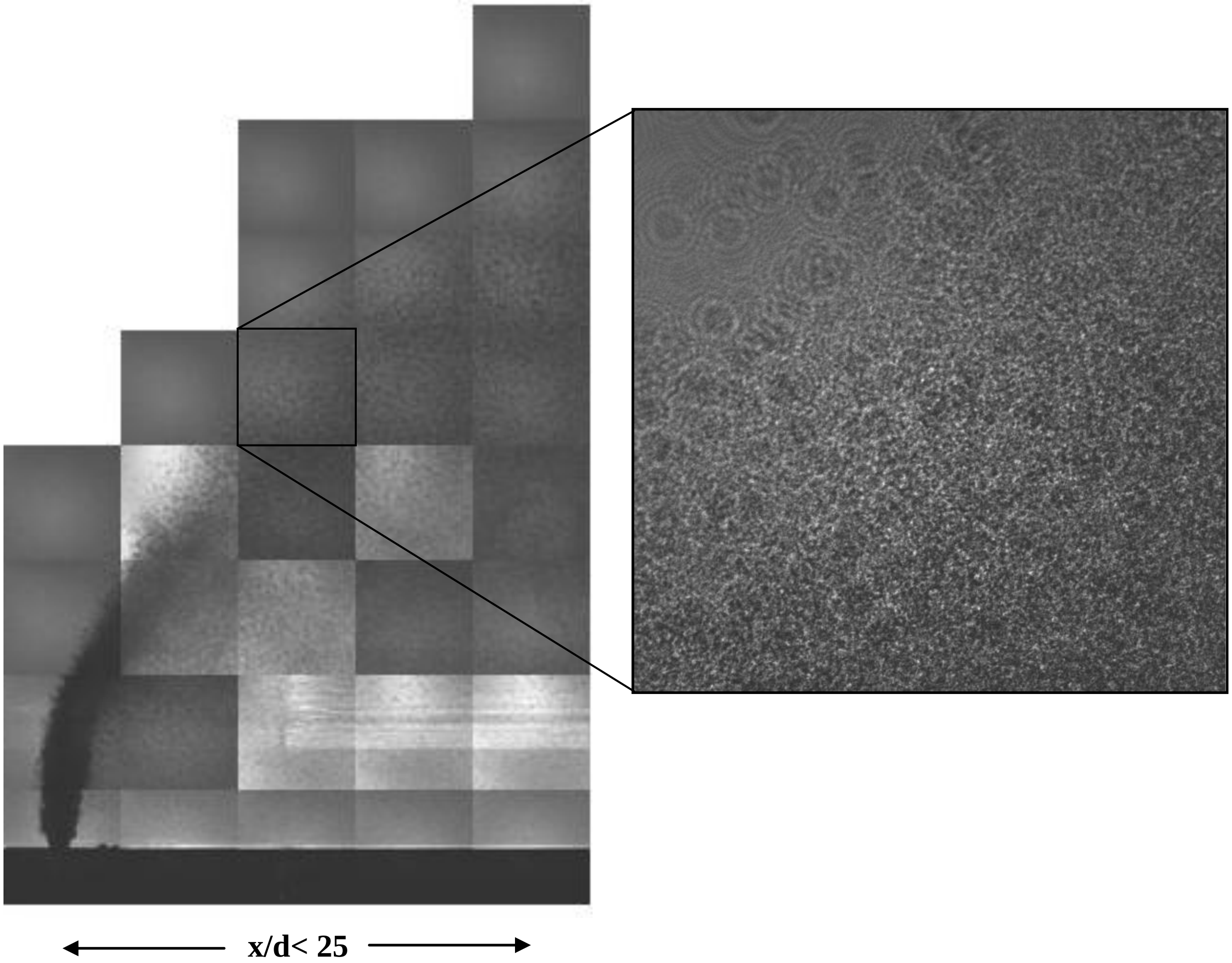

Figure 3.14 Combined Holographic Images of Test Condition B (M = 0.3, GLR = 4%, q = 10, d = 1mm) and Detail Hologram.

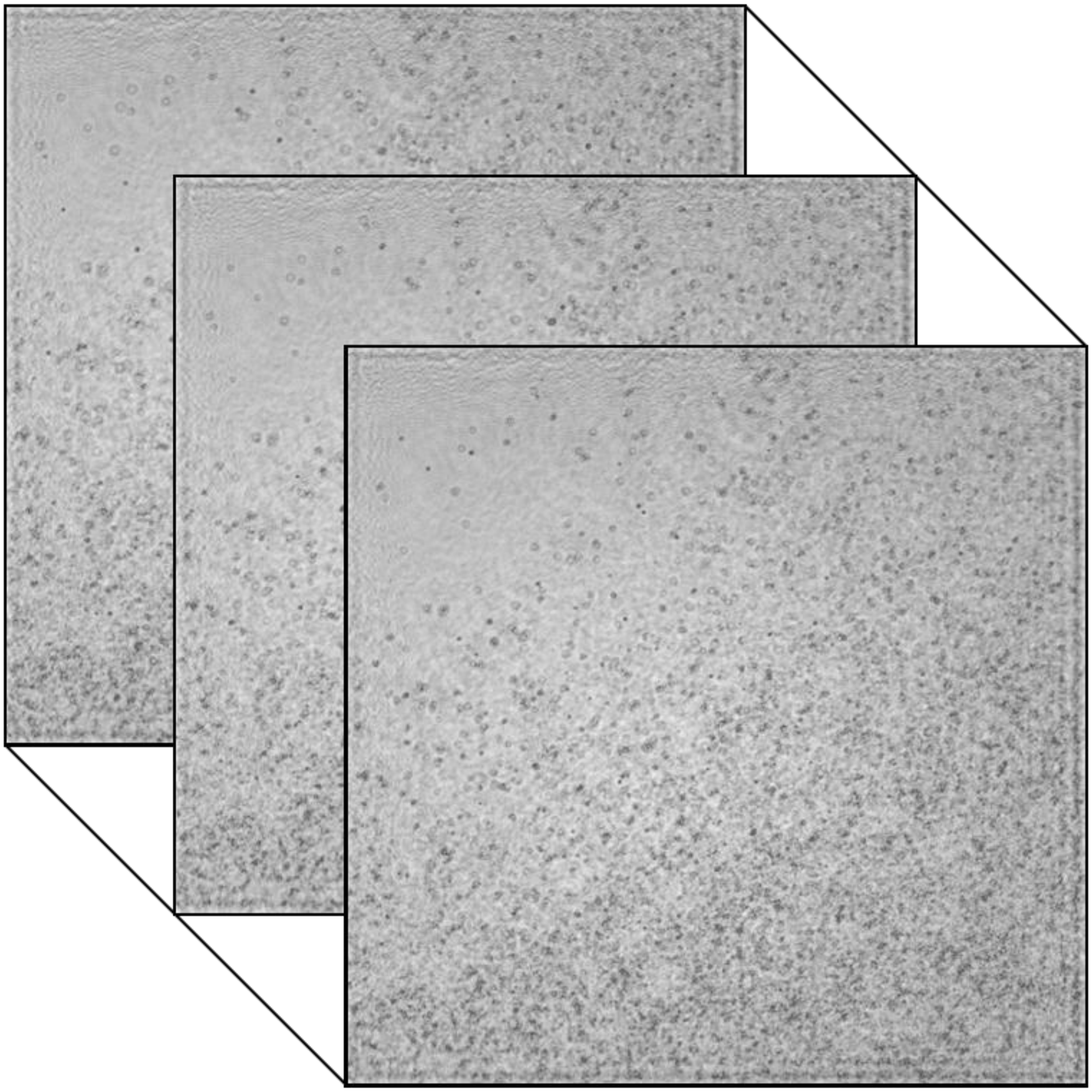

Figure 3.15 Reconstructions of Highlighted Location in Figure 3.14. 3mm Between Slices.

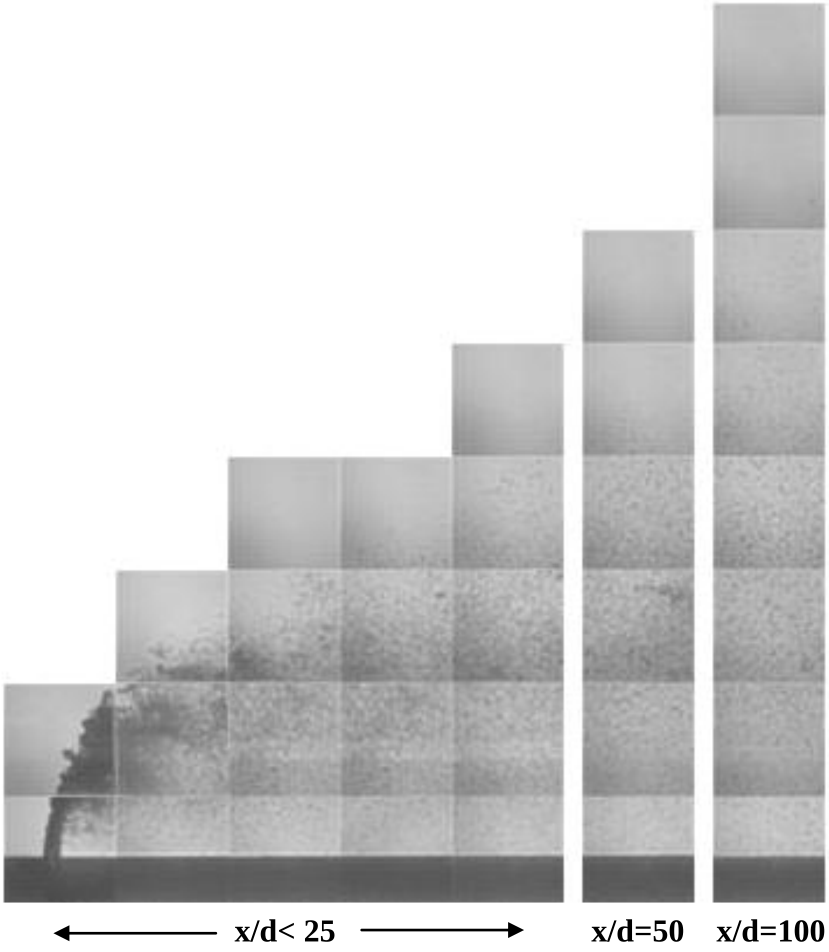

Figure 3.16 Combined Reconstructed Images along Spray Centerline of Test Condition A (M = 0.3, GLR = 0%, q = 10, d = 1mm).

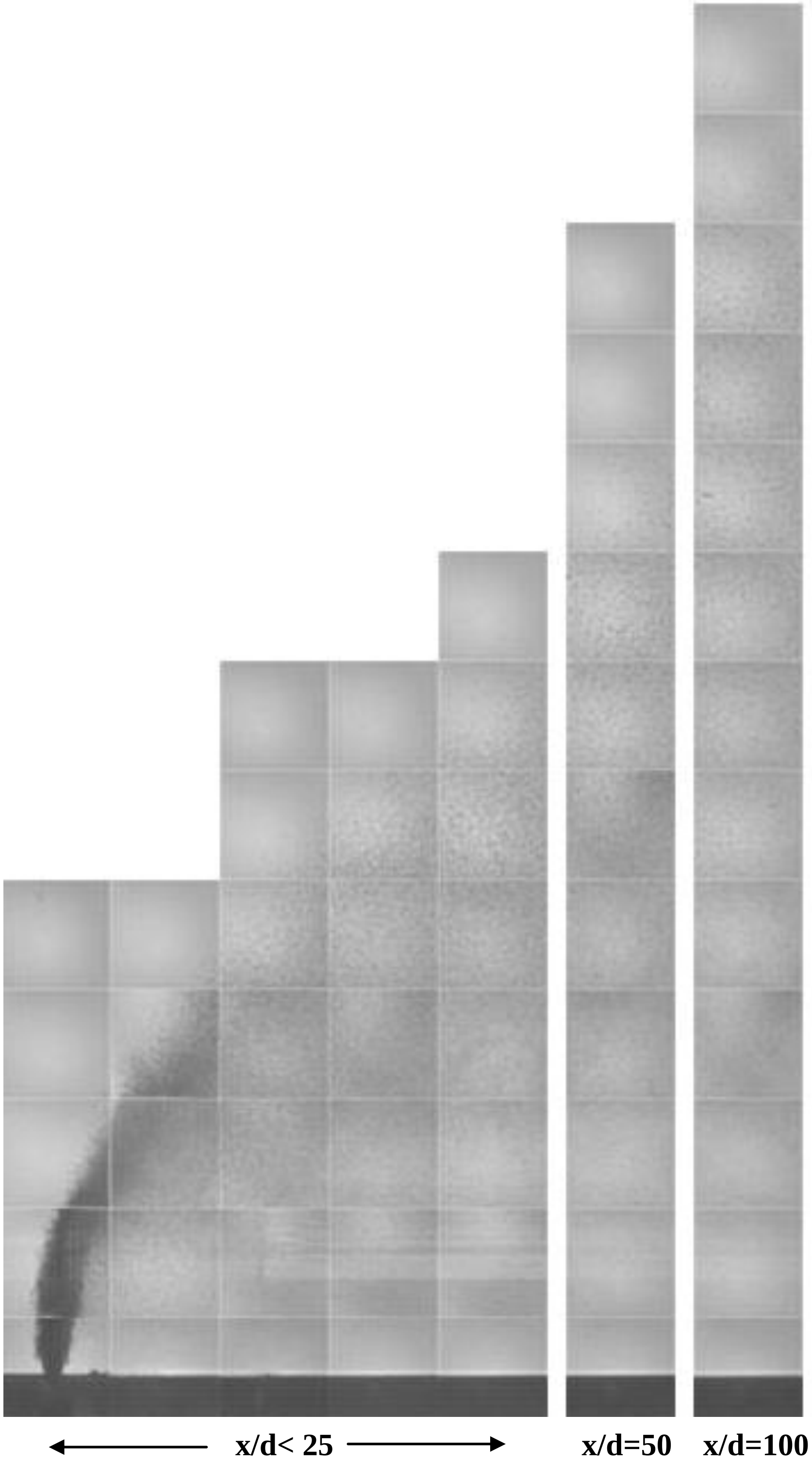

Figure 3.17 Combined Reconstructed Images along Spray Centerline of Test Condition B (M = 0.3, GLR = 4%, q = 10, d = 1mm).

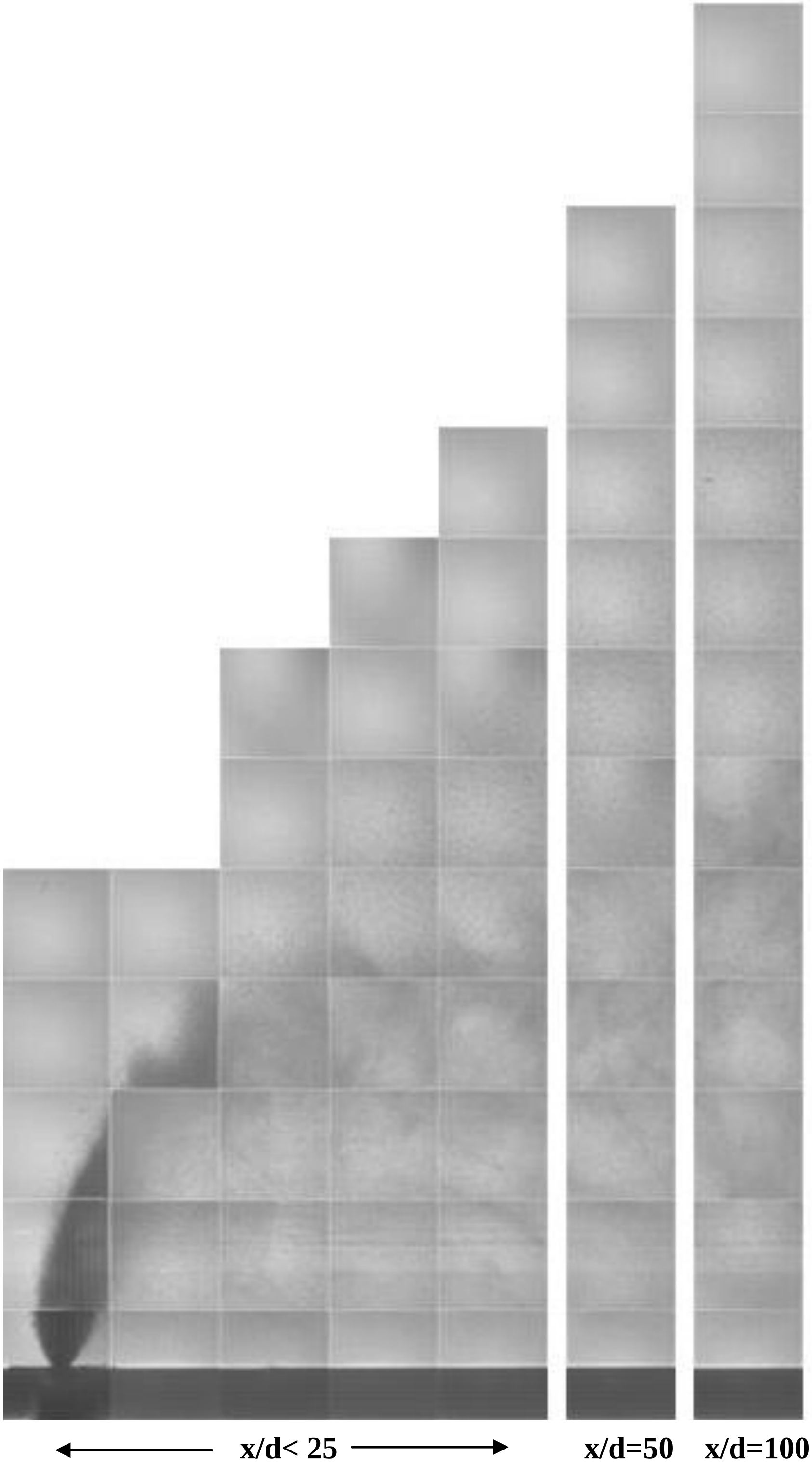

Figure 3.18 Combined Reconstructed Images along Spray Centerline of Test Condition C (M = 0.3, GLR = 8%, q = 10, d = 1mm).

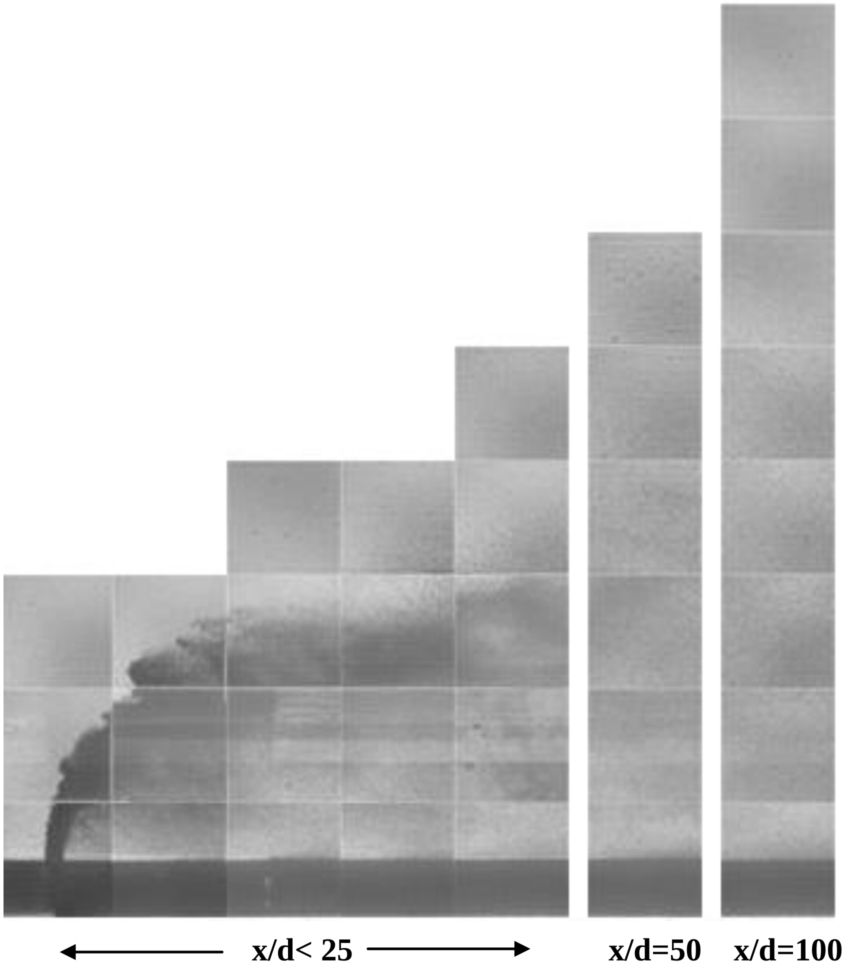

Figure 3.19 Combined Reconstructed Images along Spray Centerline of Test Condition D (M = 0.6, GLR = 0%, q = 10, d = 1mm).

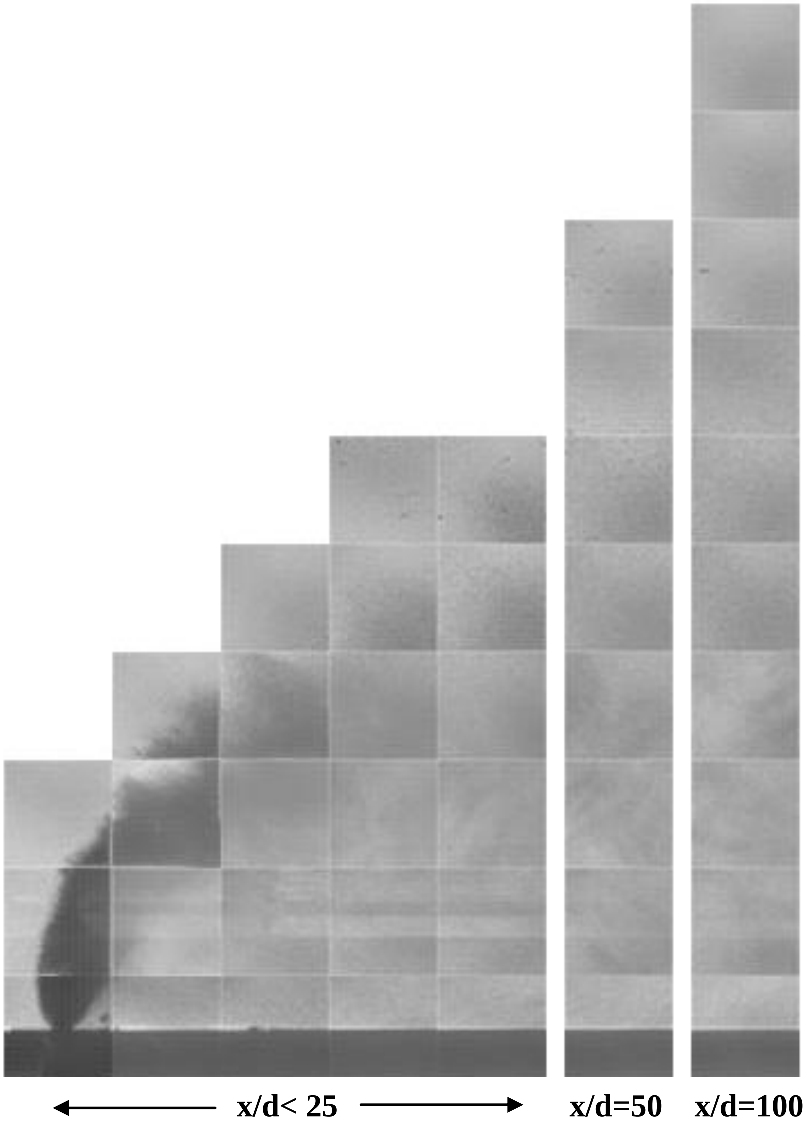

Figure 3.20 Combined Reconstructed Images along Centerline of Test Condition E (M = 0.6, GLR = 4%, q = 10, d = 1mm).

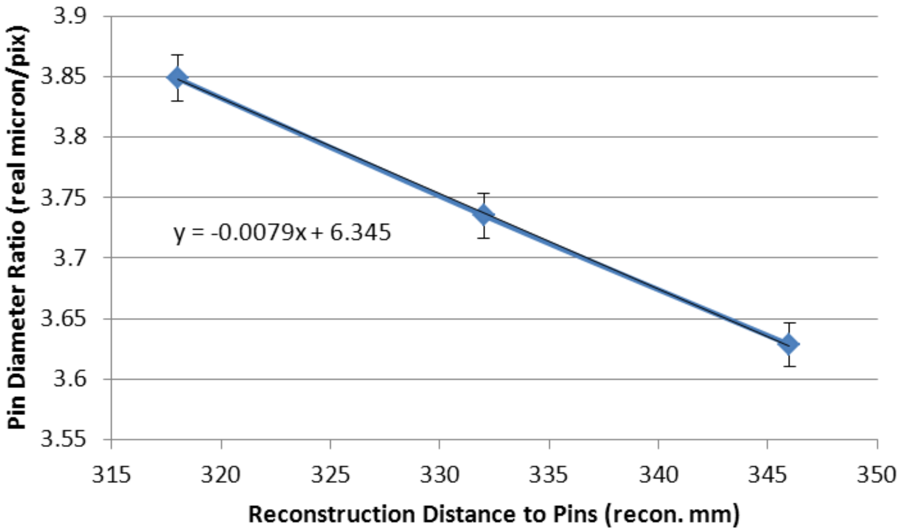

Figure 3.21 Hologram Image Calibration (99% Confidence Bars).

3.5 General Holography Experimental Concerns

The applied spray cases in Section 3.4 highlighted other general concerns which must be accounted for during the experiment setup. Because of the spherical wave front of microscopy, the distance between the objective lens and aerated jet must be minimized to maximize resolution, and the distance between the injector and the CCD is minimized to obtain as large a field of view as possible. As with any optics experiment, the optical mount structure must be absolutely rigid. The imaging system must also be well controlled as one microsec time delays for velocimetry were a maximum for the highest speed drops. The quality of the tunnel wall glass is critical. Several comparisons were made. Figure 3.22 is a hologram of the test section, but with the tunnel side glass removed. As expected, installing high quality float glass does not seriously degrade the image; see Figure 3.23. However, using a glass with small bubbles that are visible with a flashlight (despite otherwise quality glass) makes the image unusable; see Figure 3.24. Additionally, the lesser quality glass significantly skewed the focal plane of the wind tunnel centerline.

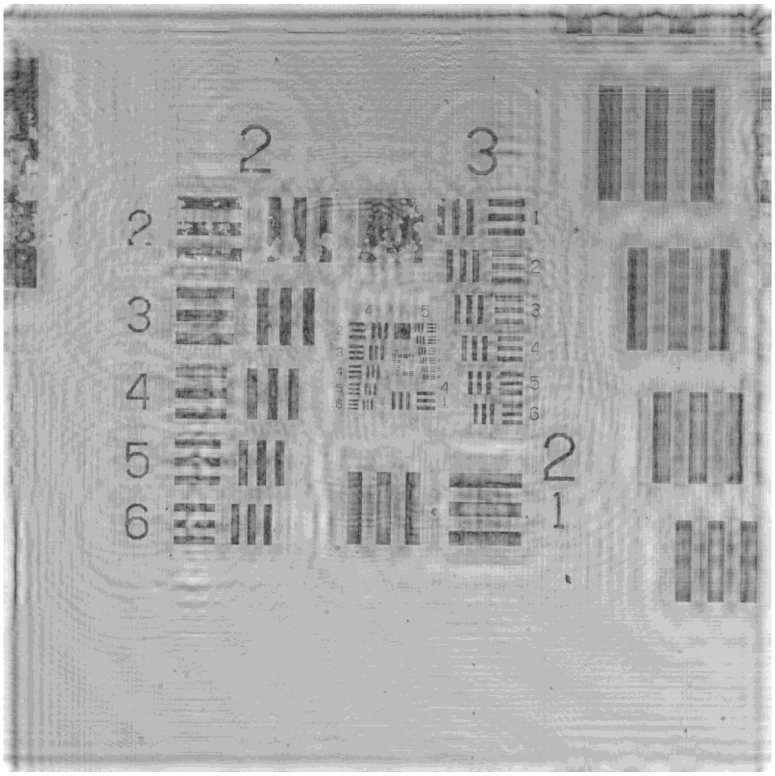

Figure 3.22 No Glass Hologram.

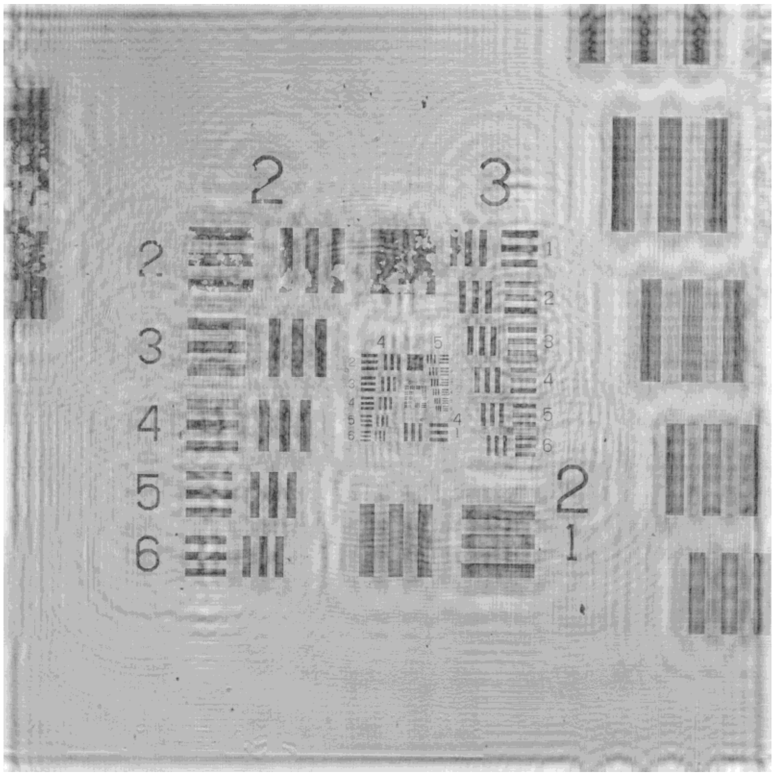

Figure 3.23 High Quality Float Glass.

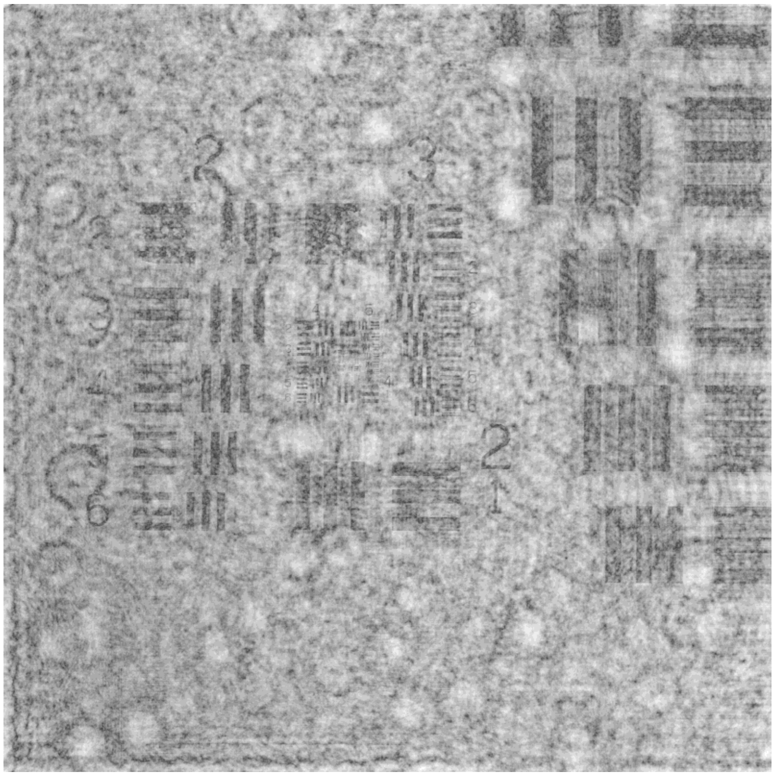

Figure 3.24 Optical Grade Fused Quartz.

Finally, care must be taken to ensure the hemispherical wave front is normal to the tunnel floor. It may even be preferable to align the pinhole so that the wave front propagates at a slight angle away from the tunnel floor. Since expanding beams are used, the light source may reflect off of wind tunnel structures and into the CCD. This effect is shown in Figure 3.25, where the spray can be seen in a hologram reflecting through the wind tunnel floor.

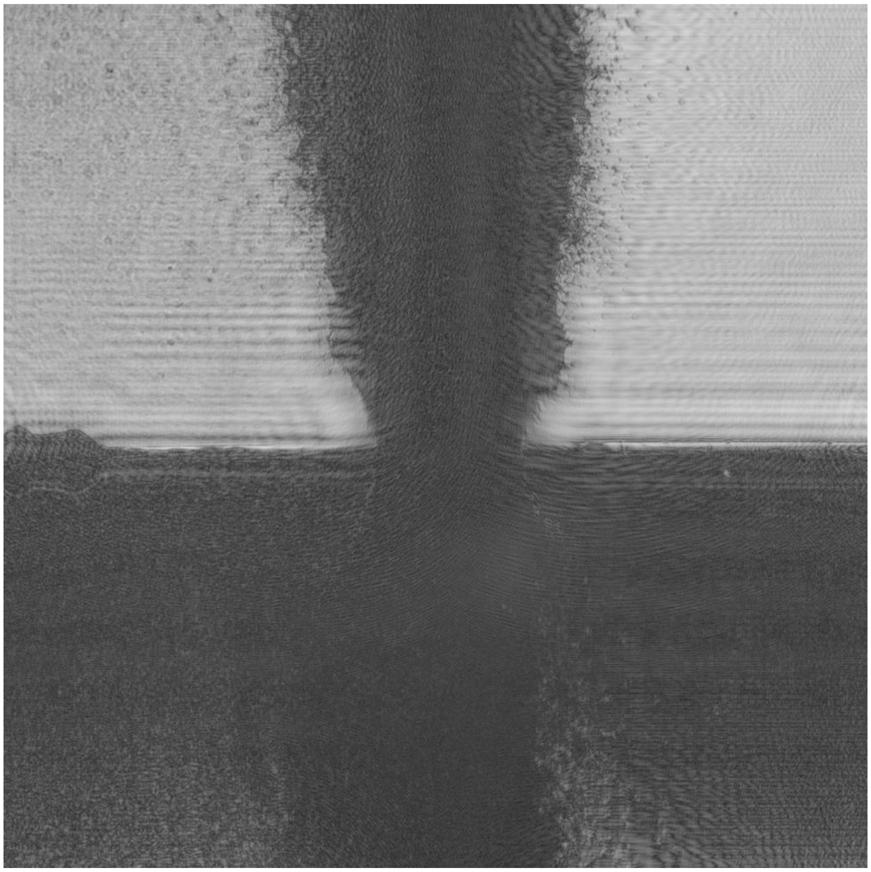

Figure 3.25 Reflections From Misaligned Laser.

Chapter IV. Algorithm Development

4.1 Introduction

To keep the algorithm development organized, this effort was broken into distinct subroutines that each contribute to mapping the spray. These are:

- hologram reconstruction
- droplet detection and 3D mapping
- droplet pairing for double view holography (if required)
- particle tracking velocimetry (if required)

These subroutines are described in the following sections. Then, the algorithm for near sprays is described in more detail. Finally, statistics and comparisons to other research groups are presented.

4.2 Noise Reduction and Edge Sharpening

The hologram and its experimental geometry are required user inputs for the algorithm. The hologram is then reconstructed at user specified intervals from the CCD using the convolution equations per Schnars and Jueptner (2005). The implementation of the reconstruction algorithm is based on the approach described by Miller (2006); see Chapter II. Before passing the images onto the second portion of the algorithm in which the drops are located, it is sometimes necessary to run routines which ease droplet detection. These are frequently run in conjunction with smoothing kernels to suppress isolated pixel intensity fluctuations (Forsyth and Ponce, 2003).

Image noise can be reduced by background subtraction. A drop image can be made clear by subtracting the blank image of the same location. This serves two purposes. It can remove unwanted images from the background and it reduces speckle noise. Ideally, the only objects left in the modified image will be droplets. This approach will not be effective if the image region changes during test or if test time and/or electronic storage are too valuable for extra holograms. An alternative that is also effective is background division. In it, the primary image is divided by the background image. Presumably the drops will be darker than their corresponding background, so an easily supportable threshold can be applied for edge detection. For example, it was found that when a pixel is 80% as bright as its background pixel, it was safe to identify it as part of a drop for edge detection.

An example of background subtraction is given in Fig. 4.1. Fig 4.1(a) is a reconstructed image of an Air Force Target. Fig. 4.1(b) is the same reconstruction, but with the target removed. Their difference is given in Fig. 4.1(c). Background subtraction can be a powerful tool because it produces readily segmented images while smoothing background objects. Unfortunately, capturing background holograms can be a time consuming process if it requires constantly stopping and starting the spray injection system, and reconstructing them imposes an additional computing burden if the background is not well composed.

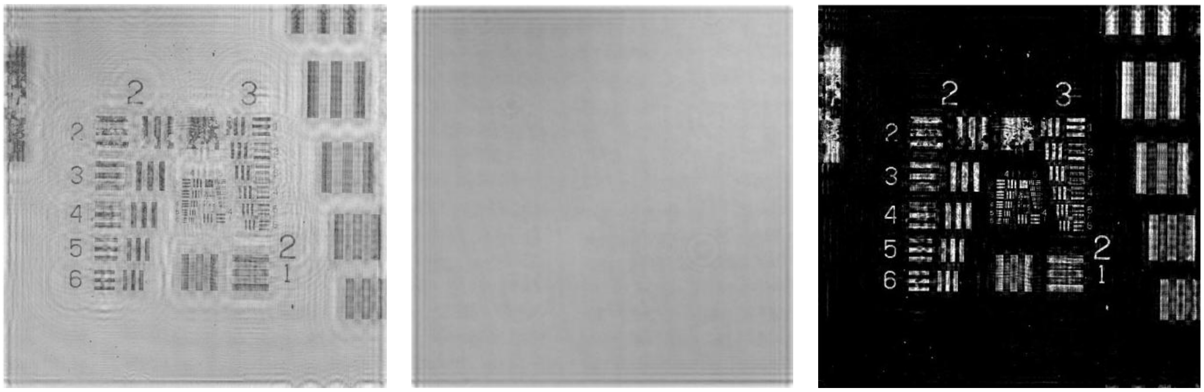

(a) (b) (c)

Figure 4.1 Background Subtraction.

Another approach which has been quick to process and effective is to enhance the contrast on drops with image addition. It has been found that the detection of droplet edges can be enhanced by adding successive reconstructions together. This smoothes the surrounding background, increasing the signal to noise ratio. Thus far, the optimal number has been all of the slices over a 10 mm interval across the wind tunnel test section. This operation has the effect of driving a droplet image darker, relative to its surroundings. This is demonstrated by Figure 4.2 in which the droplet images from Figure 3.2 have been summed.

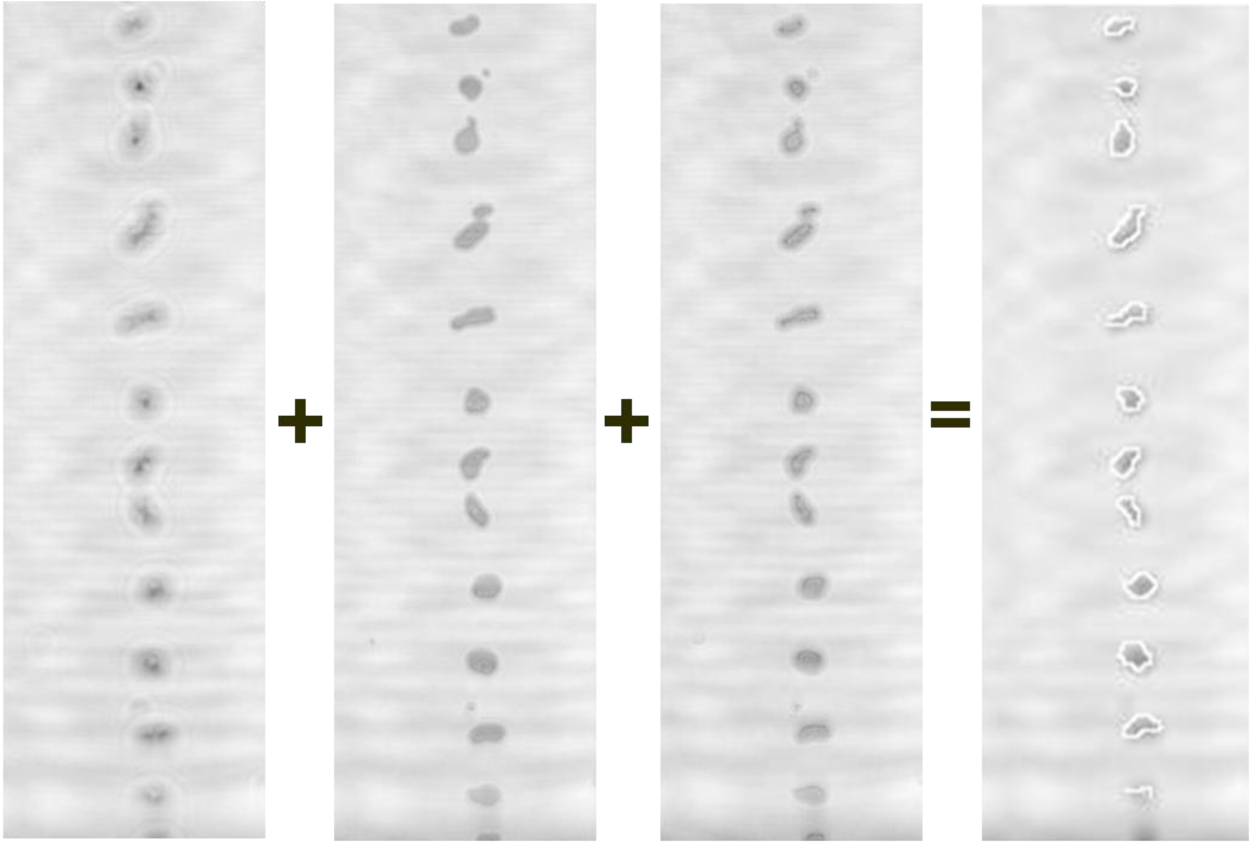

Figure 4.2 Reconstruction Image Addition Enhances Large Droplet Identification.

The out of focus neighboring slices (including Figure 3.2 a) and c)) surrounding the focused location (Figure 3.2b)) have been combined, as demonstrated in the first three images of Figure 4.2. The fourth image shows the summed image of all of the reconstructions as well as their detected edge outline. The final effect is to smooth the background interference pattern which could be confused for droplets in extreme cases and highlight larger droplets. Furthermore, the centers of the droplets are darkened, enhancing the contrast for later edge detection. While this may not produce images that are clearer than the focused image of a drop, performing this image addition step makes it easier to find larger droplets. Note that very small and faint drops can be washed out with this technique.

This approach is also an effective first step in sparsely populated holograms. If the analysis does not contain many objects in the 3D area of interest, key time savings can be realized by using this image addition approach to quickly identify regions in which objects exist. The speed gains are based on the fact that there is only one edge detection performed on the summed image versus edge detecting every reconstruction. These small regions of interest (ROI) can then be interrogated with more complex methods. ROIs may also be used to store 3D subsets of the larger hologram for computers which do not have sufficient memory to store all of the reconstructions in one large array. Image matrix reduction (i.e. Garcia-Sucerquia et al., 2005 and others) is also effective at reducing image sizes enough to store them in RAM.

4.3 Three Dimensional Data Calculation

Once the hologram has been reconstructed at a predetermined number of slices and any image preparation has been done per Section 4.2, the algorithm detects possible droplet locations. This breaks down into two primary areas, as described in the following sections. Section 4.3.1 describes the routines for identifying droplets within a slice, regardless of whether the droplet image is focused. The droplet size and centroid within the image plane are also calculated. Section 4.4 compares the results of Section 4.3.1 from slice to slice. The primary function of this subroutine is to identify which slice is most in focus. Then, the droplet's span wise coordinate is identified and its in-plane size and location is catalogued. In this way, the entire hologram droplet distribution is mapped and passed on to other programs for droplet pairing (double view holography), velocity calculations (PTV), etc.

4.3.1 Droplet Identification

The key portion of this part of the algorithm is to identify the regions of interest (ROI) which may contain droplet images (regardless of focus). In near field sprays, the ROI may be the entire hologram. In order to reduce the number of false positives, it is not uncommon to subtract a background image of the hologram. Unfortunately, it was found that, without extensive image preparation and alignment, the resultant image matrix could contain many pixel scale irregularities that required additional smoothing. Most droplets are not obscured by these irregularities, but rather the false positive rate spikes if they are not eliminated. Furthermore, there are times in which a blank, background, hologram is not available. For example, test facility time may be at such a premium that taking strictly unnecessary images is time prohibitive. So instead, this algorithm uses an averaging filter to smooth the reconstruction itself. A kernel size of about 25% of the expected diameter has been effective (kernel of ~4 pixels for the current study). Note this is a very soft requirement; it is more important that very small droplets are not completely filtered. Finally, a binary filter is applied to the smoothed image. A typical value for droplet pixel intensity is used for the threshold. This is a user supplied value, but it is easily found directly from the image.

The resultant image is segmented, dilated, and eroded to combine pixels belonging to the very dark gradient from interference fringes compressing together near the drop edge (Forsyth and Ponce, 2003, Gonzales et al., 2004). Hence, a binary image of the reconstructed slice is created. Discrete droplets are identified in the new image and interrogation areas are defined around the centers of each droplet. It is important to note that at this point in the algorithm, it is acceptable if the image smoothing and simple thresholding distorted a detected drop's size; the objective of the current routine is to simply identify ROIs that may contain drops. The final droplet area and centroid will not be calculated until the drop's span wise location has been determined.

Once a list of regions of interest have been built, the algorithm performs a Roberts edge detection within each ROI. Robert's was chosen as it is the fastest edge detection routine that detected drops without giving too many false positives. Miller (2006) and van Hout and Katz (2004) used Sobel and Canny edge detection, respectively. It was found that these routines are too sensitive given the noisy nature of near field holograms. Furthermore, corner detection is not a concern for this project. Other, more advanced recognition methods, such as PCA or Hidden Markov (Forsyth and Ponce, 2003) were not necessary. Furthermore, these methods are limited in the near field as the droplet shape is not always known.

4.3.2 Droplet Size and Image Plane Centroid

When the edge detection routine finds a droplet, the size and location can be measured. These values are used to track and order the drops until the final measurement is made. The droplet area is simply the number of pixels encompassed by its detected edge. The equivalent diameter and (x,y) centroid are calculated directly from the detected image. Note that the calculation can be complicated by the irregular and distorted cross sectional profile, as noted by Sheng et al. (2003).

4.4 Identifying Depth of Focus

At this point, every slice has been searched for possible droplets. Obviously, most of these identified droplets are simply the out of focus images of a focused droplet. What is required is a method for identifying the most focused image of each drop.

4.4.1 Centroid Calculation for the Span wise Coordinate

Sheng et al. (2006) proposed using the centroid of the collective mass of a detected drop along an axis parallel to the camera. This approach is logical given the cigar shape of a drop's depth of focus (Sheng et al., 2006). However, it proved problematic for the current effort; see Figure 4.3.

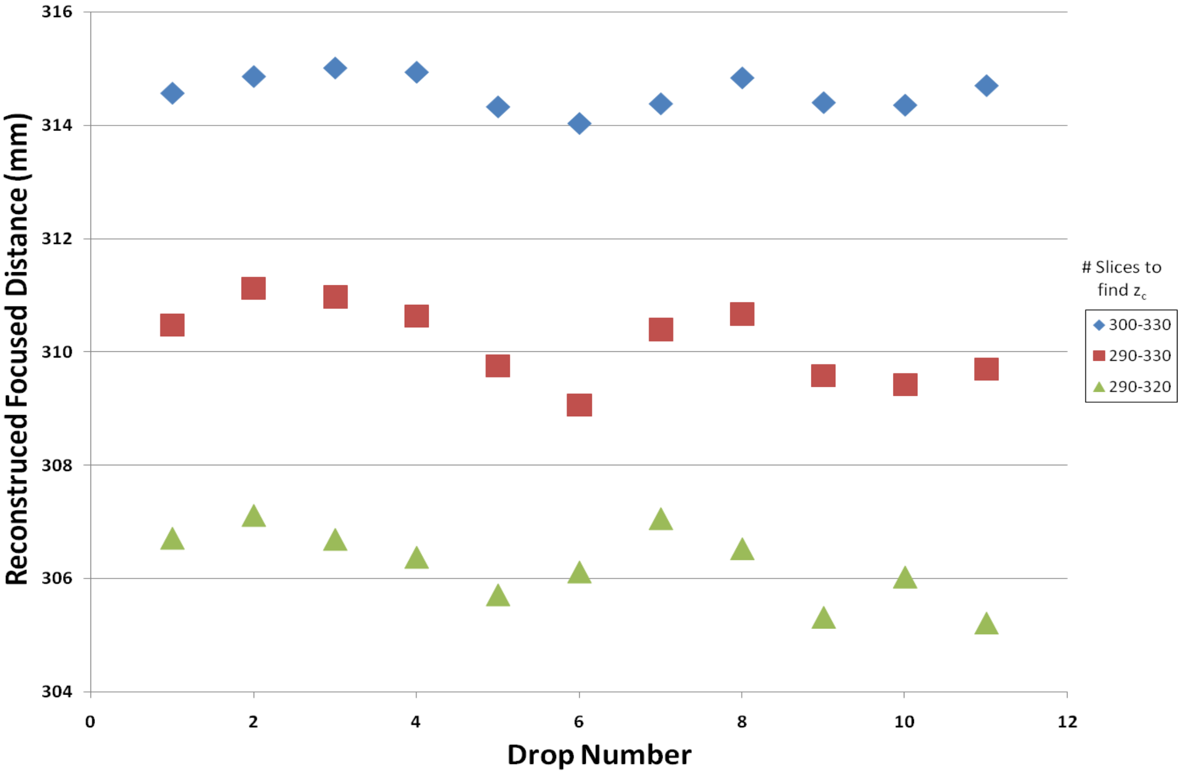

Figure 4.3 Sensitivity of Spanwise Centroid to Number of Slices for Focused Coordinate Focused at 311mm.

The centroid was calculated for a set of droplets. Each drop had three cases in which the span of slices was varied. Effectively, the location of each drop was shifted as the range of slices for the centroid calculation shifted. The bottom eleven drops from Figure 3.2b were studied; these are represented by the "Drop Number" axis in Figure 4.3. The three different cases are represented by the three different scatter plots. The y-axis gives the calculated span wise centroid for each drop. The wave from one drop to the next is acceptable and is reflected in the hologram and is repeated in each case. The focused location for all of the droplets is around 310mm. Therefore, the centroid calculations that were performed for drops approximately in the center of the range were accurate. However, the accuracy decreases rapidly as the bounds of the centroid calculation were changed. When comparing these results to Sheng et al. (2006), Sheng used a much tighter span wise range reflective of the limited test section size. Sheng et al. (2006) may have also had a more restrictive threshold for which pixels are counted toward the centroid. Regardless, Figure 4.3 is instructive, for a spray algorithm cannot rely directly on a centroid calculation to find the drop's span wise location if the depth of focus crosses the span of all available reconstructions. The centroid calculation is still useful once the span wise location is approximately found.

In summary, because of the long depths-of-focus, an intensity based span wise centroid calculation will include many pixels detected at very long distances from the true location. For example, the long depth of focus/large drops of test case #2 are present in the entire hologram reconstruction space. Hence, the centroid result will be erroneously shifted toward the center of the calculated region. However, the shift is not so severe that the method cannot be used if the true centroid is near the center of the calculated region. So, the approach of Sheng et al. (2006) is effective if a subroutine centers the centroid calculation by first finding the drop's approximate span wise coordinate. The advantage of using the centroid is it is less sensitive to fluctuations from reconstruction to reconstruction. For example, intensity statistics based on an undersized area will not capture very dark, crisp edge pixels and will be skewed by lighter/higher variability pixels towards the center.

4.4.2 Area Calculation for Span wise Coordinate

The size can be used to narrow the range for the droplet span wise location. Figure 4.4 identifies the example droplet to be investigated in Figure 4.5. Figure 4.5a shows a series of images of this drop as it goes further from the camera. Note the drop comes into focus in the center, boxed, image, and then goes back out of focus. Although not this small, this cropped area is analogous to the ROI from Sections 4.2 and 4.3.1. The next line of binary images, Figure 4.5b, shows the results of edge detection on each unfocused drop. Edge detection within this area quickly identifies that the focused location corresponds to the one with the largest detected drop. This is logical as the area measurement is, at its heart, edge detection. The slice with the largest drop image will be the one with the most well defined perimeter, furthest away from its centroid. This follows Leith and Upatnieks (1965) requirement that the most focused image correspond to the location with a well-defined, dark edge around the drop.

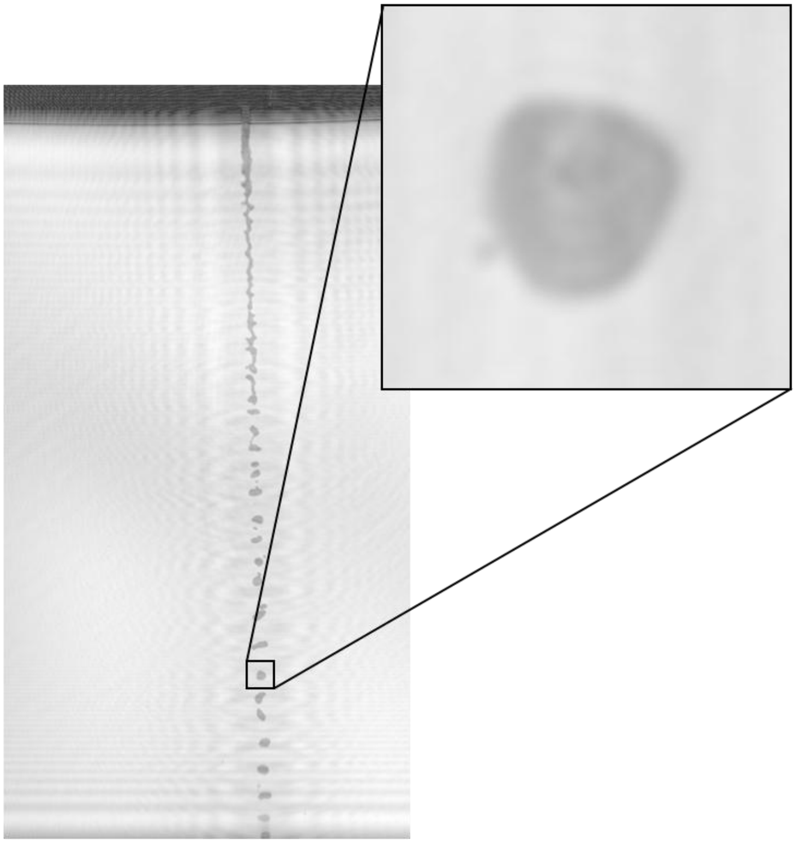

Figure 4.4 Droplet Identification for Analysis in Figure 4.5.

Several other observations can be made using Figure 4.5. The algorithm results from Section 4.3.1 will contain what appear to be many small drops in addition to the true, focused

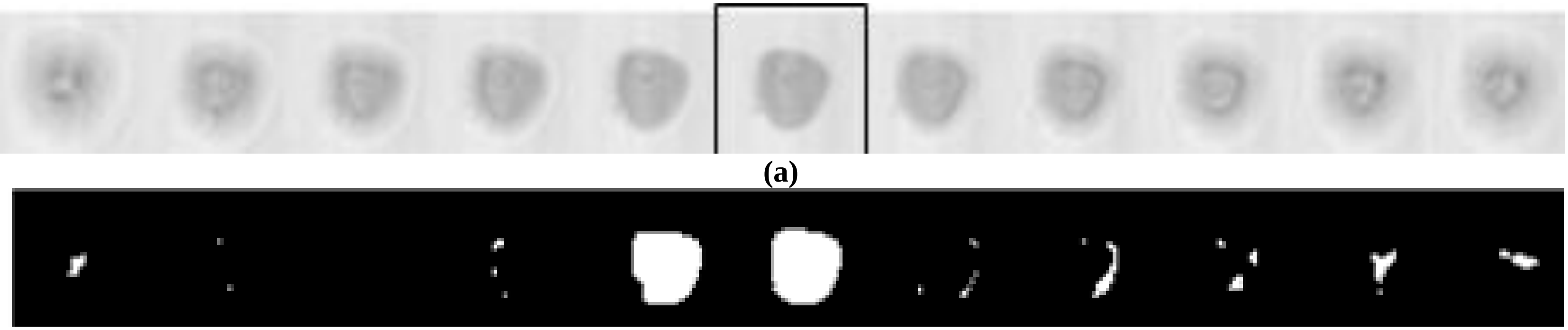

(a)

(b)

Figure 4.5 Span wise Location by Size.

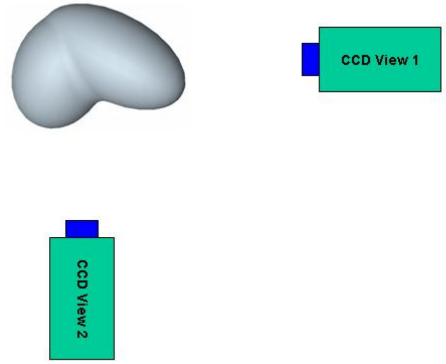

Figure 4.6 Orthogonal Views Are Necessary To Fully Characterize a Non-Spherical Droplet No Additional Cameras Are Necessary.

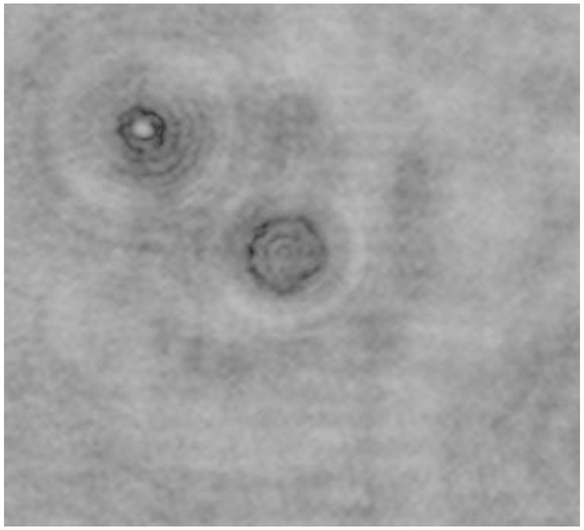

Figure 4.7 Near Focus Drop (from Fig. 3.15) Whose Edge Detection Is Interfered By Nearby Fringes.

drop in a nearby slice. By tracking the pixel coordinates within the image plane, the largest drop image will overlap these smaller, false positives. This is advantageous as this algorithm applies to transmission holography. If a small drop exists between a larger drop and the CCD array, it will be overshadowed by the large drop. Hence, any drops that overlap with another, larger drop are to be neglected. Furthermore, double view holography characterizes a drop to its fullest extent; see Figure 4.6. Only the outline of the droplet can ever be identified. If there is a structure located on the center of the surface of the droplet, the orthogonal camera will capture it.

4.4.3 Pixel Intensity Statistics Calculation for Span wise Coordinate

This largest area metric (Section 4.4.2) for calculating the span wise coordinate is effective for the clean and relatively short depth of focus of the drops in Test Case #1 (Figure 2.2). Unfortunately, the largest identified area criterion is less effective for the very long depth of focus drops in Test Case #2 and #3 (Figures 3.5 and 3.6, Figures 3.9 and 3.10). As the size measurement is driven by edge detection, it is susceptible to errors that distort the droplet edge. For example, Figure 4.7 shows a near focus drop at the center of the figure; it has been cropped from the lower right hand corner of Figure 3.15. The horizontal fringes and interference pattern from the nearby drops impose dark spots on the edge of the centered drop. The edge detection run on this portion of the ROI will result in the misidentification of the reconstruction slice with the largest image. The interior of the droplet image is not as sensitive to the surrounding conditions. Hence, a criteria based on the intensities of the interior pixels may be a reliable, and easily obtained, value.

First, the droplets from Case #1 were analyzed. The pixels encompassed by the largest cross section image were tracked across the span wise direction, centered on the drop focused location. The intensity distributions of these pixels were collected and statistics were calculated.

For each droplet at each slice, the intensity average, standard deviation, skew, and kurtosis were calculated. The slice spacing is approximately half of the droplet diameter. Results for one such droplet is given in Figure 4.8. What is immediately evident is that all of the statistical values show a marked reaction near the focused location (zero on the x-axis). However, the kurtosis has a sharp peak whereas the skew and standard deviation are more sloped. The average intensity is at a minimum (supporting the approach of Muller et al., 2004 which uses intensity thresholds and regressions of the span wise intensity profile). Unfortunately, it oscillates so quickly that a global optimization subroutine on the intensity would easily be trapped into one of the neighboring valleys. The other statistics cross zero at the focused location.

This same analysis was performed on the double view holograms in Case 2 and Case 3. In all, 90 droplet images of varying sizes were found in both views of 25 hologram pairs and the dripping case. The representative pixel intensity statistical results for these long depths of focus droplets are given in Figure 4.9. Again, the kurtosis crosses zero near the focal point. However, the standard deviation and skew do not have strong responses near the focal point; this phenomenon was found several times on the drops in Case 2 and Case 3. The average intensity also does not always correspond to the focused location. This could be explained by slightly darker edges or speckles within the drop boundaries that pull the average over. Likewise, the locations of the largest detected drop reconstruction (vertical lines) are shifted away from the droplet focal point. Importantly, note that all of the statistical curves vary much greater for the long depth of focus Case 2 and 3 than for the shorter depth of focus Case 1.

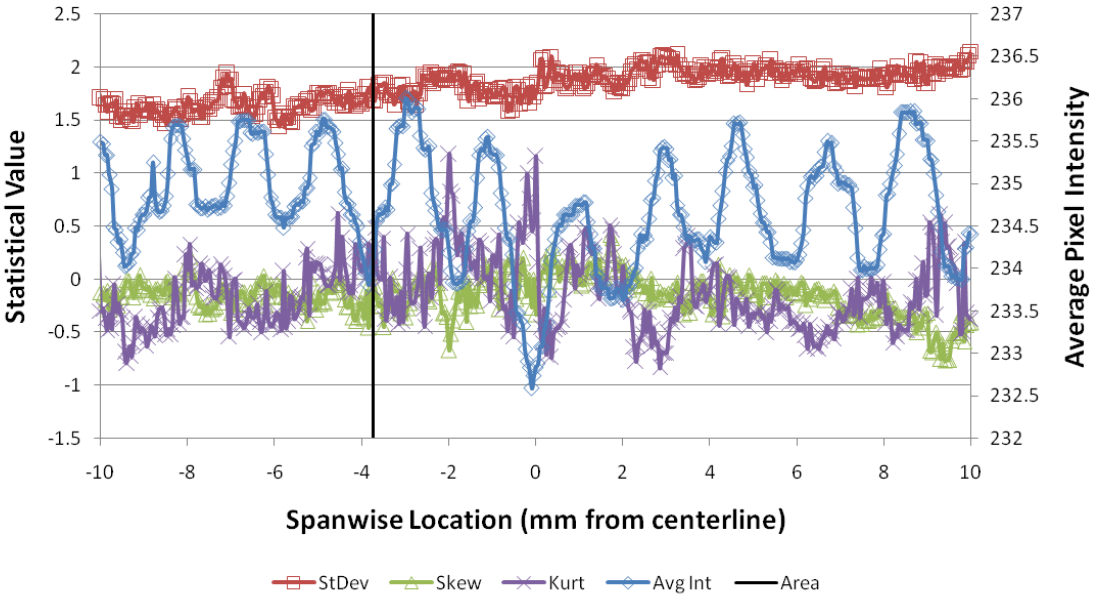

Figure 4.8 Statistical Profiles of Test Case 1 Representative Droplet Images in Each Slice Across Test Section Span.

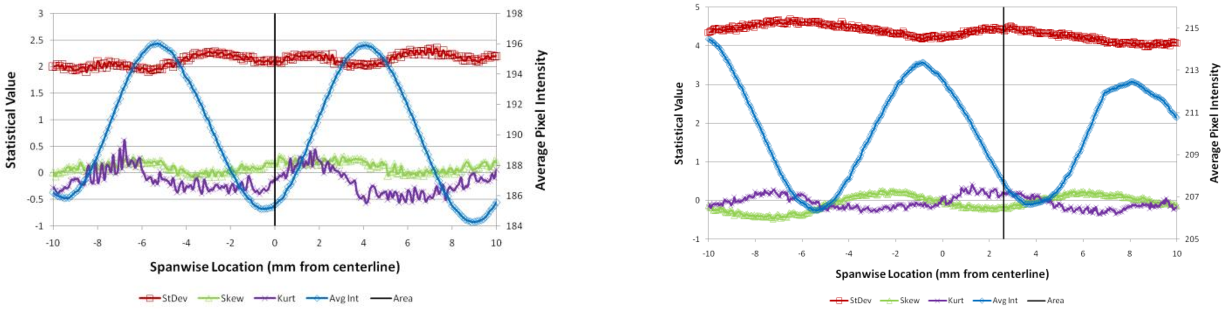

(a) **(b)**

Figure 4.9 Statistical Profiles of Test Case 2 and 3 Representative Droplet Images in Each Slice Across Test Section Span.

The error for all of these possible criteria, for all of the droplets in Cases 1, 2, and 3 are plotted in Figure 4.10. Clearly, there are a wide range of errors and criteria that works well for one drop but completely fails for another drop (i.e. minimizing the standard deviation criteria). However, there are three criteria that consistently perform better than the others. As has already been hinted at, using the droplet slice with the largest detected area works for larger drops and minimizing the average intensity calculation minimizes the error for the smallest drops. The size and maximum criteria were kept from Figure 4.10 and re-plotted in Figure 4.11. Note that for many cases, both criteria work well for identifying a drop's location and the average error is fairly low. Under the right circumstances of depth of focus and laser expansion, it is possible that the more involved statistical measures would not be necessary. Unfortunately, every result has a comparatively high uncertainty; see Figure 4.11. Note that because of the very long depths of focus in some holograms, this error is about half of the visual uncertainty of the drop location. In terms of the visual uncertainty, these results have the same or less span wise error as those of Lee et al. (2007).

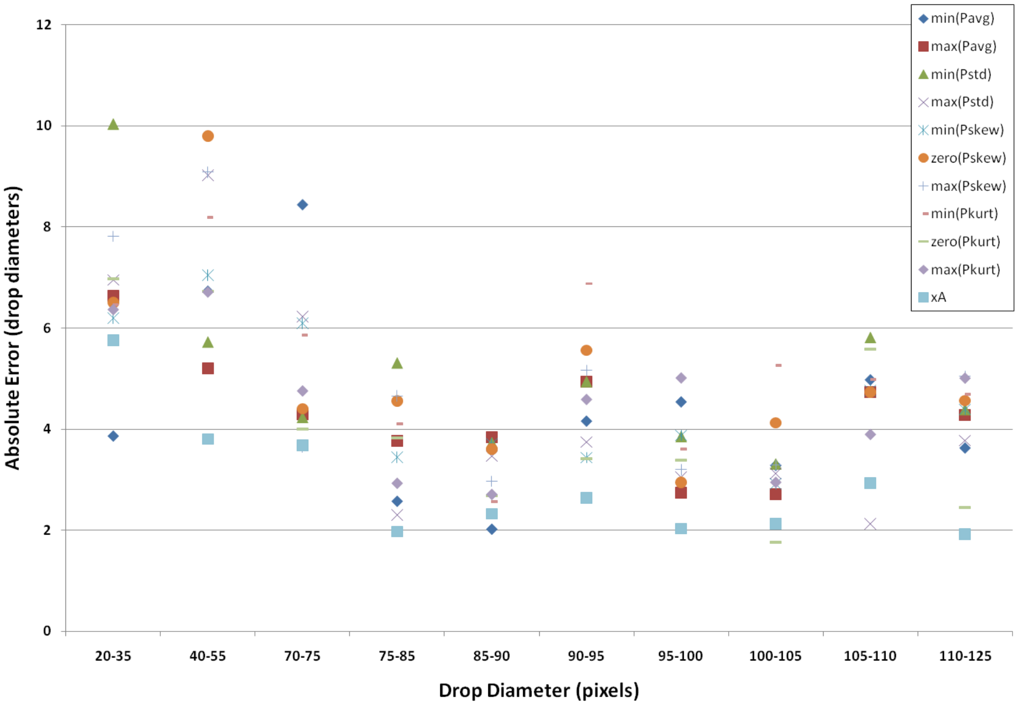

Figure 4.10 Absolute Errors of Spanwise Location Calculation Criteria for All Drops in All Cases.

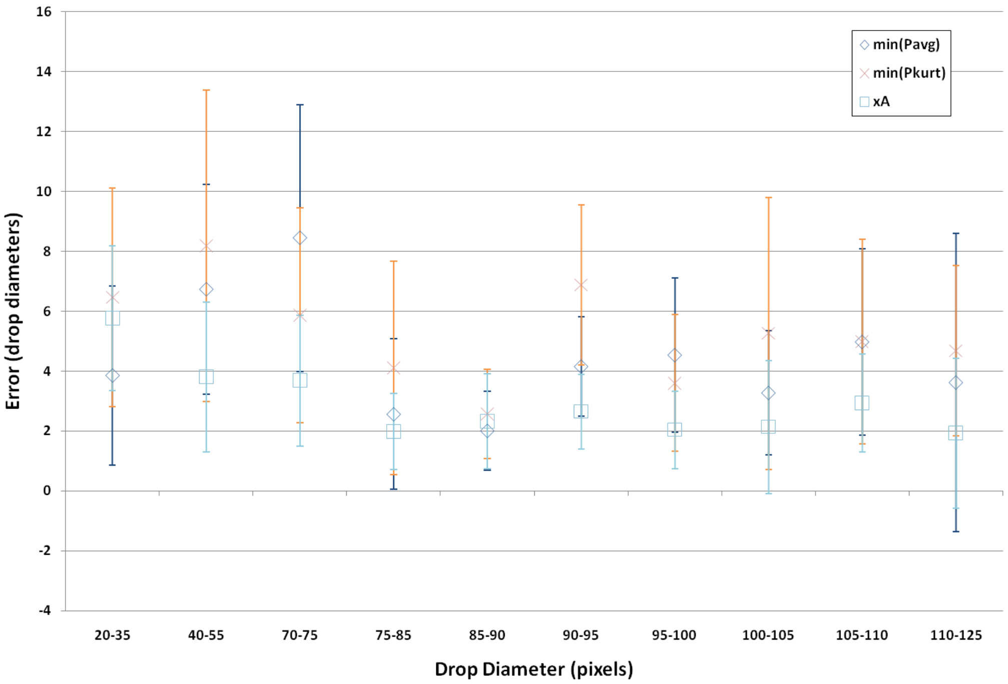

Figure 4.11 Minimum Intensity, Minimum Kurtosis, and Image Size Absolute Error of Span wise Calculation Criteria for All Drops in All Cases.

The high deviation comes from the variety of drops and images encountered. A drop can appear very dark by shadowing the laser, but as the light is bent around it, the image within the drop edges will change. Depending on the size of the drop and its position relative to the light source and camera, the drop's appearance could be very dark or have a bright spot form at the focused distance. Pixel intensity statistics can efficiently find focused drop locations; but, one must be careful to tailor the criteria to specific types of drop images.

4.5 Filter False Positives with a FFT Threshold Filter

As has already been discussed, excessive noise can interfere with the algorithm's ability to distinguish true positive droplet identifications from false positive identifications. The simple solution is to remove these false positives at the expense of losing true droplets (e.g. size filtering). Obviously this severely impacts the number of drops detected through the final calculations. Others use a trace of moving particles to classify true positives and find a centroid form the trace (e.g. Malkiel et al., 2004). Unfortunately, even if traces were available, the near field holograms would quickly become too noisy to process.

Another approach that has been developed during this project is to apply an FFT filter to distinguish real (albeit possibly unfocused) drops from false positive noise. It takes advantage of the interference pattern inherent to holography. The spaces surrounding drops are filled with interference fringes which complicate image detection; see the region between drops in Figure 4.7. This fringe pattern is centered on objects within the imaging space; false positive detections that are caused by overlapping fringes will not have the same symmetry and structure. So, it is proposed that the existence of a structured fringe pattern associated to a detected drop can be used to filter out false positives.

Referring to Figure 4.7, an analysis of the fringe pattern surrounding a drop is not readily implemented into the algorithm for a variety of reasons. There is no natural boundary for characterizing the extent of possible fringes. Additionally, the interference fringes can be obscured by other fringes as well as neighboring droplets. However, in digital holography, the echo of these fringes is reflected inside the boundaries of the detected drop; see arrows in Figure 4.12. In a real drop, these fringes are repeated inside the drop edge at a constant frequency. This problem is well suited for a Fast Fourier Transform (FFT) analysis.

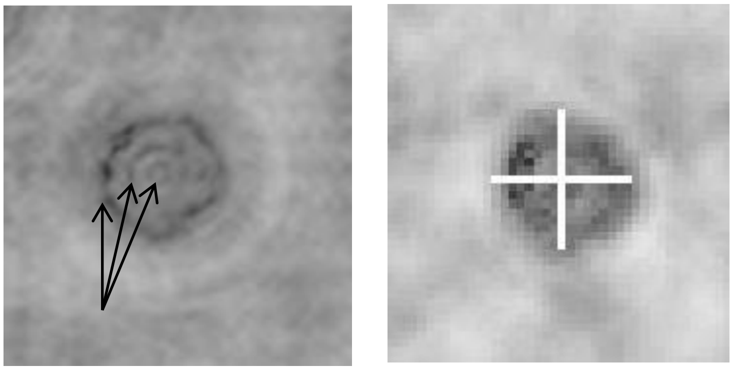

Figure 4.12 Repeating Interference Fringes within Drop Boundaries.

The steps of the subroutine are:

- Catalogue the size, location, and orientation of each detected drop.
- Calculate a linear equation through each drop's centroid, normal to the orientation of the drop's major axis. Note Matlab's command to find the minor axis of an ellipsoid does not guarantee that the minor axis is normal to the major axis.
- Calculate the length of the new line and identify the pixels intersected by the line.
- Record the intensity profile of this minor axis.
- Perform an FFT on the minor axis intensity profile.

Note, the image profile is taken at a right angle to the major axis of the drop so that if the object under study expands to the edges of the image frame, the fringe pattern will still be detected along the minor axis. The calculation speed is also improved by querying the line of pixels instead of all of the pixels within the drop; see Figure 4.12.

An example of a (real) detected drop is marked by the cross in Figure 4.12. This drop has an area of 145 pixels. Its intensity profile demonstrates a clear and repeating fringe pattern; see Figure 4.13. Because of this, the FFT plot is dominated by one frequency. It has been found that a user defined threshold of the FFT is sufficient to determine a false positive. If the frequency space of these holograms is dominated by any pattern greater than 790 (max(real(FFT(profile)))>790), then it is determined that the image belongs to a real droplet. The image information is kept and used to determine the exact 3D location of the drop using the methods discussed elsewhere.

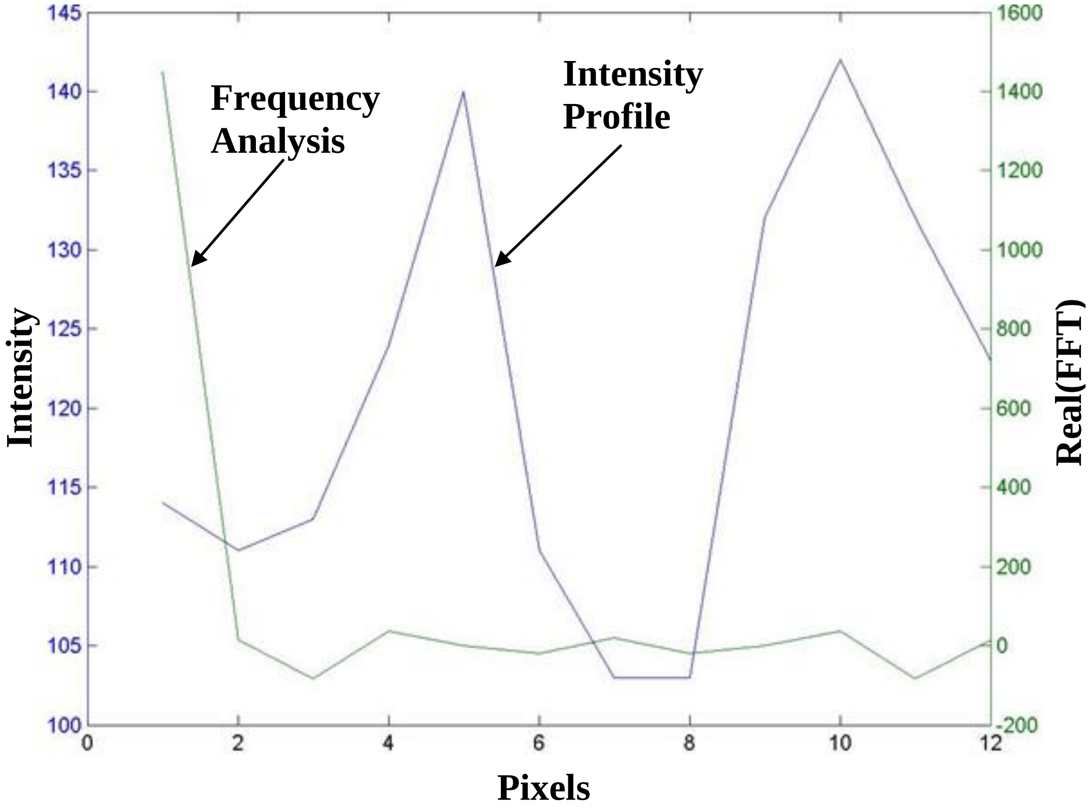

Figure 4.13 Interference Fringe Profile Frequency Analysis of Real Droplet.

Consider the circled area in Figure 4.14. This is initially a falsely identified droplet due to overlapping fringes and an unfocused drop in the background. This is a typical false positive. The intensity profile and Fourier Transform of this detected area are given in Figure 4.15. As there is no dominant frequency in the sample, this drop will be removed from any future results. Finally, while many false positives only exist in one reconstruction and then disperse in neighboring slices, this was an example of a false positive drop detected in the same area of the image plane, across a sequence of reconstructions. This observation forces the user to maintain as many reconstructions as possible for span wise accuracy and proper initial filtering.

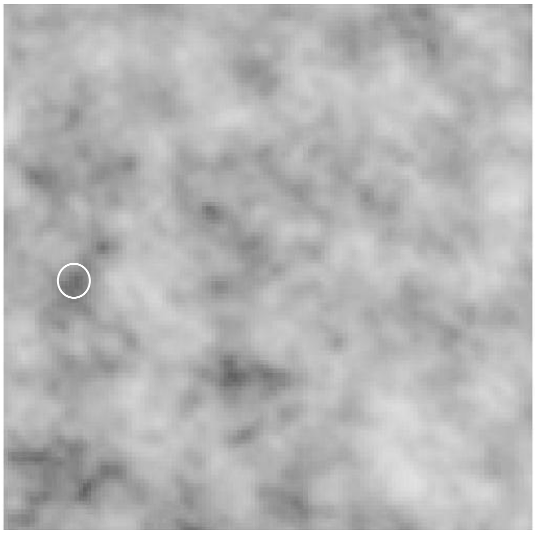

Figure 4.14 Identification of False Positive.

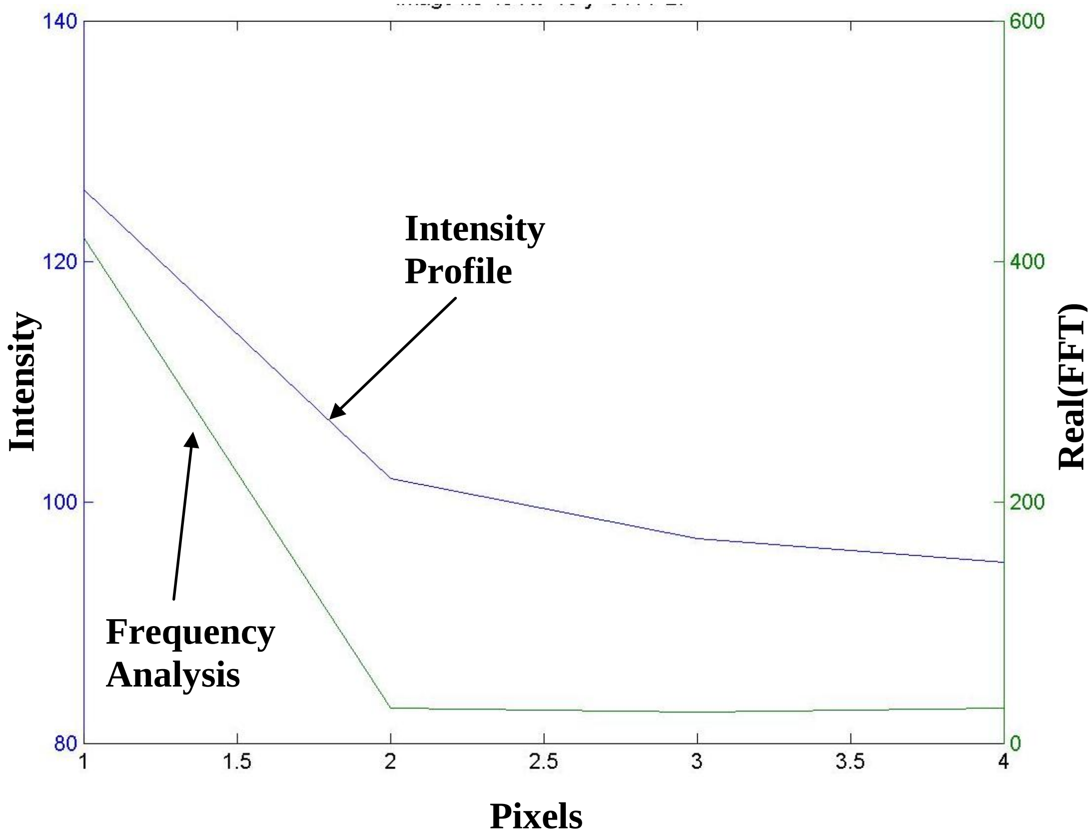

Figure 4.15 Interference Fringe Profile Frequency Analysis of False Positive.

To summarize, the FFT threshold is a filtering approach to remove false positive drops in near field holographic spray analysis. As real drops exhibit a fringe pattern within their edges and false positives do not, a Fourier Transform can appropriately determine if a dominate frequency exists within the detected drop. It stands to reason that if a dominant frequency does exist, it is caused by the internal fringe pattern. A user defined threshold of the FFT is set to determine if a frequency dominates the space. If not, the identified location is removed. In tests, over 150 droplet images have been correctly analyzed.

Clearly one of the potential drawbacks of this approach is that the smallest droplets will produce a small sample size of pixel intensities for the FFT. This results in aliasing in the frequency space. But, it has been found that the false droplet frequency response is somewhat linear. Furthermore, these very small drops may already be ignored because of the poor spatial accuracy of such a small measurement. So, the FFT filter may remove some true drops due to aliasing but all false positives should be removed. These problems are also mitigated because they will only have their greatest impact on the smallest droplets. Finally, the aliasing impact is further reduced as the fringe pattern changes with the span wise location; a dominant frequency of an out of focus drop may still be identified in a neighboring analysis.

4.6 Velocimetry

Individual velocity vectors for each droplet are calculated from the total distance traveled for each droplet. The individual distances are measured from the droplet centroids. The time delay is set by the pulse delay between lasers. It is measured by a photo-detector and oscilloscope. Particle tracking velocimetry (PTV) is used to pair droplet images. Specifically, the approach is based on the methods described in Grant and Thompson (1999). A pair of reconstructed images have been overlaid to demonstrate PTV; see Figure 4.16. An initial velocity vector approximation must be provided to each droplet. In the current program, knowledge of the general flow field at each hologram location is used; see the black arrows in Figure 4.16.

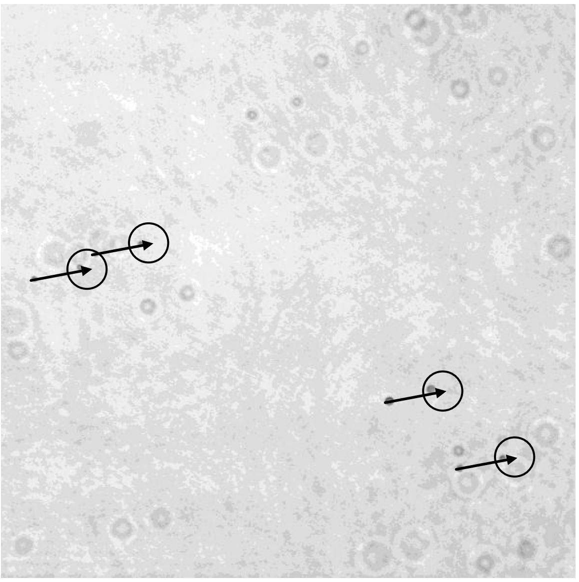

Figure 4.16 Particle Tracking Velocimetry.

The steps for calculating velocity vectors are:

1. For each droplet in the first pulse, calculate where it *should* move in the second hologram according to the guessed velocity vector (Grant and Thompson, 1999).

2. Define a search area around the predicted location. As the stream wise and vertical components dominate the velocity calculation, a spherical search area is not used. Currently, a circle with a diameter equal to half the distance traveled is used within the plane of the slice. A span of five reconstructed slices is searched in the direction normal to the camera. The size of the search area must be increased as the uncertainty in the initial vector increases (Grant and Thompson, 1999).

3. The droplet in the second hologram that is closest to the predicted location and is within the search area is identified as the image pair. If there are no droplets within the search area, the first droplet is removed from the detected drops list. On the other hand, if multiple possibilities are found, the droplet closest in size to the first droplet is identified as the match.(Grant and Thompson, 1999)

4. Finally, the 3D distance for each paired droplet is recalculated and the velocity vector is found. Three lists are compiled, lists of unmatched drops from each hologram and a list of matched drops with velocities. (Grant and Thompson, 1999)

Some preliminary results for PTV are given in Figure 4.17. In it, the downstream velocity (u, m/s) at one test location is plotted against the downstream location. The wind tunnel velocity is 103 m/s, faster than any of the drops. Hence, the expected trends are found in Figure 4.17. The smallest drops are being accelerated the fastest because of their low momentum. The largest drops are the most resistant, with the 40-50 and 50-60 micron bands showing nearly the same velocity and acceleration across the test volume.

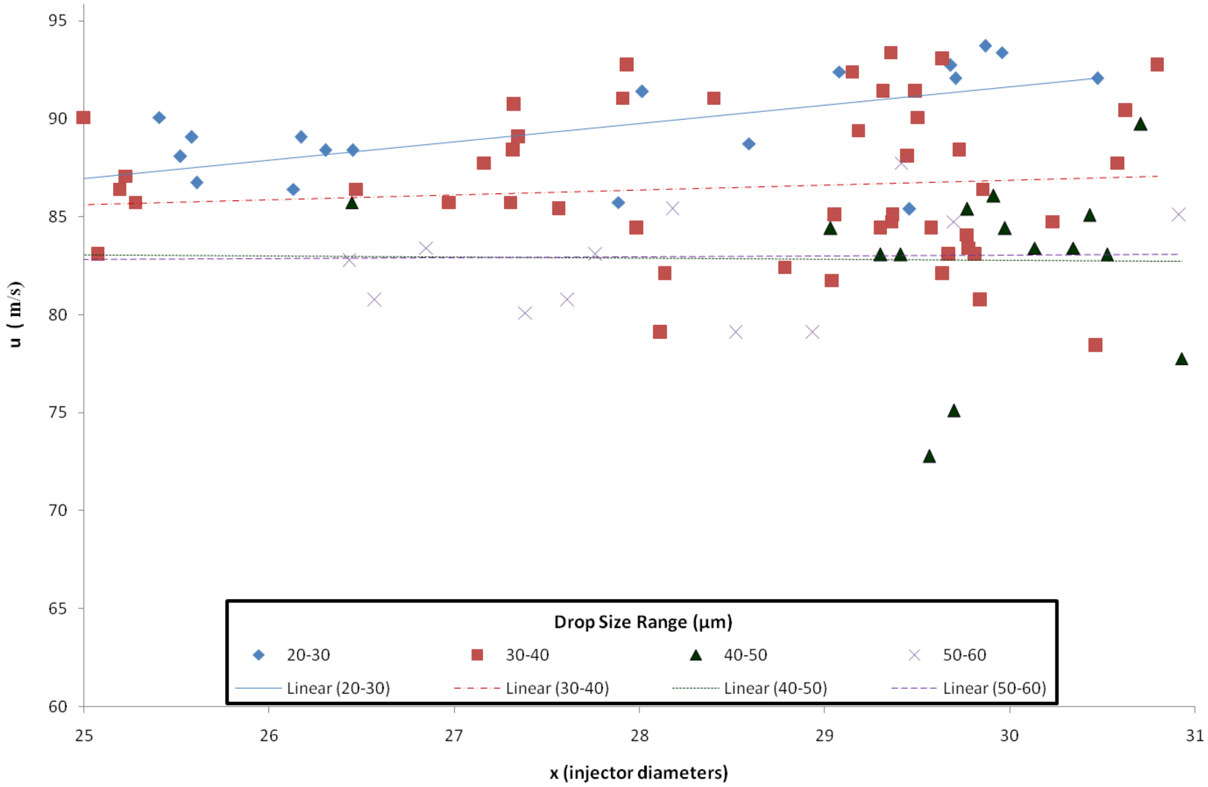

Figure 4.17 Streamwise Velocity vs. Downstream Location for Varying Drop Sizes (M = .3, GLR = 8%).

4.7 Considerations for Reduced Processing Time for High Drop Number Density Images

When applied to sprays with approximately a hundred drops, the previously discussed methods are effective at conditioning reconstructed images, detecting drops, measuring their 3D distribution and size, checking for false positives, and calculating velocity. Unfortunately when they are combined into one algorithm and applied to a near field hologram containing thousands of drops, the program run time increases exponentially and it becomes impractical to run the full image analysis suite (over one million FFT calculations could be required alone!). Some of these routines are also not as easily vectorizable. Considering the much larger sample size available, allowances on each individual measurement can be made to improve the overall run time. Restated, if the uncertainty on individual drop measurements isn't as important the overall uncertainty of a collection of measurements, a Central Limit Theorem argument can be made to justify run time compromises.

So for lower number densities, the very methodical approaches already described are useful. For cases involving higher numbers of drops, or when a large volume of holograms needs to be processed (i.e. when building correlations containing many variables), a modified program is used instead. The FFT threshold and finding the approximate location from the largest drop image are removed.

4.7.1 Two Step Centroid Calculation for Drop Span wise Location

So instead, the knowledge that the largest cross-section is approximately the focused location is used by implementing a span wise centroid calculation similar to that of Sheng, et al. (2006). But as already been shown, the centroid calculation of these drops is sensitive to the range of the images used; see Figure 4.3. To compensate for this, a two stage approach is employed. First, a centroid calculation is run using a “coarse” reconstruction interval. This will define a 3D ROI that will contain the actual drop. The maximum reconstruction spacing must be small enough to detect the existing fine fluid structures (such as satellite droplets and ligaments).

The second phase is to rerun the z centroid calculation only on a span centered on the approximate location of the drop, as defined in the first phase. A smaller reconstruction step can be used to improve span wise accuracy and capture the true size of the drop. The span corresponds with the approximate visual depth of focus of the drop. This is typically 10 reconstructed mm. By vectorizing this two phase approach, much faster run times are achieved.

In each slice, droplets must be detected before running the centroid calculation. For the two phase approach for near field sprays, it has been found that Canny edge detection works better than the previously stated Robert's edge detection. This is because in the near field, surrounding fringe noise is nearly as dark as a real droplet. As the surrounding noise coalesces, it begins to look like a droplet. These problems are amplified when two drops overlap (recall that in transmission holography, the camera cannot measure a drop if it is masked by another drop). These problems are countered first by insuring that an identified drop has a depth of focus. Canny edge detection is effective because a feint edge will only be detected if it connects to a sharp edge. By using very restrictive thresholds, the slightly blurred edges caused by nearby noise forces an entire detected drop to be ignored. Restated, only drop images with very sharp edges are kept for the centroid calculation. Using statistics terminology, Type II error is traded to decrease Type I error. From a PIV view, each image is sampled to find pixels that belong to a drop. By imposing strict standards for detection, it will be required to analyze additional holograms to achieve the same level of statistical confidence.

A fundamental assumption is that the there is no direct correlation between the size of a drop and whether it is wrongly ignored (using the Pearson product-moment correlation coefficient). Most importantly, if there is no direct relation for the ignored drop size, correlations of droplet velocity and size can be calculated (with a lower confidence given the lower sample size). These statistics are discussed in more detail in the Section 4.7.2. A number density calculation will need a correction term to account for the Type I error.

4.7.2 Adjustment of Program Drop Parameter Results for Misclassification Errors

The computer program generates a dataset of individual detected drops with characteristics and parameters. The dataset of detected drops is regressed to a probability density function (pdf) of individual drop parameters (*d*) across the range of values, i.

$$p(d_i)\ for\ \ i = \{\text{min parameter value} \ldots \text{max parameter value}\} \in \text{dataset}$$

$$\text{where } \int p(d_i)dx = 1 \tag{4.1}$$

Each drop parameter (e.g. diameter, velocity, etc.) has its own pdf so that correlations are independent of one another. Each interval within a density distribution, p, is given a subscript (discritized by i) as they are not necessarily "exchangeable" with other values of d in following calculations. For example, if drop velocity is the current parameter (d), $p(d)$ is the velocity probability density distribution regressed from the algorithm results. This is developed from $p(d_i)$, the percentage of drops with velocity i .

The regression, $p(d_i)$, will have uncertainty based on the dataset. The Type I and Type II errors (categorical errors) inherent to the program that generated the dataset are not explicitly included in the data's regression (which has its own uncertainty band with errors). The final reported distribution for the spray properties should consider all available sources of error. The following addresses the impact that an uneven distribution of Type I and Type II errors inherent to the program would have on the final, reported, drop parameter distribution.

There are four classifications for drop detection:

- True Positive (TP): the ideal state in which a real drop in the image space is correctly identified as being a drop.
- False Positive (FP): noise in the image is incorrectly identified as a drop by the algorithm. This is akin to Type I error (aka α error).
- True Negative (TN): noise in the image is correctly ignored. No record of this is maintained in the final dataset.
- False Negative (FN): a real drop in the image space is incorrectly treated as noise and is dropped from the dataset. This is akin to Type II error (aka β error).

By definition, any entry in the final dataset is either true positive or false positive. Therefore, the "ideal" regression of the dataset (i.e. the true droplet population with no contaminated data) for the parameter distribution of detected drops would be

$$p(d_i|nFP_i, nFN_i) \tag{4.2}$$

Hence, it is the real distribution of drops in the hologram where no individual drop is identified as a false positive (*nFP*) and no individual drop is identified as a false negative (*nFN*). This meets the ideal requirement that there would be no Type I or Type II errors in sampling the population.

Bayes Theorem (Denison et al., 2002) can be used to expand this conditional probability into a joint likelihood containing the error types and the prior distribution of the drop parameter (regressed function).

$$p(d_i|nFP_i, nFN_i) = \frac{p(nFP_i, nFN_i|d_i)p(d_i)}{p(nFP, nFN)} \tag{4.3}$$

The denominator is a normalizing term equal to the sum of all possible hypotheses.

$$p(nFP, nFN) = p(nFP_i, nFN_i|d_i)p(d_i) + \sum_j \{p(nFP_j, nFN_j|d_j)p(d_j)\} \tag{4.4}$$

$$\text{for } j = \{\text{min parameter value} \ldots \text{max parameter values}\} \in \text{dataset}, j \neq i$$

i is the term of interest from the current drop parameter and j consists of all other possibilities within the parameter. Substitute the normalizing function and (assuming independent terms) break out the joint probabilities:

$$p(d_i|nFP_i, nFN_i) = \frac{p(nFP_i|d_i)p(nFN_i|d_i)p(d_i)}{p(nFP_i|d_i)p(nFN_i|d_i)p(d_i) + \sum_j \{p(nFP_j|d_j)p(nFN_j|d_j)p(d_j)\}}$$

where by definition:

$$p(nFP_i|d_i) = 1 - p(FP_i|d_i) \tag{4.5}$$

which is (number of detected drops – number of false pos.)/(number of detected drops). Recall that by being true positive or false positive, it is never true negative or false negative.

Likewise:

$$\begin{aligned} p(nFN_i|d_i) &= 1 - p(FN_i|d_i) \\ p\left(nFP_j|d_j\right) &= 1 - p\left(FP_j|d_j\right) \\ p\left(nFN_j|d_j\right) &= 1 - p\left(FN_j|d_j\right) \end{aligned} \tag{4.6}$$

Characteristic distributions can be regressed for these algorithm false positive rates and the false negative rates. Keeping the priors and substituting the likelihood terms yield:

$$p(d_i|nFP_i, nFN_i) = \tag{4.7}$$

$$\frac{[1 - p(FP_i|d_i)][1 - p(FN_i|d_i)]p(d_i)}{[1 - p(FP_i|d_i)][1 - p(FN_i|d_i)]p(d_i) + \sum_j\left\{\left[1 - p\left(FP_j|d_j\right)\right]\left[1 - p\left(FN_j|d_j\right)\right]p(d_j)\right\}}$$

Eqn. 4.7 is the primary equation which accounts for the algorithm’s Type I and Type II error distributions. It incorporates known program error rate distributions to the regressed data. The error rate priors would have to be measured from representative drop images. Doing so would allow the experimenter to adjust for Contaminated Data.

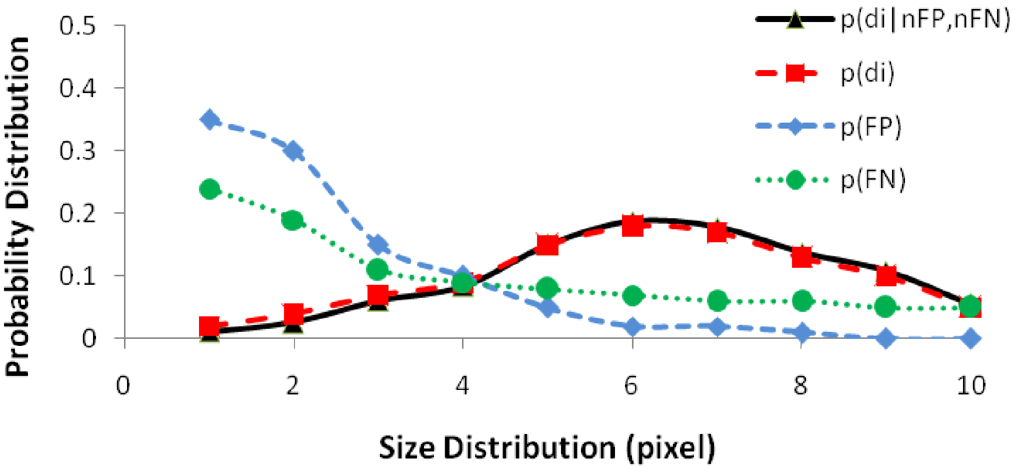

Figure 4.18 Notional Effect of Program Error (Type I and II) Distribution on Posterior Distribution of Drop Size.

Figure 4.18 gives example prior distributions for the drop size and associated Type I and Type II program error. The impact of these errors on the drop size posterior distribution is calculated and shown. Note that even the comparatively high error rates applied to the low drop number density tail of the size distribution only have a minor impact on the posterior distribution.

If it can be approximated that the Type I and Type II errors are statistically independent of the drop parameter distribution, then the false positive distribution is a constant (FP) for the parameter distribution. And, the false negative distribution is a constant (FN) for the parameter distribution. Therefore:

$$p(d_i|nFP, nFN) = \qquad (4.8)$$

$$\frac{[1-p(FP)][1-p(FN)]p(d_i)}{[1-p(FP)][1-p(FN)]p(d_i) + \sum_j\{[1-p(FP)][1-p(FN)]p(d_j)\}}$$

and $p(d_i) + \sum_j\{p(d_j)\}$ is equivalent to the cumulative distribution function of d taken over the entire domain; it sums to one. Therefore, Eqn. 4.8 simplifies to the original pdf from the dataset:

$$p(d_i|nFP_i, nFN_i) = p(d_i) \quad (4.9)$$

If it can be assumed that the program's Type I and Type II error distributions are constant for all possible values of a parameter, then it matches the intuitive case of frequentist statistics to assume that the data's regression is not skewed. Note that the program's overall error rates may still inflate the overall confidence interval of the final regression.

To show that $p(FP|d_i) \neq f(d_i)$ and that $p(FN|d_i) \neq f(d_i)$:

1. Make a subjective comparison by plotting the false positive and false negative rates vs. the drop distribution.

2. Calculate the reliability, r, of the errors to show that the variability of the program errors do not skew the regression.

   $$r = 1 - \frac{\sigma^2_{error\ data}}{\sigma^2_{observed\ data}} \quad (4.10)$$

   Ideally, r = 1 to show the variance of the error data has no effect on the overall dataset.

3. Calculate the correlation coefficient between the error classification and the drop parameter. A Pearson (or Matthew's Correlation for binary data, Baldi et al., 2000) coefficient will equal zero for no linear correlation.

Hence for a regression, the mean, μ, of the algorithm's output will be calculated using standard fitting techniques (i.e. least squares). Its confidence region must incorporate both the regression uncertainty (assumes data is all true positive) and the algorithm false positives.

A typical regression confidence interval is defined by

$$p_r(u < \mu < v) = (1-\alpha)_r \quad (4.11)$$

$(1-\alpha)_r$ is the confidence level for the probability that given lower and upper bounds, u and v, encompass the mean. Eqn. 4.11 is based solely on the data set. The confidence interval for the regression which incorporates the algorithm's true positive rate (TP) is given in Eqn. 4.12. The new confidence interval γ is a joint pdf:

$$\gamma = p(u < \mu < v, TP) \quad (4.12)$$

Assuming independent terms, Eqn. 4.12 can be split according to Eqn. 4.13.

$$\gamma \equiv p(u < \mu < v, TP) = p(u < \mu < v) \cdot p(TP) \quad (4.13)$$

If the true positive rate is constant for all cases, *p(TP) = TP*. Therefore, combining with Eqn. 4.11 yields

$$\gamma = (1-\alpha)_r \cdot TP \quad (4.14)$$

So the final confidence interval is a function of the normally calculated uncertainty region, with a confidence reduced by the true positive rate. The ideal behavior with no reduction is preserved.

4.7.3 Reduction of Search Volume to Decrease Run Times

In the far field, there is relatively little distortion so drops are clearly visible across most of the sample volume. Therefore, it was attempted to use a first phase search interval up to half an order of magnitude larger than that used in Section 4.7.1. Unfortunately, once this coarse interval is larger than a few droplet equivalent diameters, there is not enough information to calculate the centroid accurately.

Reducing the hologram investigation size was also tried to improve processing time and find an optimum that would give the highest analyzed area / run time. Unfortunately, no optimum exists. For example, a 2048 x 2048 pixel^2 hologram provides full coverage at a test location. So, a 1624 x 1624 pixel^2 hologram will cover 63% of the area, but still took 61% of the time to run. Multiple runs of different sizes confirmed there the area / time ratio was constant within a few percentage points. The algorithm is intentionally setup to be parallelized; the run sequences of most algorithm loops are independent of the loops' step number. As such, the analyzed area/run time is essentially linear. After accounting for the extra program book keeping and error checking, looping the subroutines on subsets of holograms is not worthwhile.

4.8 Code Validation

The algorithm, as described in Section 4.7.1, is used to study near field sprays.

4.8.1 Independence of Classification Errors from Drop Size

Samples of 3713 near field droplets were taken to characterize the error in the program and calculate an uncertainty for future results. 3063 drops were detected across the entire size distribution, of which 193 were false positives; see Figure 4.19.

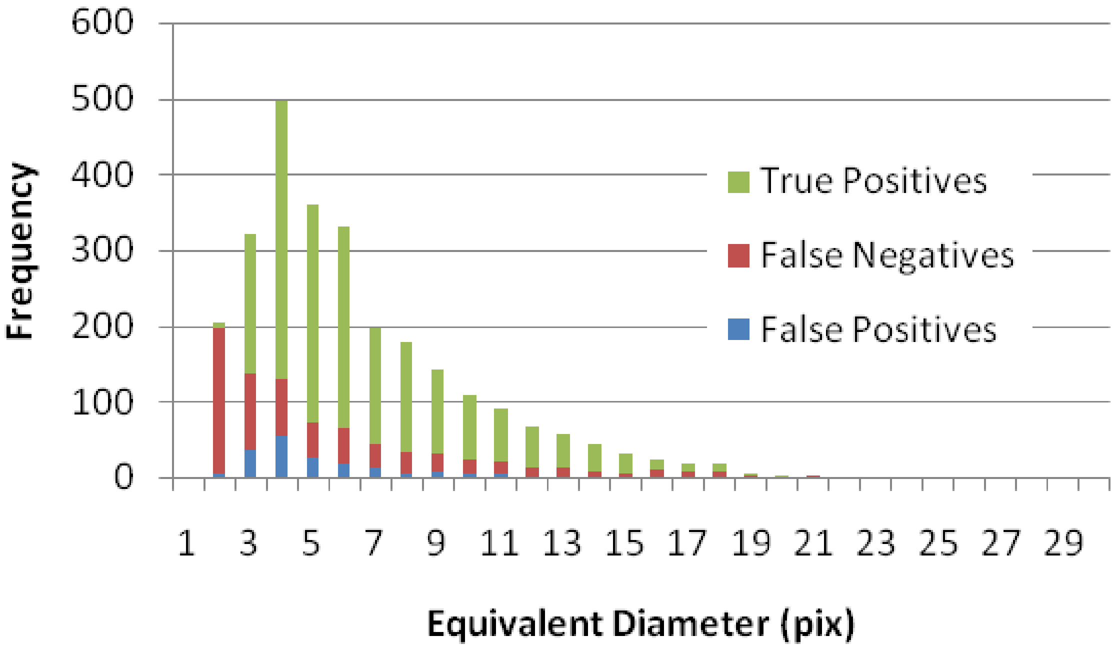

Figure 4.19 Raw Distributions of Droplet Sizes for Sample Images.

The true positive, false negative, and false positive distributions are given as a function of droplet size in Figure 4.19. Clearly, drops with an equivalent diameter less than four pixels have a high classification error rate. If the results that are less than a diameter of six pixels are removed from the data set, the error rates improve significantly. 1005 drops remain with 766 true positives, 192 false negatives, and 47 false positives.

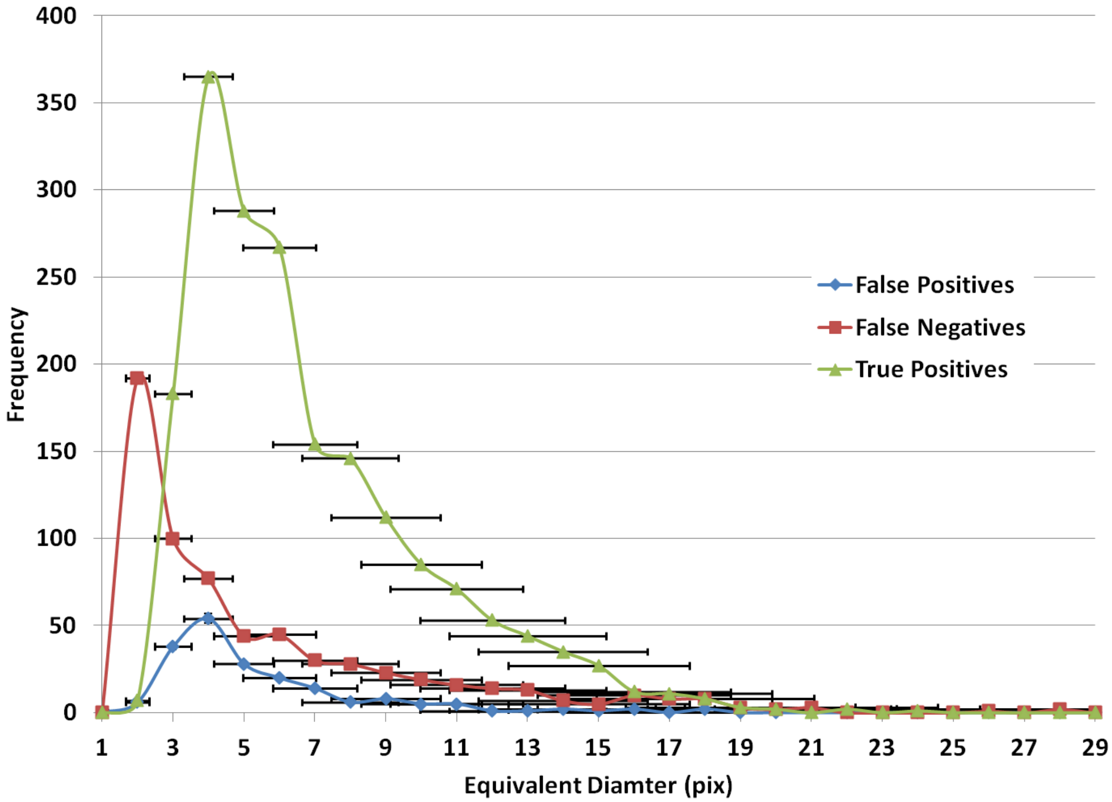

Figure 4.20 Frequency Distribution of Classification Categories, +/-17% Diameter Uncertainty.

Of the 958 droplets remaining in the sample, 766 were correctly detected, giving a “false negative” rate (A.K.A. Type II Error or beta error) of 20%. But, there is not a direct correlation between whether a drop is missed and its equivalent diameter (Pearson correlation coefficient = 0.1759). Therefore a single correction factor (based on the image properties but not the drop size distribution) could be used to correlate number density and drop distribution calculations.

Hence, the Type II (AKA beta error) is independent of size, for the minimum size threshold imposed. In addition to the 766 true positives, the 47 false positives provide a Type I (aka alpha error) error rate of 6.1%. This too can be assumed to be independent of drop size (Pearson correlation = -0.0366). Likewise, the true positive rate is independent of drops size (correlation = -0.1443). Note this type of analysis would need to be repeated for drastically different hologram images. This figure reinforces the need for high magnification in microscopy. If the bulk of the fluid is above the cut off, the detection rates would improve dramatically. This is a function of the experimental setup, not the algorithm.

The reliability of a subsample can also be used to measure the impact of its variability on the entire sample's characteristics:

$$r = 1 - \frac{\sigma^2_{error\ data}}{\sigma^2_{observed\ data}} \tag{4.15}$$

So, the reliability is a measure of variance. For the given threshold, the false positive and true positive reliability is 0.99 and 0.97, respectively. From Fig. 4.20, it is assumed that uncertainties in the diameter measurement are not skewing the results given the large sample size. Particularly, it is assumed that the uncertainties associated with equivalent diameters near the six pixel threshold are not skewing the results.

In summary, the algorithm trades the overall detection rate to ensure that the drops that are detected are correct. Furthermore, field properties (volume averaged velocity, SMD, etc.) are treated just like any other data set, a correction factor is not required. The sample size is smaller than what might otherwise be possible, but given the low Type I error, analyzing additional holograms will raise the available number of drops and likewise increase the confidence level of any calculations. The impact of the size threshold on the total volume of drops is shown in Figure 4.21.

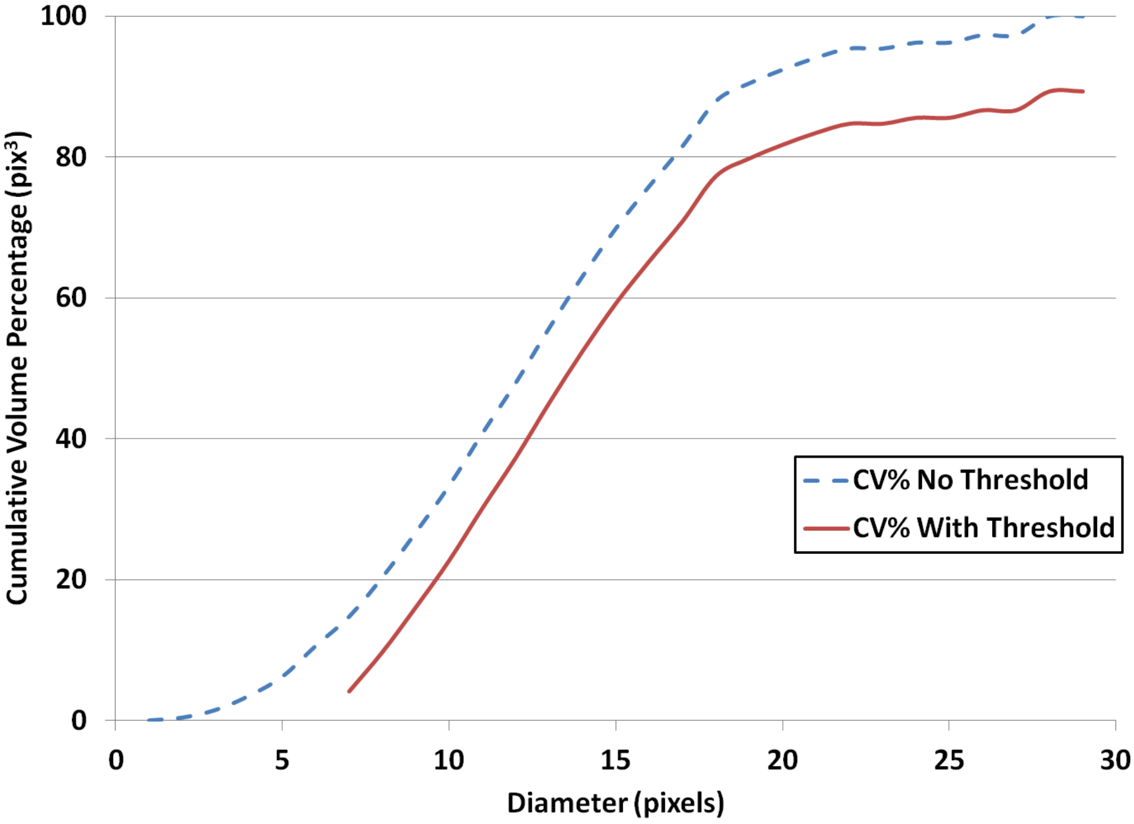

Figure 4.21 Cumulative Volume Percentage of Drop Size Distribution.

By making the allowances discussed in the previous sections for very high number density sprays, an order of magnitude more holograms can be processed in the same computer processing time. Therefore, the increased uncertainty incurred by simplifying the analysis of any one hologram is more than compensated by the increased sample size available through the extra hologram results.

4.8.2 Effect of Increasing Reconstruction Interval

Given the advances made in Section 4.7.1, it is tempting to further reduce processing time by increasing the reconstruction interval (distance between slices). Reducing the number of reconstructions has the greatest impact on the total run time. During algorithm development, a reconstruction interval of approximately a quarter diameter of the smallest drops ensured that several reconstructions passed through every true drop. By increasing the reconstruction interval, one risks:

a) that no image is close enough to the true center to capture a drop's true size
b) that the reduced number of locations in the centroid calculation will shift the span wise coordinate
c) that if the droplet span wise centroid is too far from any reconstructions, the (x,y) centroid will shift
d) that droplets will be missed in the initial pass through

Fortunately, the actual changes in results show that most of these concerns are overstated (note that this may not be true for very high expansion holographic microscopy). By increasing the reconstruction interval to approximately 5 droplet diameters:

a) the measured equivalent diameters changed by less than one pixel
b) the span wise coordinate did change by several droplet diameters, but less than the 5 droplet diameter increase in reconstruction interval
c) the span wise centroid shifted by less than one pixel in the x and y directions
d) Of the ~3000 droplets detected, the total number of detected drops only changed by 10 drops

The one pixel changes in the (x,y) centroid and the diameter are minor increases in uncertainty given the increased samples. When regressed, these differences are undetectable. Therefore, the primary impact of reducing the number of reconstructions is to significantly increase the span wise centroid uncertainty. The differences will also be suppressed when calculating the volume averaged properties as it is the smallest drops that are most sensitive to the additional errors.

4.9 Comparison of Results

The results of the near injector, dense spray are presented here along with their supporting statistics. The algorithm, as described in Section 4.7.1, was used.

4.9.1 Comparison of Results to Other Research in the Far Field

The algorithm is validated against the results of another research group using established methods. Lin et al. (2002) provide several results for aerated liquid jets in the far field using PDPA. Several of these researchers also worked to collect the Applied Sprays (Section 3.4) data on a similar wind tunnel and water injection system. Therefore, Lin et al. (2002) is a good benchmark on which to compare the current algorithm's results. Table 4.1 lists the common test conditions between this holography study and Lin et al. (2002). The cross flow Mach number (M), downstream distance from the injector (x, normalized by the injector diameter, d), momentum flux ratio (q), Gas/Liquid Ratio (GLR, mass percentage), and detected Sauter Mean Diameter (SMD, microns) are given. Note, one finding of Lin et al. (2002) is that q does not have a statistically significant effect on SMD. Hence, the SMD of the studies may be compared while the other properties describing the plume size may not be compared.

Table 4.1. Comparison of Algorithm's Results (Holo.) to Lin et al., 2002 (PDPA).

	PDPA	Holo	PDPA	Holo	PDPA	Holo	PDPA	Holo	PDPA	Holo	PDPA	Holo	PDPA	Holo
M	0.3		0.3		0.3		0.3		0.3		0.3		0.3	
x/d	50		100		50		100		50		100		100	
q	6	10	6	10	6	10	6	10	6	10	12	10	12	10
GLR	0		0		4		4		8		0		4	
SMD	43.3	47.1	46.6	50.4	36.1	34.6	36.4	38.3	29.5	31.9	45.5	50.4	35.2	38.3

As will be discussed Section 4.10, the uncertainty of the SMD holography measurements is +/- 26% (calculated from Eqn. 4.27). In comparison, Lee (2009) used a less conservative calculation for uncertainty and reported an SMD percentage for similar holograms of aerated liquid jets of 21.5%. The tabulated results show a difference of less than five microns (10%) in SMD across test conditions. The uncertainty is this high because of the small number of pixels per drop. Using either a higher pixel density CCD or greater magnification will significantly reduce the final uncertainty.

4.9.2 Comparison of Results to Other Research in the Near Field

Some of the original holograms used in the 0.5 mm injector manual analysis in Miller et al. (2008) were available for processing by the algorithm. These results are compared in Table 4.2. This table gives results for Sauter Mean Diameter (SMD, μm), Mass Median Diameter (MMD, μm), and their ratio (MMD/SMD) at different test combinations of downstream location (x/d, number of injector diameters), mass momentum ratio (q), and Gas/Liquid Ratio (GLR, %).

Table 4.2. Comparison of Algorithm's Results to Manual Results in Miller et al. (2008).

	Alg.	Miller	Alg.	Miller	Alg.	Miller	Alg.	Miller	Alg.	Miller	Alg.	Miller	Alg.	Miller	Alg.	Miller
x/d	25		50		25		50		25		50		25		50	
q	.74		.74		.74		.74		4.0		4.0		4.0		4.0	
GLR	4		4		8		8		4		4		8		8	
SMD	166	154	81	97	88	75	69	62	152	167	170	149	81	74	78	70
MMD	189	176	85	115	100	81	74	66	186	193	227	191	91	83	87	80
MMD/SMD	1.1	1.1	1.1	1.2	1.1	1.1	1.1	1.1	1.2	1.1	1.3	1.3	1.1	1.1	1.1	1.1

Most of the manually developed results from Miller et al. (2008) fall well within the expected range of the algorithm's results. The one exception is the x/d=50, q=.74, GLR=4% test location. The variation between results is explained in Figure 4.21. It is a histogram of the detected droplet diameter distributions.

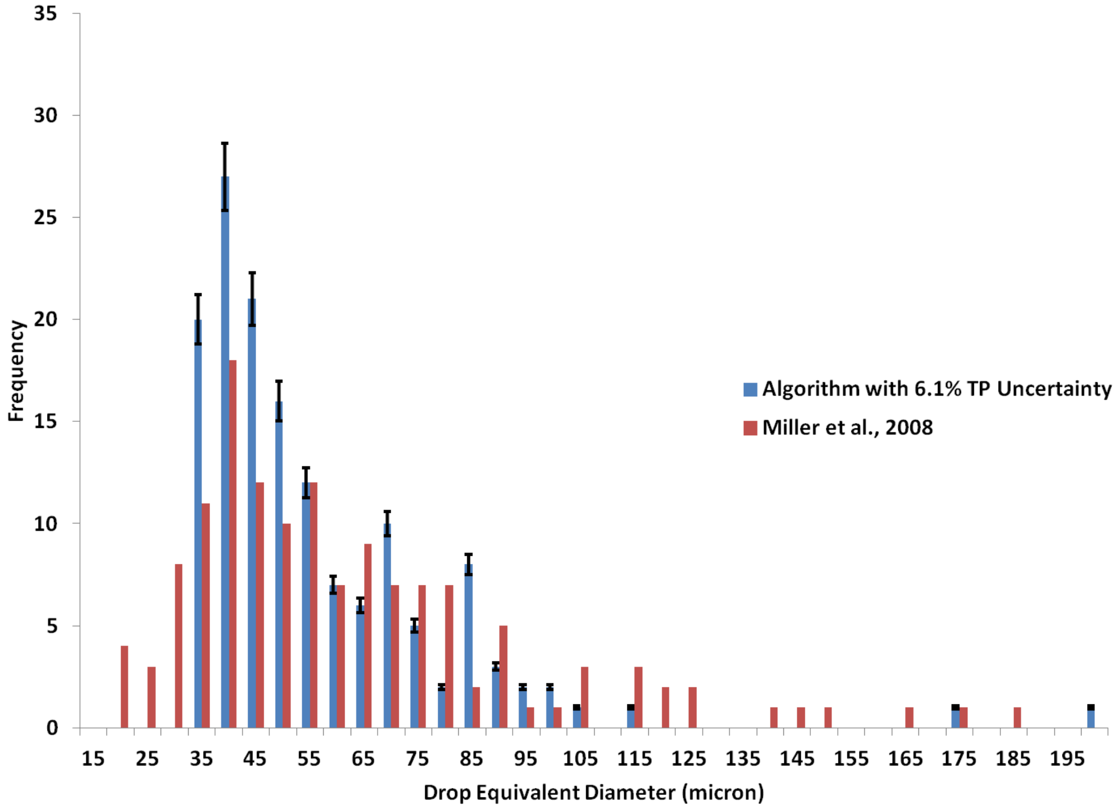

Figure 4.22 Comparisons of the Automated Near Field Spray Analysis with Miller et al., 2008 +/-6.1% Uncertainty Bars from Algorithm's True Positive Rate.

The algorithm has a minimum size threshold of 30 μm (akin to Figure 4.19). Also from Figure 4.22, it is found that the algorithm detected many more droplets in the 35-45 μm region. In addition to these additional drops the algorithm found, several larger drops measurements were undersized. Note that these measurements were still within the program's size uncertainty. Even though these factors combined to produce a size distribution to the left of Miller's, Miller's final results were still within the propagated uncertainty of the algorithm. The development of the uncertainty equations is discussed in Section 4.10.

4.10 Uncertainty Analysis for Near Field Spray Measurements

The uncertainty, ε, of all the droplet properties ultimately depends on just a few parameters, namely their measured size and location, and physical properties inherent to the experiment like fluid density and Mach Number. The uncertainties of the physical properties and wind tunnel equipment are provided in Chapter III.

There are two methods for quantifying the uncertainty of the droplet size and the spray field. The first is to cite the uncertainty of individual droplets. This uncertainty will usually be conservatively high, but is necessary if one wishes to characterize a system of individual measurements. The alternative approach is to quote uncertainties based upon a large sample size and its standard deviation. The standard deviation approach will require duplicate calculations of the field parameters.

4.10.1 Uncertainty of Droplets Size and Location Measurements

In order to calculate the standard deviation of an array of droplet sizes, the image acquisition and processing system must be characterized for a variety of different sized images. Obviously, real droplets cannot be used, even if multiply exposed on one image. The alternative is to use a standard target with a variety of known features. The current project uses the standard Air Force resolution target (MIL-STD-150) for its widespread usage, low cost, and accepted standard in providing a variety of sizes to analyze. It allows the calculation of the uncertainty as a function of size. Following Taylor and Kuyatt (1994), the average value and the standard deviation of the feature size is used to calculate the uncertainty. The uncertainty, as a function of size, d, is calculated using Equation 4.16.

$$\varepsilon(d) = \pm t_{1-\alpha,n-1} \frac{\sigma}{\sqrt{n}} \tag{4.16}$$

Three sets of target bars each were taken from 25 holograms of Air Force Resolution Targets. The holograms were reconstructed at the focal plane so that measurements of the target bars could be compared to their true value and an uncertainty for the program could be calculated. The target's bars are found using the same edge detection algorithm used to find the droplets. The edge detection results (pixels) are converted to the equivalent size measurement (microns) so that the calculated uncertainty encompasses errors in the edge detection program as well as errors in the pin calibration (Figure 3.20). By Equation 4.16, the uncertainty for any one diameter measurement for the program is +/-17% with a 99% confidence level.

$$\varepsilon_{deq} / d_{eq} = \pm 17\% \tag{4.17}$$

Location measurements within an image slice are a simple centroid calculation; they are on the order of individual microns. Hence, it is assumed that the vertical and stream wise coordinates are negligible when combined with the global location uncertainties inherent in the CCD location. Since there is no orthogonal view to verify span wise measurements, the span wise coordinate uncertainty is found in a similar manner to the size uncertainty. The same MIL-STD-150 Air Force resolution target is analyzed at several elements and across many reconstructions and the resultant span wise centroid is compared to the known location. By relating the results of the AF target analysis and analysis of drops along a target (see Figure 3.1) back to real, global coordinates, the uncertainty of the pin calibration (Figure 3.20) is incorporated into the standard deviation in Eqn. 4.16. By Eqn. 4.18, the uncertainty for any one span wise coordinate measurement of the program is +/- 2.97 drop diameters with a 90% confidence level.

$$\varepsilon_z / d_{eq} = \pm 2.97 \tag{4.18}$$

4.10.2 Uncertainty Propagation

These uncertainties propagate through all subsequent calculations. Assuming the predictor variables are independent and following Kline (1985), the equation for the non-dimensional propagation of uncertainty percentage is:

$$\frac{dZ}{Z} = \sqrt{\left(\frac{\partial \ln Z}{\partial \ln X_1}\frac{\varepsilon_{X_1}}{X_1}\right)^2 + \left(\frac{\partial \ln Z}{\partial \ln X_2}\frac{dX_2}{X_2}\right)^2 + \cdots + \left(\frac{\partial \ln Z}{\partial \ln X_N}\frac{dX_N}{X_N}\right)^2} \tag{4.19}$$

which is recast into the more usable form

$$\frac{\varepsilon_Z}{Z} = \sqrt{\left(\frac{X_1}{Z}\frac{\partial Z}{\partial X_1}\frac{\varepsilon_{X_1}}{X_1}\right)^2 + \left(\frac{X_2}{Z}\frac{\partial Z}{\partial X_2}\frac{\varepsilon_{X_2}}{X_2}\right)^2 + \cdots + \left(\frac{X_N}{Z}\frac{\partial Z}{\partial X_N}\frac{\varepsilon_{X_N}}{X_N}\right)^2} \tag{4.20}$$

where $\frac{\varepsilon_Z}{Z}$ is the uncertainty percentage of the calculated parameter under consideration (Z). $\frac{X_i}{Z}\frac{\partial Z}{\partial X_i}$ are the individual influence coefficients and $\frac{\varepsilon_{X_i}}{X_i}$ are the uncertainty percentages for each contributing term. For all the current measurements, every parameter's uncertainty is centered on zero. ε_X is the absolute uncertainty of X. As it will be desired to limit the experiment's physical parameters based upon maximum percentages, the alternate, dimensional form, of Kline's uncertainty equations are not used.

4.10.3 Equivalent Diameter (Calculated From the Cross-Section Area)

If the measurement error of the area is known, the equivalent diameter can be calculated from the cross-sectional area measurement. In this sense, the equivalent diameter is

$$d_{eq} = \left(\frac{4A}{\pi} \right)^{1/2} \tag{4.21}$$

The percent uncertainty of the equivalent diameter is:

$$\frac{\varepsilon_{d_{eq}}}{d_{eq}} = \sqrt{\left(\frac{A}{d_{eq}} \frac{1}{\sqrt{\pi A}} \frac{\varepsilon_A}{A} \right)^2} \tag{4.22}$$

4.10.4 Sauter Mean Diameter

From Eqn. 1.1, when all of the individual droplets are known for a region of space (i = 1..n) and the dispersed phase is constant density, the equation for that interval's Sauter mean diameter (SMD) is:

$$SMD = \frac{\sum d_{eq}{}^3}{\sum d_{eq}{}^2} \tag{4.23}$$

where d_{eq} is the equivalent diameter of each individual droplet. The SMD uncertainty can be found from multiple samples of the SMD and Eqn. 4.16 or by calculating the propagation of error per Eqn. 4.20. Here, it is calculated through the propagation of uncertainty using Eqn. 4.20. Eqn. 4.24 and Eqn. 4.20 are combined into the following form.

$$\frac{\varepsilon_{SMD}}{SMD} = \sqrt{\sum_i \left(\frac{d_{eq,i}}{SMD} \, {}^{\partial SMD}\!\big/_{\partial d_{eq,i}} \, \frac{\varepsilon_{d_{eq,i}}}{d_{eq,i}} \right)^2} \tag{4.24}$$

i denotes any individual droplet. $d_{eq,i}$ must be isolated in order to calculate the influence coefficient each droplet has on the SMD. The percent uncertainty of each equivalent diameter is given by Eqn. 4.17. The $d_{eq,i}$ terms could be canceled if the absolute uncertainty of $d_{eq,i}$ is known instead.

The derivative of the SMD with respect to each droplet is calculated in Eqn. 4.25.

$$\partial SMD \big/ \partial d_{eq,i} = \frac{3d_{eq,i}{}^{2}\left(d_{eq,i}{}^{2} + \sum_{j} d_{eq,j}{}^{2}\right) - 2d_{eq,i}\left(d_{eq,i}{}^{3} + \sum_{j} d_{eq,j}{}^{3}\right)}{\left(d_{eq,i}{}^{2} + \sum_{j} d_{eq,j}{}^{2}\right)^{2}} \tag{4.25}$$

where

$$\sum_{all\,drops} d_{eq} = d_{eq,i} + \sum_{j} d_{eq,j}\,, \;\; j \neq i \tag{4.26}$$

The uncertainty of SMD can then be reduced to

$$\frac{\varepsilon_{SMD}}{SMD} = \sqrt{\sum_{i}\left\{\frac{d_{eq,i}\left(3d_{eq,i}{}^{2} - 2d_{eq,i}\,SMD\right)}{d_{eq,i}{}^{3} + \sum_{j} d_{eq,j}{}^{3}}\frac{\varepsilon_{d_{eq,i}}}{d_{eq,i}}\right\}^{2}} \tag{4.27}$$

4.10.5 Velocity

The uncertainty percentage for the individual velocity is calculated in the same way. If u is representative of each of the components, the velocity is given by Eqn. 4.28.

$$u = \frac{\Delta x_{c}}{\Delta t} = \frac{x_{c2} - x_{c1}}{\Delta t} \tag{4.28}$$

The vector is measured from the centroids of the droplets. By substituting the velocity into Z, Eqn. 4.20 becomes:

$$\frac{\varepsilon_u}{u} = \sqrt{\left(\frac{x_{c2}}{u}\,\frac{1}{\Delta t}\,\frac{\varepsilon_{x_{c2}}}{x_{c2}}\right)^2 + \left(\frac{x_{c1}}{u}\,\frac{-1}{\Delta t}\,\frac{\varepsilon_{x_{c1}}}{x_{c1}}\right)^2 + \left(\frac{\Delta t}{u}\,\frac{-(x_{c2}-x_{c1})}{\Delta t^2}\,\frac{\varepsilon_{\Delta t}}{\Delta t}\right)^2} \tag{4.29}$$

and most likely, the centroid uncertainties will be equal.

The uncertainty in the time delay was left to point out that its influence coefficient can be significantly larger than those for the centroids. However, modern lasers have negligible shot-to-shot jitter and oscilloscopes can repeatedly measure on the order of nanoseconds. Furthermore, the time delay will be orders of magnitude greater than its uncertainty and the entire fraction will be squared. Hence, the contribution from time uncertainties is ignored. Therefore, the percent uncertainties of the velocity components are each:

$$\frac{\varepsilon_u}{u} = \frac{\pm 1}{u\,\Delta t}\,\frac{\varepsilon_x}{x_c}\sqrt{{x_{c2}}^2 + {x_{c1}}^2} \tag{4.30}$$

This leads to the interesting dilemma that longer time delays are desirable for decreasing the uncertainty in the velocity measurement. However, this must be balanced by the need for short time delays to increase the success rate of matching droplets. As always, Eqn. 4.28 requires a short enough interval to assume that the instantaneous velocity is calculated. By substituting u back in, the time contribution can be canceled from Eqn. 4.30:

$$\frac{\varepsilon_u}{u} = \frac{\varepsilon_x}{x_c}\,\frac{\sqrt{{x_{c2}}^2 + {x_{c1}}^2}}{\Delta x_c} \tag{4.31}$$

4.10.6 Acceleration

The acceleration of a droplet could be calculated in the same way as the velocity. If triple pulse holography were available, the acceleration would be calculated from the two velocity calculations. For example, the acceleration x-component is a function of the x-component velocity at two instants in time.

$$a_x = \frac{\Delta u}{\Delta t} = \frac{u_2 - u_1}{\Delta t} \tag{4.32}$$

The vector is measured from the centroids of the droplets. Again, the contribution from the time will be negligible and the uncertainty percentages associated with u are equal. Therefore, the percent uncertainties of the acceleration components are each:

$$\frac{\varepsilon_{a_x}}{a_x} = \frac{\sqrt{{u_2}^2 + {u_1}^2}}{\Delta u} \frac{\varepsilon_u}{u} \tag{4.33}$$

4.10.7 Mass Averaged Velocity

For identical density droplets, the equation for the mass averaged velocity is

$$\tilde{u} = \frac{\sum \left(u {d_{eq}}^3 \right)}{\sum {d_{eq}}^3} \tag{4.34}$$

Following the same approach and assumptions that were used for the SMD, the uncertainty for mass averaged velocity is:

$$\frac{\varepsilon_{\tilde{u}}}{\tilde{u}} = \sqrt{\sum_i \left\{ \frac{3 {d_{eq.i}}^3 \left(u_i - \tilde{u} \right)}{\tilde{u} \left(d_{eq,i} + \sum_j d_{eq,j} \right)} \frac{\varepsilon_{d_{eq.i}}}{d_{eq.i}} \right\}^2} \tag{4.35}$$

4.10.8 Momentum Flux Ratio

The equation for the momentum flux ratio is

$$q = \frac{\rho_L{}^2 v_j{}^2}{\rho_\infty{}^2 v_\infty{}^2} \tag{4.36}$$

The corresponding uncertainty propagation is

$$\frac{\varepsilon_q}{q} = \sqrt{\begin{array}{l}\left(\frac{\rho_L}{q}\frac{\partial q}{\partial \rho_L}\frac{\varepsilon_{\rho_L}}{\rho_L}\right)^2 + \left(\frac{v_j}{q}\frac{\partial q}{\partial v_j}\frac{\varepsilon_{v_j}}{v_j}\right)^2 + \\ \qquad \left(\frac{\rho_\infty}{q}\frac{\partial q}{\partial \rho_\infty}\frac{\varepsilon_{\rho_\infty}}{\rho_\infty}\right)^2 + \left(\frac{u_\infty}{q}\frac{\partial q}{\partial u_\infty}\frac{\varepsilon_{u_\infty}}{u_\infty}\right)^2\end{array}} \tag{4.37}$$

Which reduces to

$$\frac{\varepsilon_q}{q} = 2\sqrt{\left(\frac{\varepsilon_{\rho_L}}{\rho_L}\right)^2 + \left(\frac{\varepsilon_{v_j}}{v_j}\right)^2 + \left(\frac{\varepsilon_{\rho_\infty}}{\rho_\infty}\right)^2 + \left(\frac{\varepsilon_{u_\infty}}{u_\infty}\right)^2} \tag{4.38}$$

4.11 Final Programming Considerations

4.11.1 Masking Optically Dense Core and Wind Tunnel Walls

Obviously, no drops should be detected in the optically dense jet core and the wind tunnel walls. However, because of reflections, overlapping interference patters, and general noise, it is possible for the program's edge detection routines to identify false positives. The solution is to mask off the results from regions in which droplets cannot exist. This is done by segmenting and hole filling each reconstruction into a binary image by a pixel value that it so dark that it could not be noise or interference fringes. To create the mask, any pixels in the region that are not connected to the image border are removed. What remains is the binary mask, which is laid on top of the reconstruction. Any detected drops which contain pixels that intersect the mask are removed.

4.11.2 Expansion and Parallelization

One final benefit of the current approach to spray analysis is it is easily expandable to other types of analysis and it is readily parallelizable. Additional subroutines to calculate acceleration and even jerk, incorporate streaks, or add additional views could be added without disrupting the base program. The program is well suited for cluster computing because the image reconstruction steps and the image analysis steps are inherently evenly distributed loads. And, the majority of the execution time is imbedded in a good loop structure where the execution order is independent across nodes.

Chapter V. Experimental Results

5.1 Unprocessed Results

5.1.1 Size and 3D Distribution

The results for the aerated liquid jet holographic analyses are demonstrated in the following figures. For reference, the compiled images of the spray from Chapter III are included. The area near the injector floor in the figures are composed of a high number density, wide span of very small droplets separated from the main, high density core. This region immediately downstream of the injector, under the jet core, features a continuous distribution of drops. Hence, while a wake of relatively large drops forms downstream of the injection site, the wake is not completely empty. The majority of the spray mass is concentrated at higher penetration heights in the spray field. This trend is evident in all of the test cases. This was also confirmed by the centerline images (Figures 3.15 through 3.19). The droplet size steadily increases with increasing distance from the wind tunnel floor to the jet central core. As the width and the height of the plumes increase (due to decreasing crossflow Mach number or increasing aeration), the number density of fine droplets decreases. Furthermore, no large drops are found in or near the wake. Note that while the results show two distinct lobes, the actual distribution is more continuous. However, due to the limitation inherent to transmission holography, the smallest droplets that are clearly visible near the tunnel floor would be masked by the large droplets and their interference fringes at higher elevations. This highlights the difficulty transmission holography can have at the main core because the spray becomes “opaque” to the experiment.

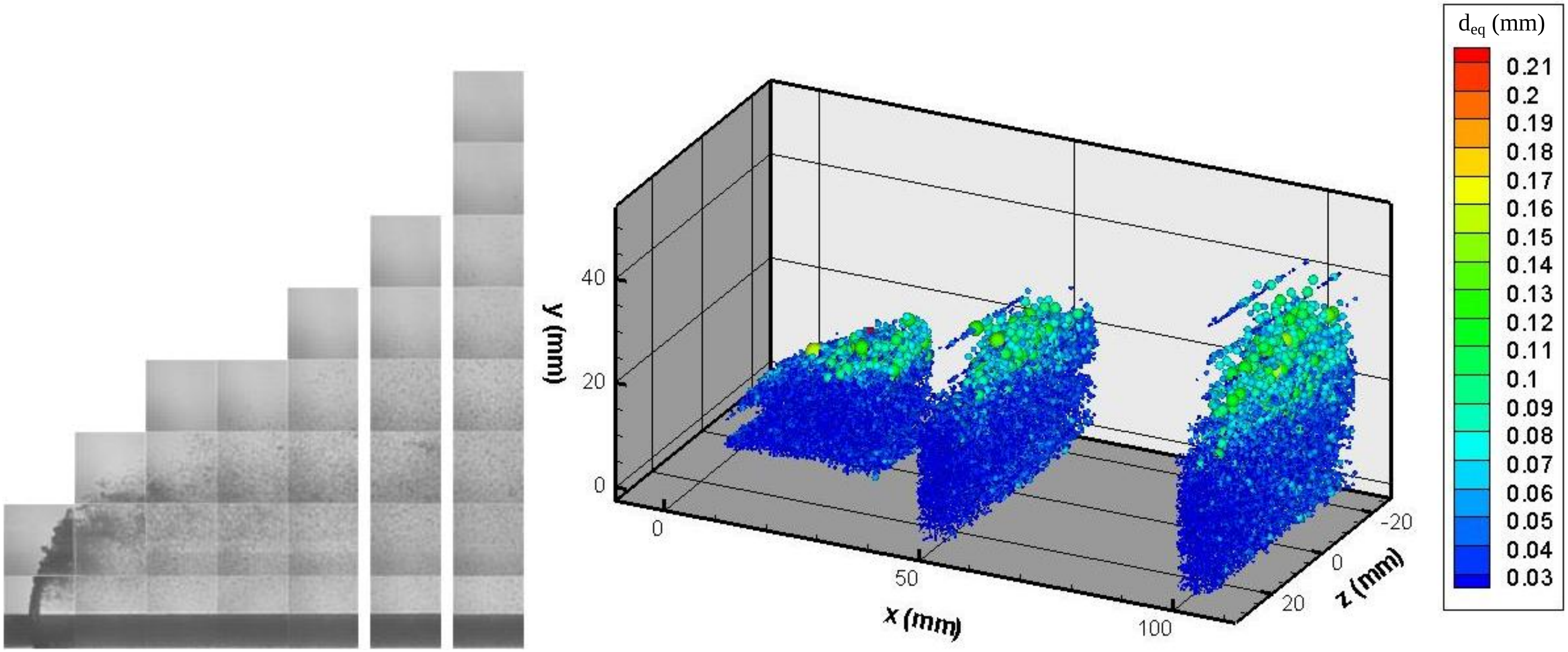

(a) (b)

Figure 5.1 (a) 5x5mm^2 Combined Reconstructions and (b) 3D and Size Results From Test Condition A (M = 0.3, GLR = 0%, q = 10, d = 1mm).

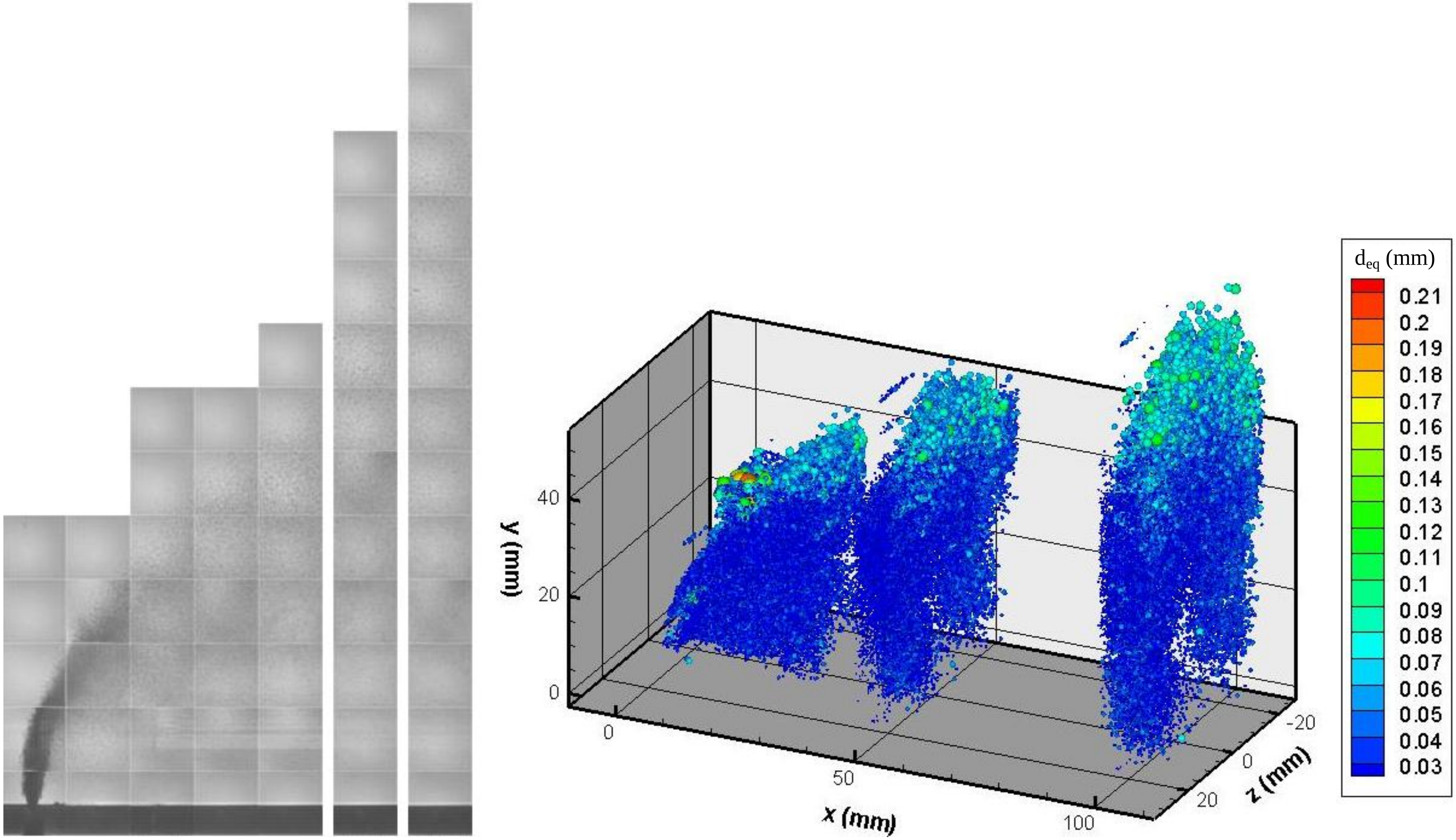

(a) (b)

Figure 5.2 (a) 5x5mm^2 Combined Reconstructions and (b) 3D and Size Results From Test Condition B (M = 0.3, GLR = 4%, q = 10, d = 1mm).

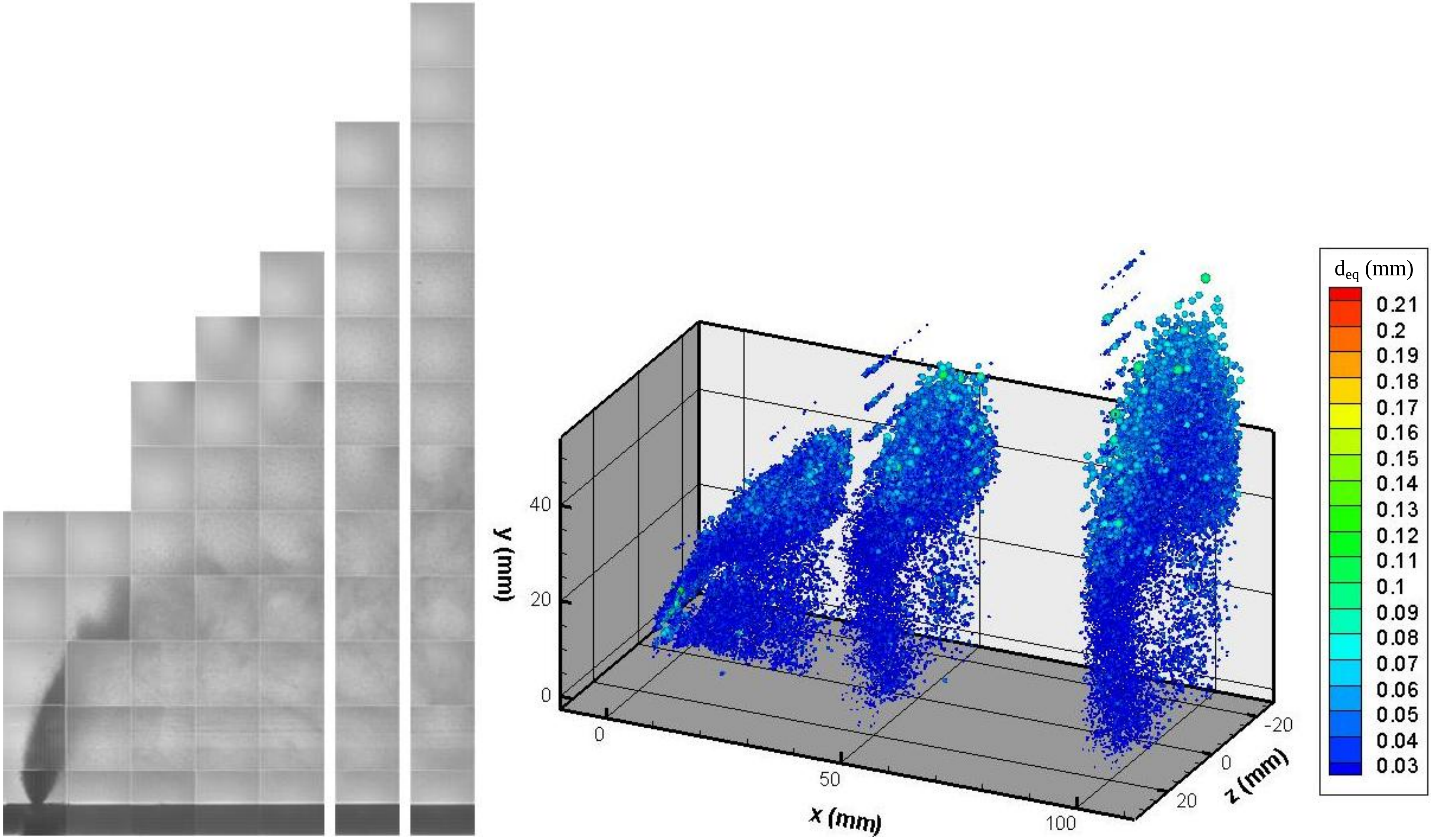

(a) (b)

Figure 5.3 (a) 5x5mm^2 Combined Reconstructions and (b) 3D and Size Results From of Test Condition C (M = 0.3, GLR = 8%, q = 10, d = 1mm).

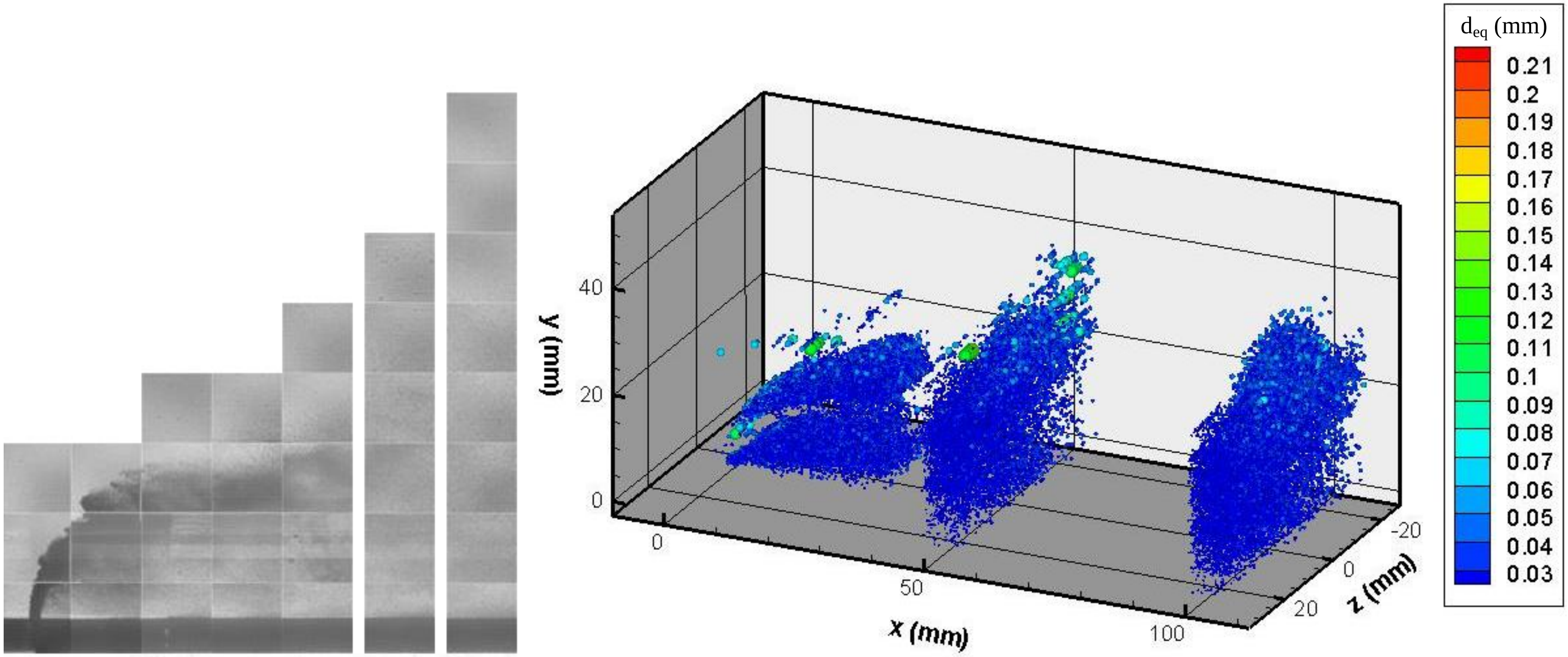

(a) (b)

Figure 5.4 (a) 5x5mm^2 Combined Reconstructions and (b) 3D and Size Results From Test Condition D (M = 0.6, GLR = 0%, q = 10, d = 1mm).

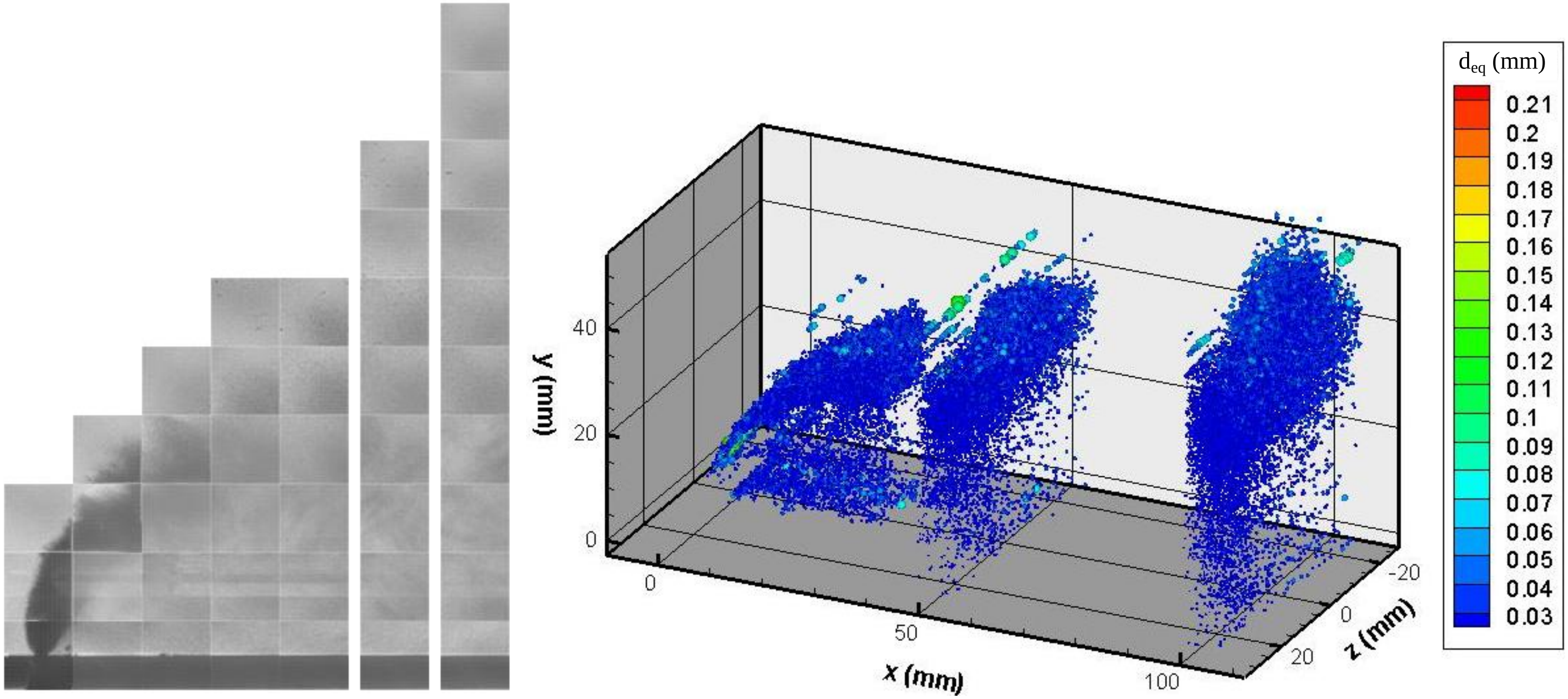

(a) (b)

Figure 5.5 5x5mm^2 Combined Reconstructions and (b) 3D and Size Results From Test Condition E (M = 0.6, GLR = 4%, q = 10, d = 1mm).

Figures 5.1 through 5.5 show the spray for each test condition. Each spray was investigated at x/d = 0..25, 50, and 100. The injector is at the (x,y,z) origin, mounted in the floor and sprays straight up into the crossflow. The x axis marks the cross flow downstream location, the y axis is the penetration height, and the z axis gives the spanwise distance from the centerline. The spheres represent individual detected drops within the 3D space. The sphere size and color indicate the equivalent diameter of the detected drops. Some sprays have a gap in the data near the injector from the dense spray core. Note that this is different from the less dense locations that reflect the wake induced by the jet.

5.1.2 Recovery Ratio

The effectiveness of the algorithm can be measured by comparing the detected mass flux to the known injection rate, the recovery ratio; see Eqn. 5.1.

$$Recovery\ Ratio = \frac{\pi\, \rho\, \hat{u}\, SMD^2/4}{\dot{m_{inj}}} \tag{5.1}$$

The recovery ratio is presented for the test conditions at various downstream locations in Table 5.1. Given the difficulties associated with small droplets and particle tracking, the more accurate mass averaged values are used.

Table 5.1 Recovery Ratio Percentage.

	Downstream Location (x/d)				
Test Matrix	5	15	25	50	100
A(M=.3,GLR=0)	25	80	85	80	90
B(M=.3,GLR=4)	30	85	85	80	90
C(M=.3,GLR=8)	25	65	80	75	90
D(M=.6,GLR=0)	50	60	65	75	85
E(M=.6,GLR=4)	40	70	75	75	90

For all test conditions, the recovery ratio is significantly lower at x/d=5 than elsewhere in the spray. The higher Mach number locations also had a reduced ratio due to experimental difficulties in keeping the wind tunnel glass clean. As expected, the far field locations have a higher recovery ratio because their holograms were much less noisy. Another good indicator of a successful experiment is the recovery ratio becomes consistent across x values. Some of these locations are unexpectedly high. It could be possible that some drops are over-reported from experimental uncertainties. Additional analysis of larger quantities of sprays, and by multiple groups, would help reduce this uncertainty. It should be noted that on a similar test set, Lin, et al. (2002) also reported very high recovery ratios for some test conditions.

5.1.3 Velocity Distribution

Sample velocity distributions are given in Figures 5.6 through 5.10. Again the size and color of the spheres represent the equivalent diameter (mm). The vector attached to each drop represents the direction and magnitude of the velocity. The vector color represents the horizontal velocity component (m/s). Throughout the figures, the largest drops are the slowest to accelerate due to their higher mass. Also, drops closer to the tunnel floor tend to be slower. To increase the number of image pair matches, a generous search radius of 50% of the initial guess vector is used for PTV calculations. This allows many individual velocity vectors that deviate from the general flow field.

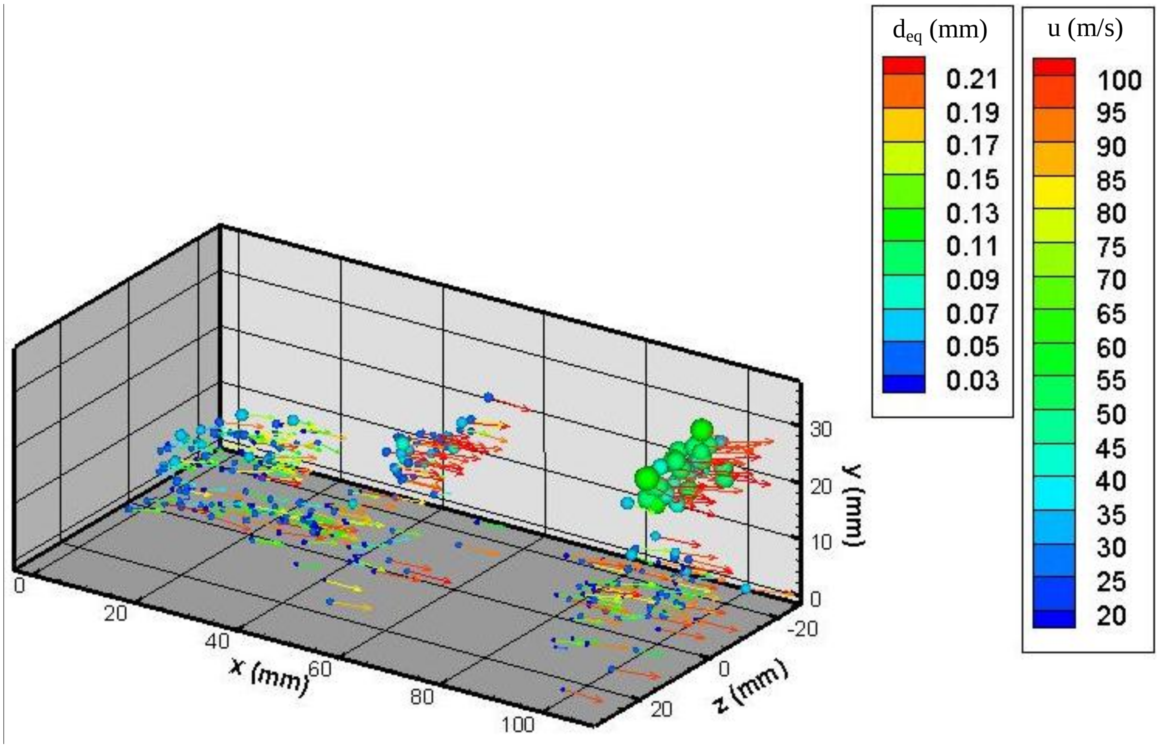

Figure 5.6 Sample Velocity Distribution for Test Condition A (M = 0.3, u_∞=103.1 m/s, GLR = 0%, q = 10, d = 1mm).

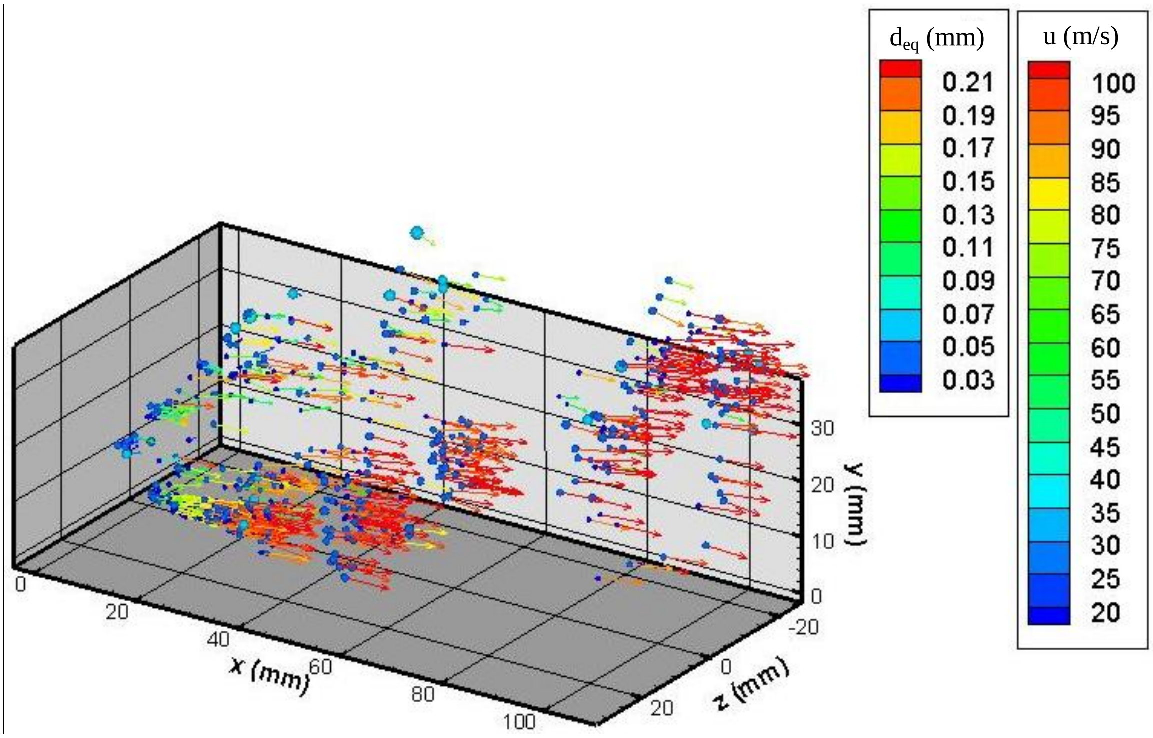

Figure 5.7 Sample Velocity Distribution for Test Condition B (M = 0.3, u_∞=103.1 m/s, GLR = 4%, q = 10, d = 1mm).

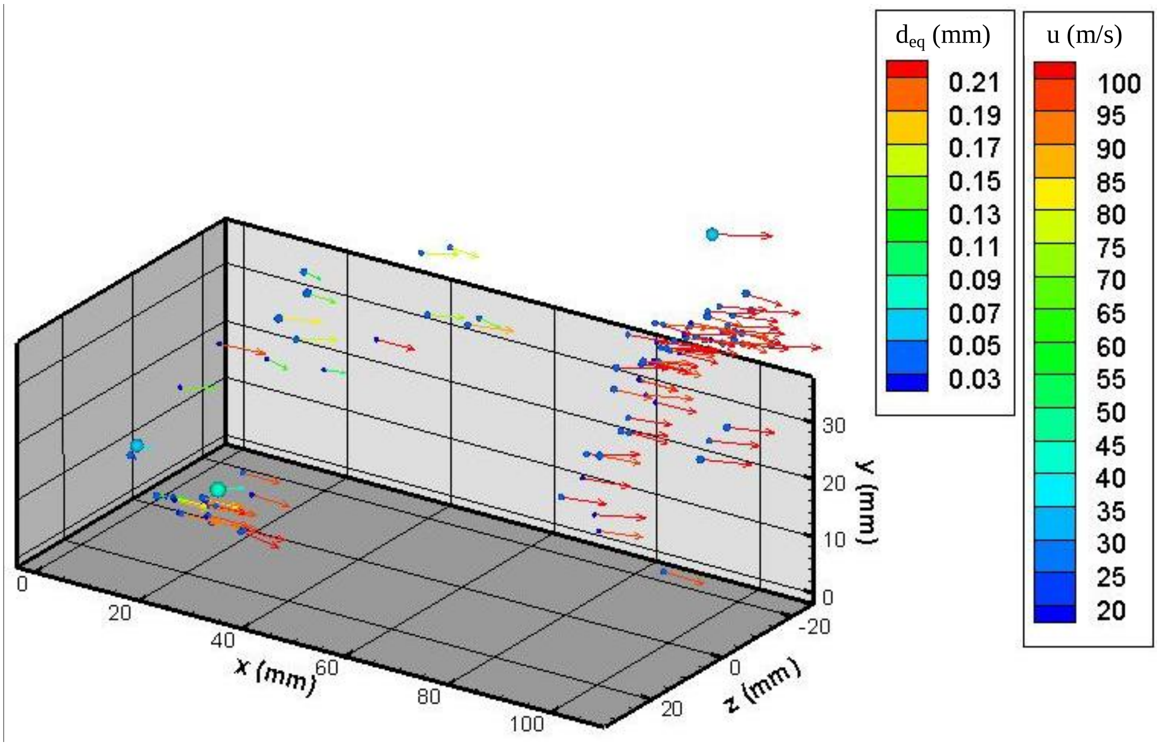

Figure 5.8 Sample Velocity Distribution for Test Condition C (M = 0.3, u_∞=103.1 m/s, GLR = 8%, q = 10, d = 1mm).

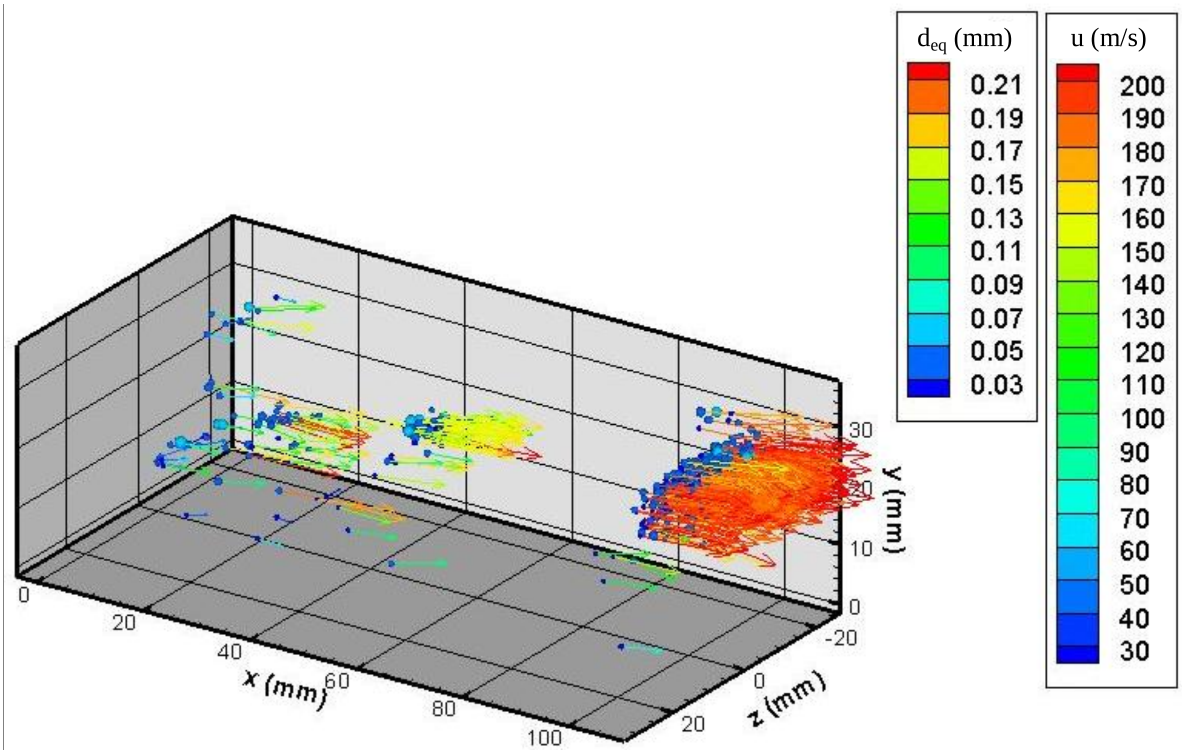

Figure 5.9 Sample Velocity Distribution for Test Condition D (M = 0.6, u_∞=206.3 m/s, GLR = 0%, q = 10, d = 1mm).

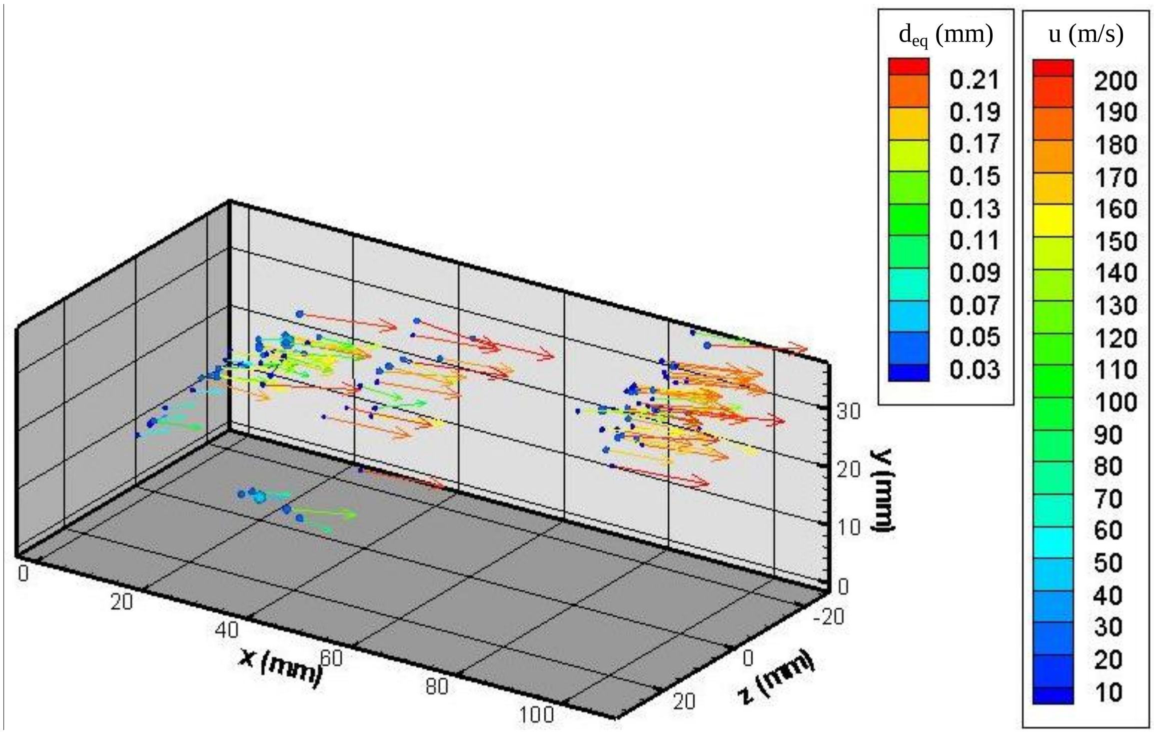

Figure 5.10 Sample Velocity Distribution for Test Condition E (M = 0.6, u_∞=206.3 m/s, GLR = 4%, q = 10, d = 1mm).

5.2 Spray Properties

5.2.1 Size Distribution

Table 5.2(a-f) and Figure 5.11 through Figure 5.15 give the experimental equivalent diameter distribution data for drops for their respective test cases. Each figure is presented on a Rosin-Rammler scale and a logarithm scale for clarity. To maximize the total sample size, the same 10mm spans used in Table 5.1 are repeated here. The greatest variability in drop size is for the pure liquid jet cases (A and D). The variability decreases with increasing downstream location. The majority of droplets are in the 30 – 40 micrometer range.

The Rosin-Rammler function is a cumulative volume density function that can be used to characterize the distribution of drop sizes (Ashgriz, 2011, Liu, 1999); see Eqn. 5.2.

$$CV_i = 1 - e^{-\left({d_i}/{\delta}\right)^q} \qquad (5.2)$$

CV_i is the cumulative volume distribution for all drops up to and including drops with diameter i,(d_i). q and δ are the fitting parameters which will define the drop size distribution. Small q corresponds to a large range of drop sizes. Eqn. 5.2 can be linearized to obtain Eqn. 5.3.

$$ln\big(-ln(1 - CV_i)\big) = q\ ln(d_i) - q\ ln(\delta) \tag{5.3}$$

Using the experimentally calculated CV_i, this is what is plotted in Figs. 5.11a-5.15a. q is the slope of Eqn. 5.3 and it is the slope of the linear regressions in Figs. 5.11a-5.15a. Results for q are given in Table 5.2f.

Table 5.2a Equivalent Diameter Distribution.

	deq (μm)	**x/dj=5**	**x/dj=15**	**x/dj=25**	**x/dj=50**	**x/dj=100**
Test A (M=.3, GLR = 0%)	15	0.00E+00	0.00E+00	0.00E+00	0.00E+00	0.00E+00
	30	3.39E-01	4.19E-01	3.55E-01	3.87E-01	3.48E-01
	45	5.84E-01	5.23E-01	4.87E-01	4.57E-01	4.27E-01
	60	7.12E-02	4.30E-02	8.35E-02	1.01E-01	1.37E-01
	75	5.04E-03	1.07E-02	4.58E-02	3.43E-02	5.49E-02
	90	7.19E-04	3.48E-03	2.02E-02	1.32E-02	2.11E-02
	105	0.00E+00	6.32E-04	6.44E-03	6.06E-03	8.10E-03
	120	0.00E+00	6.32E-04	1.61E-03	1.73E-03	3.00E-03
	135	0.00E+00	0.00E+00	4.60E-04	4.33E-04	1.18E-03
	150	0.00E+00	0.00E+00	0.00E+00	1.08E-04	1.82E-04
	165	0.00E+00	3.16E-04	0.00E+00	0.00E+00	0.00E+00
	180	0.00E+00	0.00E+00	0.00E+00	0.00E+00	0.00E+00
	195	0.00E+00	0.00E+00	2.30E-04	0.00E+00	0.00E+00

Table 5.2b Equivalent Diameter Distribution.

	deq (μm)	x/dj=5	x/dj=15	x/dj=25	x/dj=50	x/dj=100
Test B (M=.3, GLR = 4%)	15	0.00E+00	0.00E+00	0.00E+00	0.00E+00	0.00E+00
	30	3.88E-01	4.30E-01	4.07E-01	4.22E-01	3.27E-01
	45	5.23E-01	4.67E-01	4.54E-01	4.24E-01	4.32E-01
	60	7.77E-02	7.95E-02	1.12E-01	1.14E-01	1.60E-01
	75	8.04E-03	1.33E-02	2.25E-02	3.13E-02	6.07E-02
	90	2.30E-03	5.02E-03	5.02E-03	7.00E-03	1.62E-02
	105	7.66E-04	1.54E-03	0.00E+00	1.27E-03	3.27E-03
	120	3.83E-04	1.35E-03	0.00E+00	6.66E-05	3.47E-04
	135	0.00E+00	3.86E-04	0.00E+00	0.00E+00	0.00E+00
	150	0.00E+00	3.86E-04	0.00E+00	0.00E+00	0.00E+00
	165	0.00E+00	1.93E-04	0.00E+00	0.00E+00	0.00E+00
	180	0.00E+00	5.79E-04	0.00E+00	0.00E+00	0.00E+00
	195	0.00E+00	0.00E+00	0.00E+00	0.00E+00	0.00E+00

Table 5.2c Equivalent Diameter Distribution.

	deq (μm)	x/dj=5	x/dj=15	x/dj=25	x/dj=50	x/dj=100
Test C (M=.3, GLR = 8%)	15	0.00E+00	0.00E+00	0.00E+00	0.00E+00	0.00E+00
	30	4.70E-01	5.69E-01	4.88E-01	4.75E-01	4.45E-01
	45	4.68E-01	3.99E-01	4.57E-01	4.30E-01	4.41E-01
	60	5.39E-02	2.91E-02	5.09E-02	8.24E-02	9.73E-02
	75	6.45E-03	1.24E-03	4.44E-03	9.92E-03	1.46E-02
	90	1.76E-03	6.19E-04	2.22E-04	1.72E-03	2.12E-03
	105	0.00E+00	3.09E-04	0.00E+00	2.86E-04	3.53E-04
	120	0.00E+00	0.00E+00	0.00E+00	0.00E+00	0.00E+00
	135	0.00E+00	0.00E+00	0.00E+00	0.00E+00	0.00E+00
	150	0.00E+00	0.00E+00	0.00E+00	0.00E+00	0.00E+00
	165	0.00E+00	0.00E+00	0.00E+00	0.00E+00	0.00E+00
	180	0.00E+00	0.00E+00	0.00E+00	0.00E+00	0.00E+00
	195	0.00E+00	0.00E+00	0.00E+00	0.00E+00	0.00E+00

Table 5.2d Equivalent Diameter Distribution.

	deq (μm)	x/dj=5	x/dj=15	x/dj=25	x/dj=50	x/dj=100
Test D (M=.6, GLR = 0%)	15	0.00E+00	0.00E+00	0.00E+00	0.00E+00	0.00E+00
	30	3.88E-01	6.16E-01	5.88E-01	6.95E-01	6.07E-01
	45	5.27E-01	3.64E-01	4.00E-01	2.83E-01	3.77E-01
	60	7.36E-02	1.51E-02	1.14E-02	1.63E-02	1.50E-02
	75	7.55E-03	1.77E-03	0.00E+00	3.11E-03	5.41E-04
	90	2.83E-03	1.77E-03	0.00E+00	1.41E-03	0.00E+00
	105	9.43E-04	4.43E-04	0.00E+00	7.07E-04	0.00E+00
	120	0.00E+00	8.86E-04	0.00E+00	1.41E-04	0.00E+00
	135	0.00E+00	0.00E+00	0.00E+00	4.24E-04	0.00E+00
	150	0.00E+00	0.00E+00	0.00E+00	0.00E+00	0.00E+00
	165	0.00E+00	0.00E+00	0.00E+00	0.00E+00	0.00E+00
	180	0.00E+00	0.00E+00	0.00E+00	0.00E+00	0.00E+00
	195	0.00E+00	0.00E+00	0.00E+00	0.00E+00	0.00E+00

Table 5.2e Equivalent Diameter Distribution.

	deq (μm)	x/dj=5	x/dj=15	x/dj=25	x/dj=50	x/dj=100
Test E (M=.6, GLR = 4%)	15	0.00E+00	0.00E+00	0.00E+00	0.00E+00	0.00E+00
	30	4.73E-01	6.42E-01	6.53E-01	7.16E-01	6.91E-01
	45	4.62E-01	3.41E-01	3.36E-01	2.69E-01	2.99E-01
	60	5.38E-02	1.49E-02	8.80E-03	1.10E-02	8.70E-03
	75	8.67E-03	1.92E-03	1.52E-03	2.11E-03	1.23E-03
	90	1.73E-03	0.00E+00	0.00E+00	1.13E-03	4.73E-04
	105	8.67E-04	0.00E+00	0.00E+00	5.63E-04	0.00E+00
	120	0.00E+00	0.00E+00	0.00E+00	0.00E+00	0.00E+00
	135	0.00E+00	0.00E+00	0.00E+00	1.41E-04	0.00E+00
	150	0.00E+00	0.00E+00	0.00E+00	0.00E+00	0.00E+00
	165	0.00E+00	0.00E+00	0.00E+00	0.00E+00	0.00E+00
	180	0.00E+00	0.00E+00	0.00E+00	0.00E+00	0.00E+00
	195	0.00E+00	0.00E+00	0.00E+00	0.00E+00	0.00E+00

Table 5.2f Rosin-Rammler Distribution Slope and Intercept Parameters *q* and δ.

	M	**GLR**	**Test**	**x/d_j=5**	**x/d_j=15**	**x/d_j=25**	**x/d_j=50**	**x/d_j=100**
q	0.3	0	A	4.66	1.89	2.45	2.46	2.90
	0.3	4	B	2.67	2.08	3.50	3.02	3.31
	0.3	8	C	4.14	2.51	3.63	3.61	3.15
	0.6	0	D	5.44	3.03	1.69	4.74	2.00
	0.6	4	E	3.45	2.75	3.45	3.33	1.63
δ	0.3	0	A	45.6	52.2	67.1	63.6	65.0
	0.3	4	B	50.6	62.3	50.9	54.4	61.0
	0.3	8	C	44.3	40.9	43.2	47.0	49.2
	0.6	0	D	36.5	49.5	41.2	37.5	41.8
	0.6	4	E	37.6	47.2	36.6	36.9	36.0

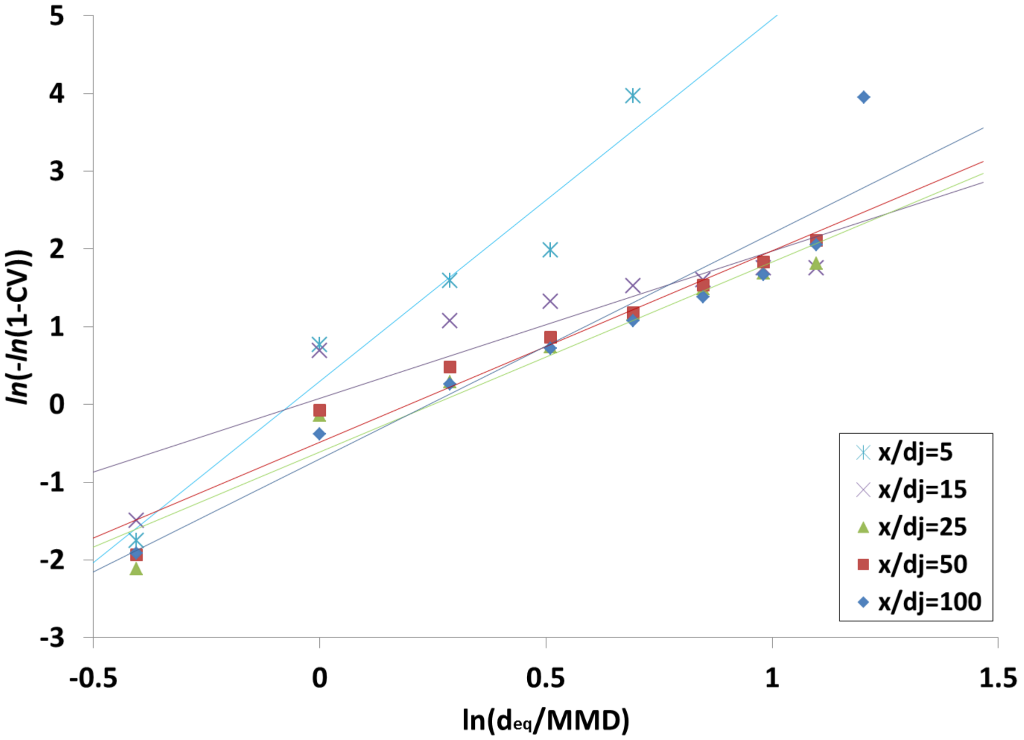

(a) Rosin-Rammler Scale

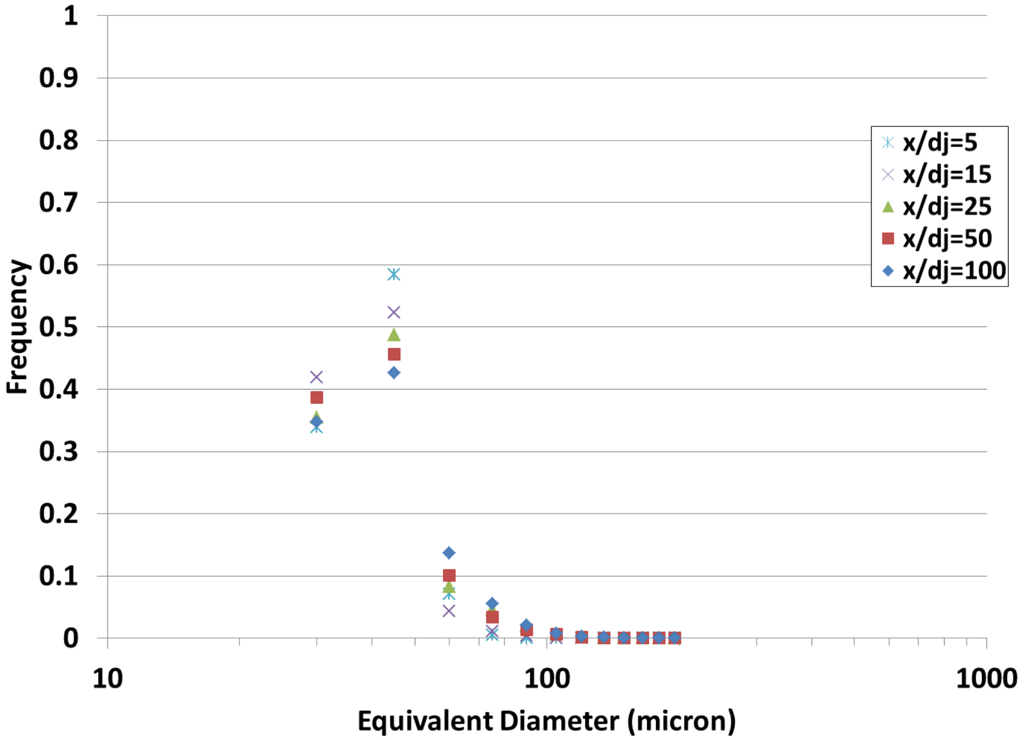

(b) Log Scale

Figure 5.11 Equivalent Diameter Distribution for Test Condition A (M = 0.3, GLR = 0%, q = 10, d = 1mm).

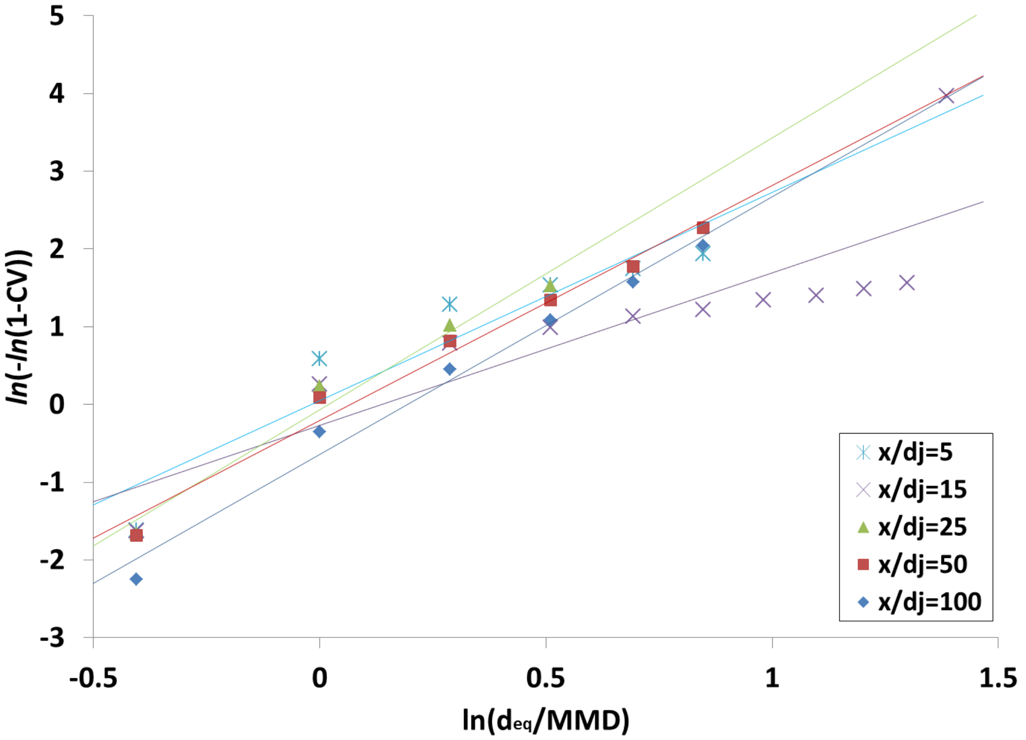

(a) Rosin-Rammler Scale

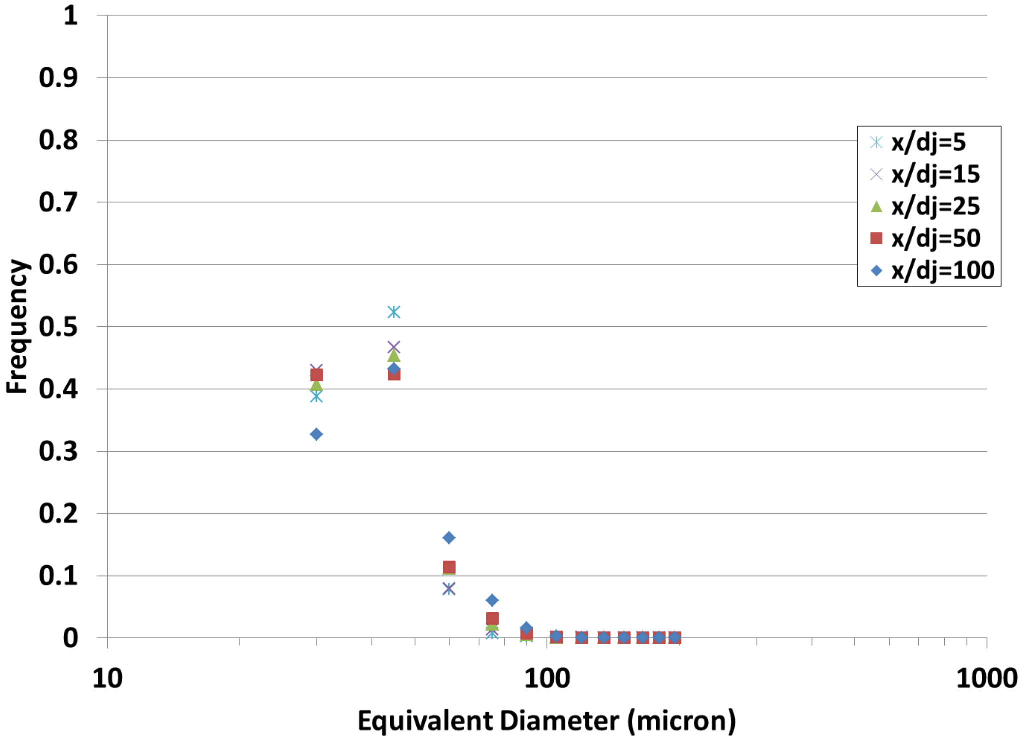

(b) Log Scale

Figure 5.12 Equivalent Diameter Distribution for Test Condition B (M = 0.3, GLR = 4%, q = 10, d = 1mm).

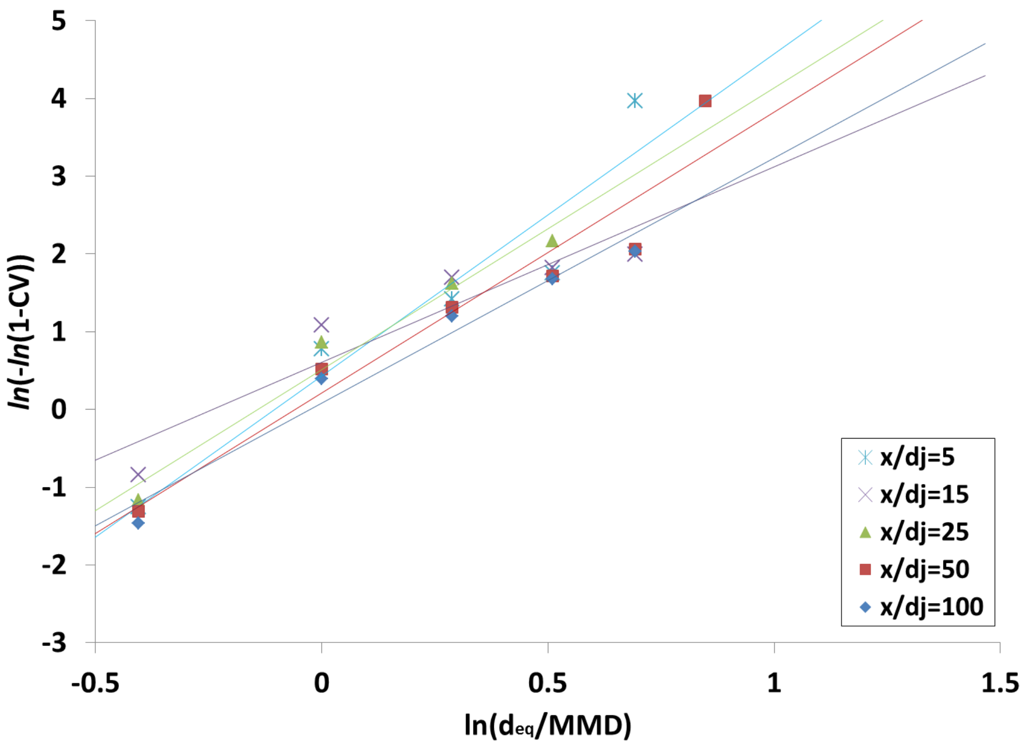

(a) Rosin-Rammler Scale

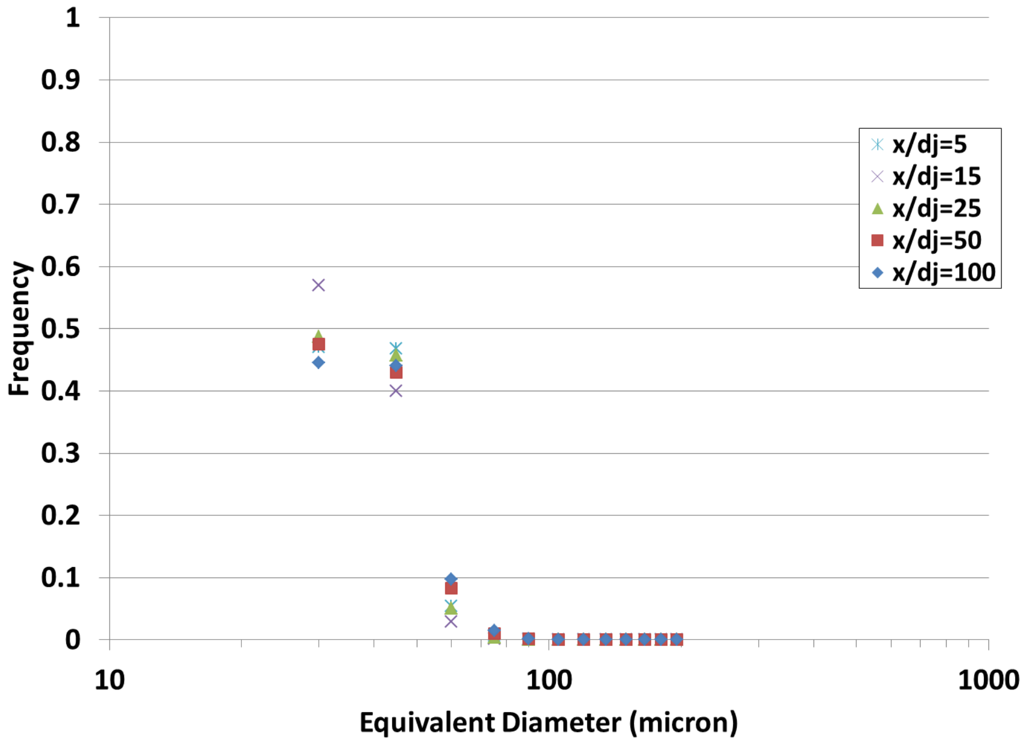

(b) Log Scale

Figure 5.13 Equivalent Diameter Distribution Test Condition C
(M = 0.3, GLR = 8%, q = 10, d = 1mm).

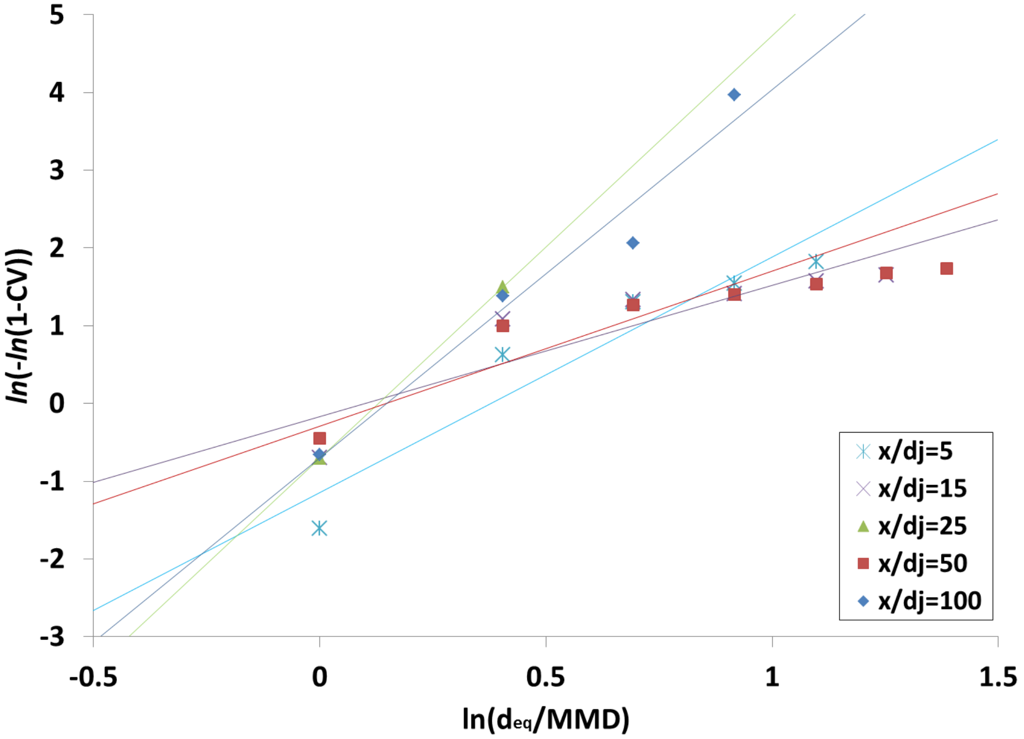

(a) Rosin-Rammler Scale

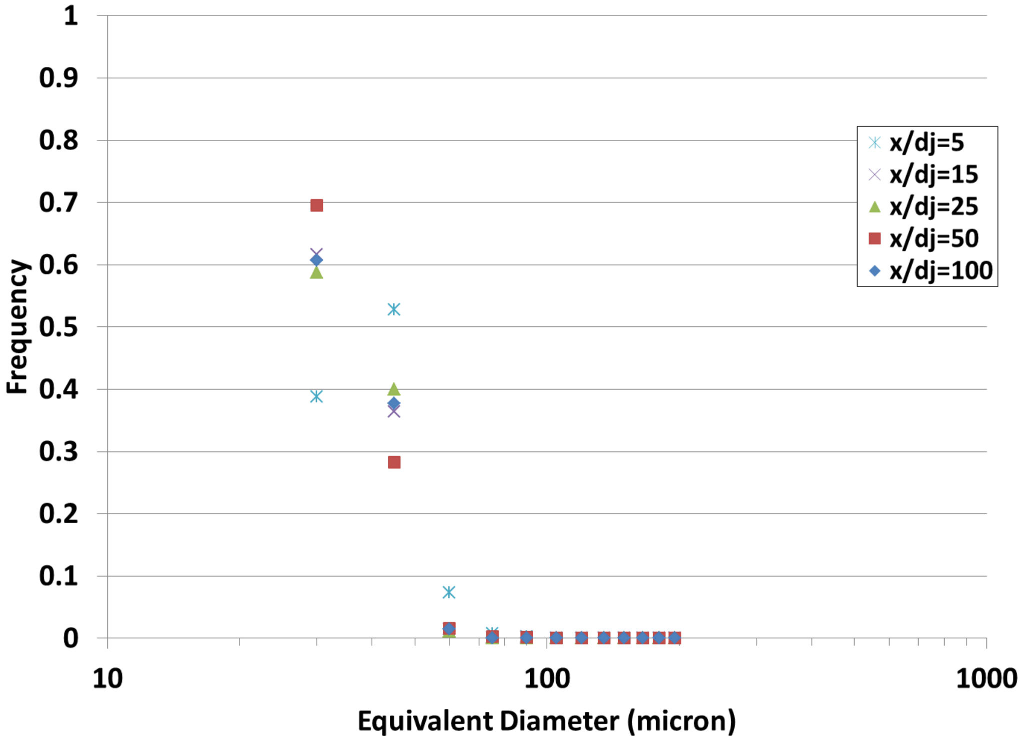

(b) Log Scale

Figure 5.14 Equivalent Diameter Distribution for Test Condition D (M = 0.6, GLR = 0%, q = 10, d = 1mm).

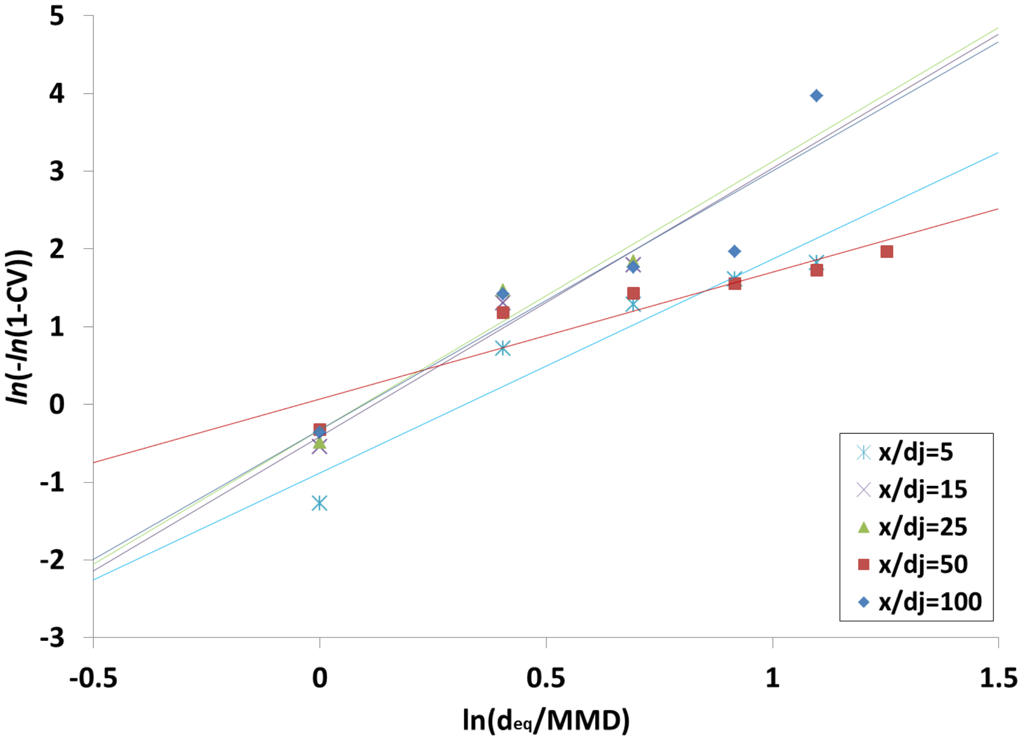

(a) Rosin-Rammler Scale

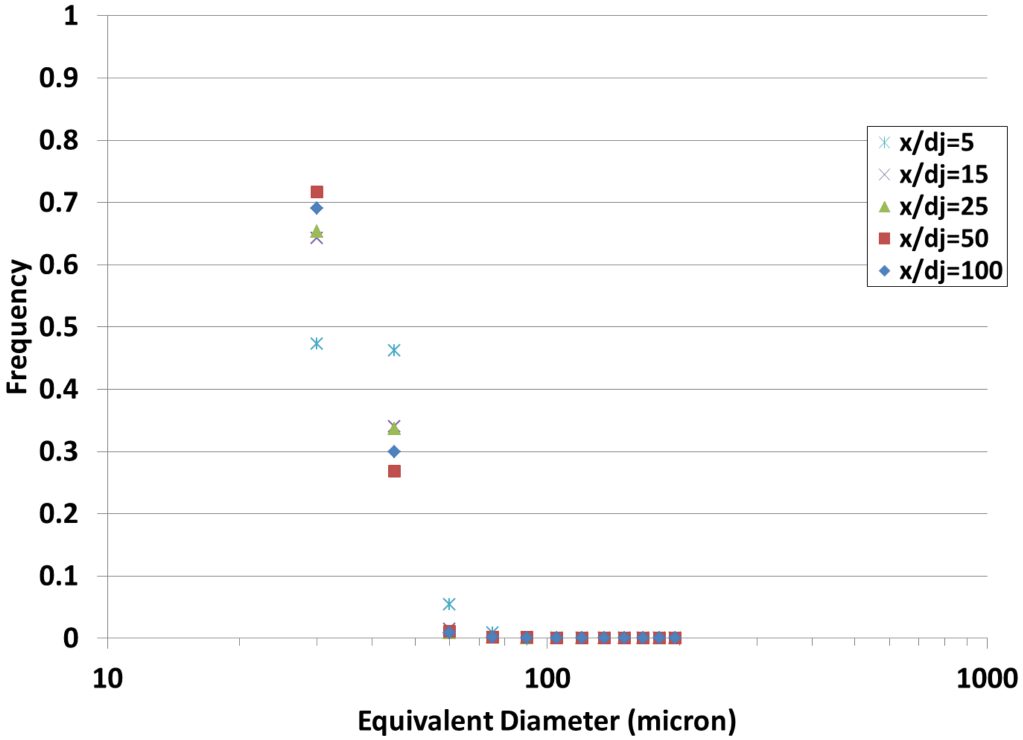

(b) Log Scale

Figure 5.15 Equivalent Diameter Distribution for Test Condition E (M = 0.6, GLR = 4%, q = 10, d = 1mm).

5.2.2 Sauter Mean Diameter

Following the standard least squares regression methods detailed in Bates and Watts (1988) and Myers et al. (2002), correlations were developed from the results. The first correlation for Sauter Mean Diameter was found for Test Conditions A and D (pure liquid jet):

$$\left.\frac{SMD}{d_0}\right|_{\substack{pure\\liquid\\jet}} = .031x^{-.008}M^{-.27}, x > 0 \tag{5.4}$$

Where the mean and standard deviation of the ratio of the predicted to measured SMD/d are 1.01 and 13.5%. The uncertainty of the final regression (includes uncertainty of the regression and the algorithm false positive rate) is +/-4.3 microns with a confidence of 89%.

A correlation for the Sauter Mean Diameter (SMD) for only aerated liquid jets was also calculated:

$$\left.\frac{SMD}{d_0}\right|_{\substack{aerated\\liquid\\jet}} = .039x^{-.007}GLR^{-.28}M^{-.45}, x > 0, GLR > 0 \tag{5.5}$$

Where the mean and standard deviation of the ratio of the predicted to measured SMD/d are 1.01 and 13.6%. The uncertainty of the final regression (incorporating the uncertainty of the mathematics of the regression and the false positive rate per Eqn. 4.14) is +/-4.8 microns with a confidence of 89%.

The previous two equations can be combined so the aeration contribution is clearly separated from the pure liquid jet contribution:

$$\left.\frac{SMD}{d_0}\right|_{\substack{aerated\\liquid\\jet}} = \left[\left.\frac{SMD}{d_0}\right|_{\substack{pure\\liquid\\jet}}\right] \cdot \left[1.26x^{-.0009}GLR^{-.28}M^{-.18}\right],\ x > 0, GLR > 0 \qquad (5.6)$$

In this form, the correlation has a +/-9 micron uncertainty at a confidence of 89%. The mean and standard deviation of the ratio of the predicted to measured SMD/d are 1.02 and 13.7%.

The correlations for SMD(x) for pure liquid jet and aerated jet (Eqns. 5.4 and 5.5) are plotted against the volume averaged (by downstream location) experimental results; see Figures 5.16 through 5.20. The average SMD data points are presented in Table 5.3.

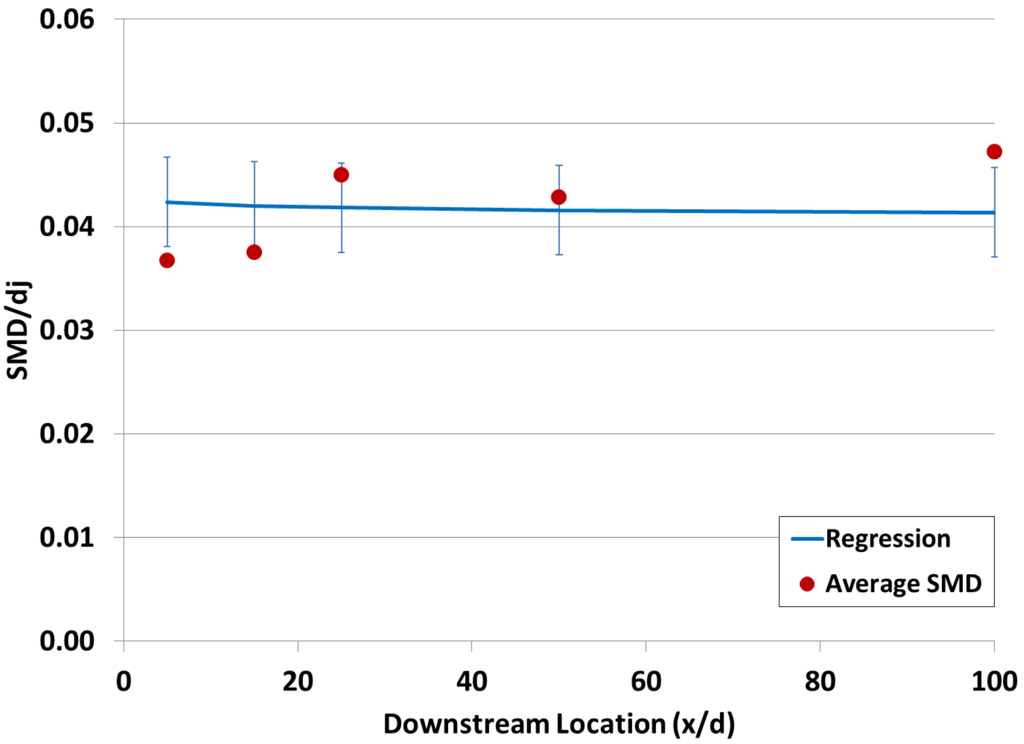

Figure 5.16 SMD/d_j for Test Case A
(M = 0.3, GLR = 0%, q = 10, d = 1mm).

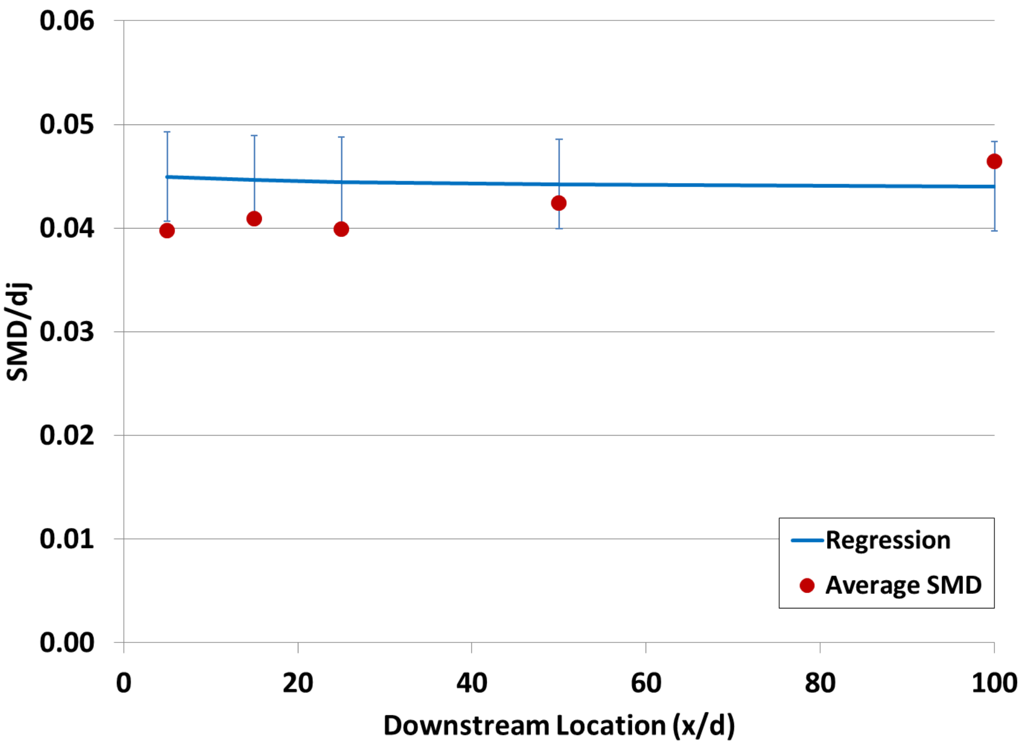

Figure 5.17 SMD/d_j for Test Case B
(M = 0.3, GLR = 4%, q = 10, d = 1mm).

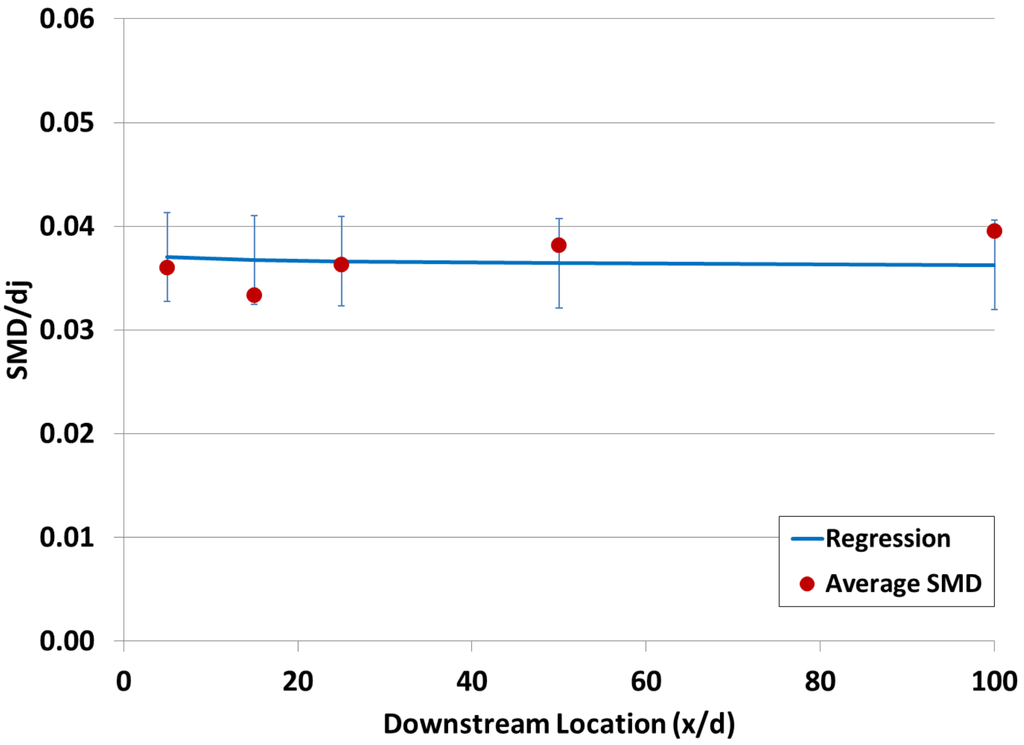

Figure 5.18 SMD/d_j for Test Case C
(M = 0.3, GLR = 8%, q = 10, d = 1mm).

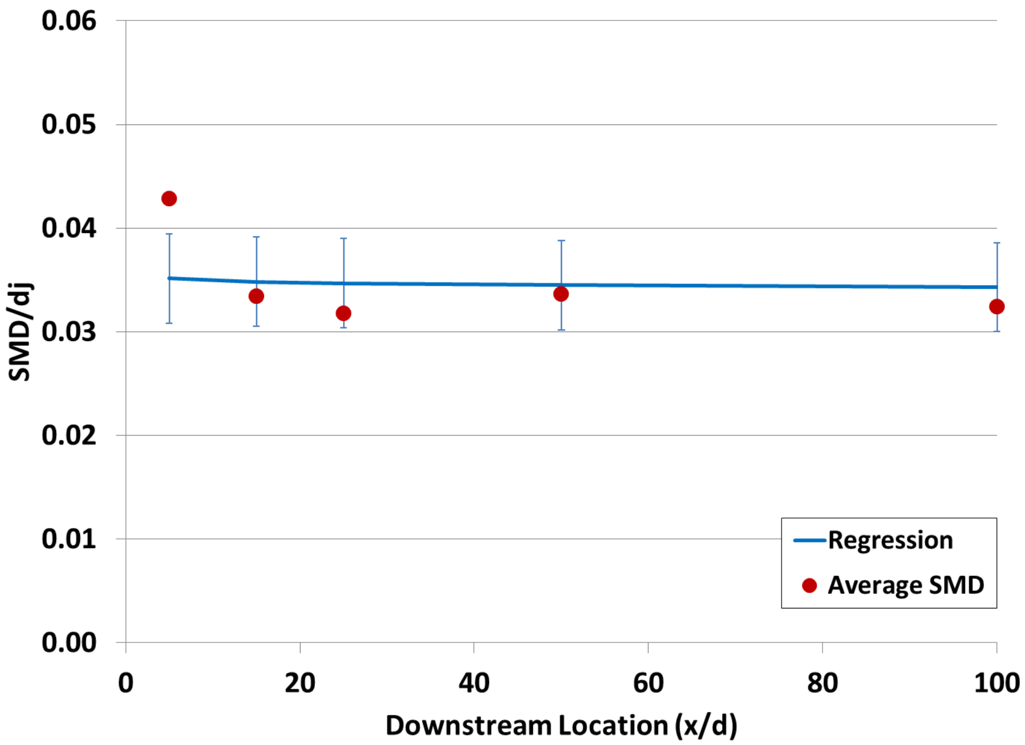

Figure 5.19 SMD/d_j for Test Case D
(M = 0.6, GLR = 0%, q = 10, d = 1mm).

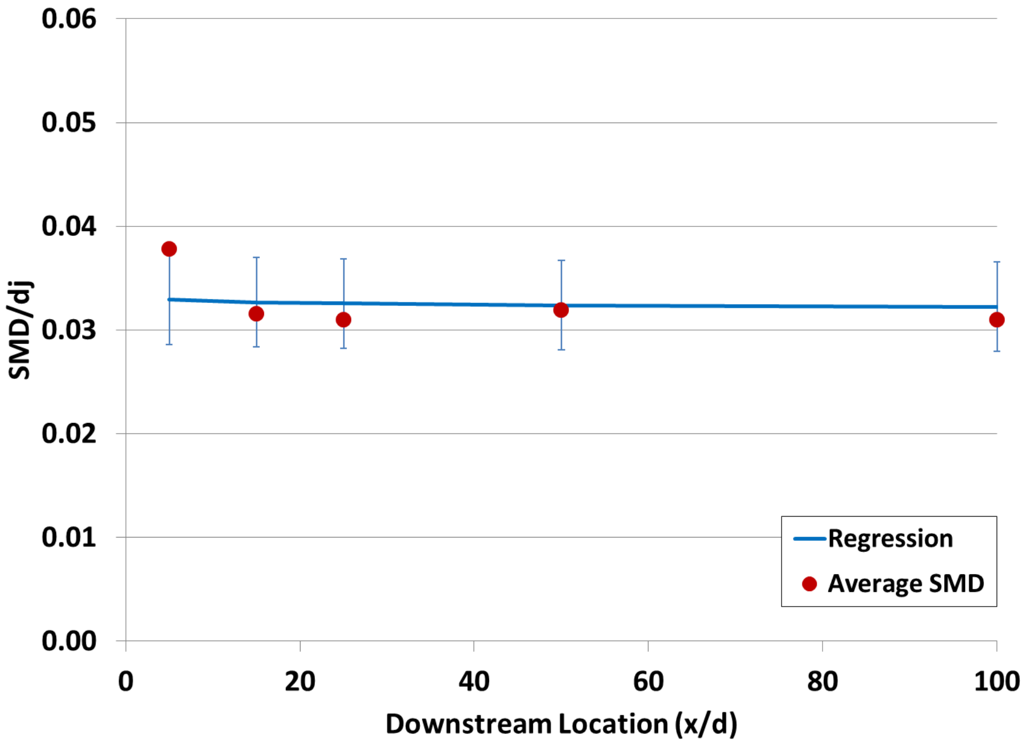

Figure 5.20 SMD/d_j for Test Case E
(M = 0.6, GLR = 4%, q = 10, d = 1mm).

Table 5.3 Downstream Location Average SMD/d_j.

	Downstream Location (x/d_j)				
Test Matrix	5	15	25	50	100
A(M=.3,GLR=0)	0.0367	0.0375	0.0450	0.0429	0.0472
B(M=.3,GLR=4)	0.0398	0.0409	0.0399	0.0424	0.0464
C(M=.3,GLR=8)	0.0360	0.0334	0.0363	0.0382	0.0395
D(M=.6,GLR=0)	0.0429	0.0334	0.0318	0.0337	0.0324
E(M=.6,GLR=4)	0.0378	0.0316	0.0310	0.0319	0.0310

Lin, et al. (2002) found that past $x/d > 50$, the effect of the downstream location was insignificant. By definition, the downstream location is important to the size in the near field; larger drops break up during secondary atomization. However, even with the near field data, the influence of x is much less than GLR or M for the given data set. SMD is inversely proportional to all three factors. One factor reducing the influence of the downstream location is the optical density at the injector. Per Table 5.1, the recovery ratio in the first few diameters downstream of the injector is very low. From the hologram reconstructions, this region is where most of the largest drops were found; and many had already split before leaving the optically dense core. A regression that allows for a greater bend near zero (e.g. SMD ~ -ln(x)) should be used if complete data at the injector ($x/d<5$) is available.

Also note that, compared to Lin et al. (2002), the effect of GLR has a larger influence in the near field than in far field only results relative to M. This is logical since the high speed cross flow has not had as much time to act on the drops in this dataset compared to far field results. This reinforces the need for aeration to accelerate the onset of secondary breakup. This will ensure that the unstable near field atomization zone is shortened.

Finally, note that all results were for an injector diameter of 1mm. In comparison, Lin, et al. (2002) used a 0.5 mm injector. The momentum flux ratio (q) was not varied in this project so its impact on the near field was not studied.

5.2.3 Velocity Distribution

Just as the mass of a drop is used to weight the diameter distribution, each velocity component can also be weighted:

$$\tilde{u} = \frac{\sum\limits_{alldrops} u_i d_{eq,i}^3}{\sum\limits_{alldrops} d_{eq,i}^3} \tag{5.7}$$

$$\tilde{v} = \frac{\sum\limits_{alldrops} v_i d_{eq,i}^3}{\sum\limits_{alldrops} d_{eq,i}^3} \tag{5.8}$$

5.2.3.1 Streamwise Mass Averaged Velocity

The streamwise (u) velocity profiles are charted by diameter in Figures 5.21 through Figure 5.25. Each series in each figure represents the velocity distribution at a different downstream location. Here the velocity is normalized by the mass averaged velocity and the diameter is normalized by the mass average diameter (SMD). Given the rapidly changing nature of the near injector region, a wide velocity distribution is to be expected. But the locations further downstream converge to a single value. Also, because of their inherent momentum, the largest drops are the slowest to take on the freestream velocity value.

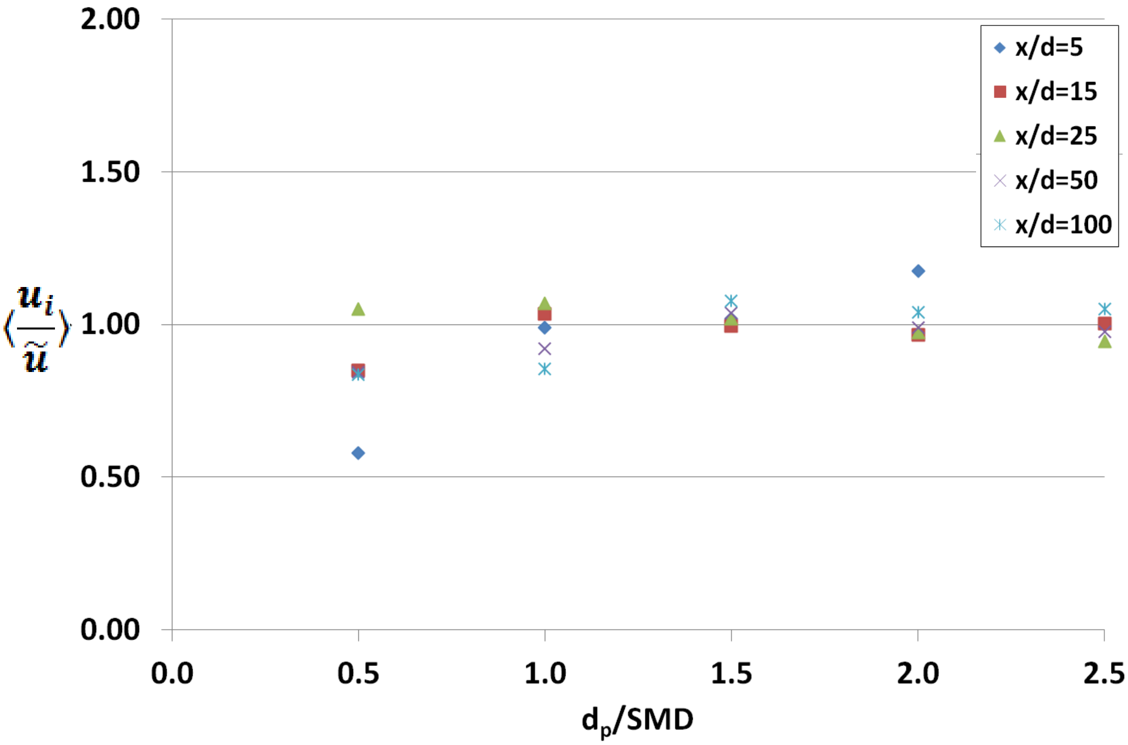

Figure 5.21 Mass Averaged Velocity for Test Case A
(M = 0.3, GLR = 0%, q = 10, d = 1mm).

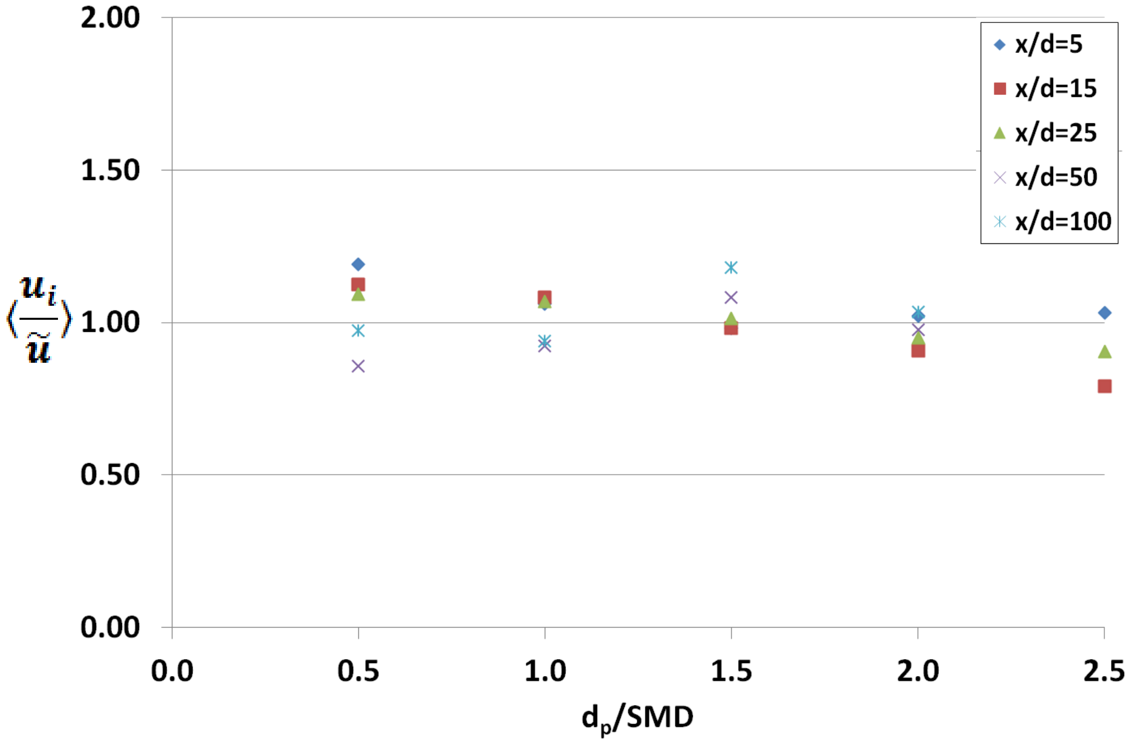

Figure 5.22 Mass Averaged Velocity for Test Case B
(M = 0.3, GLR = 4%, q = 10, d = 1mm).

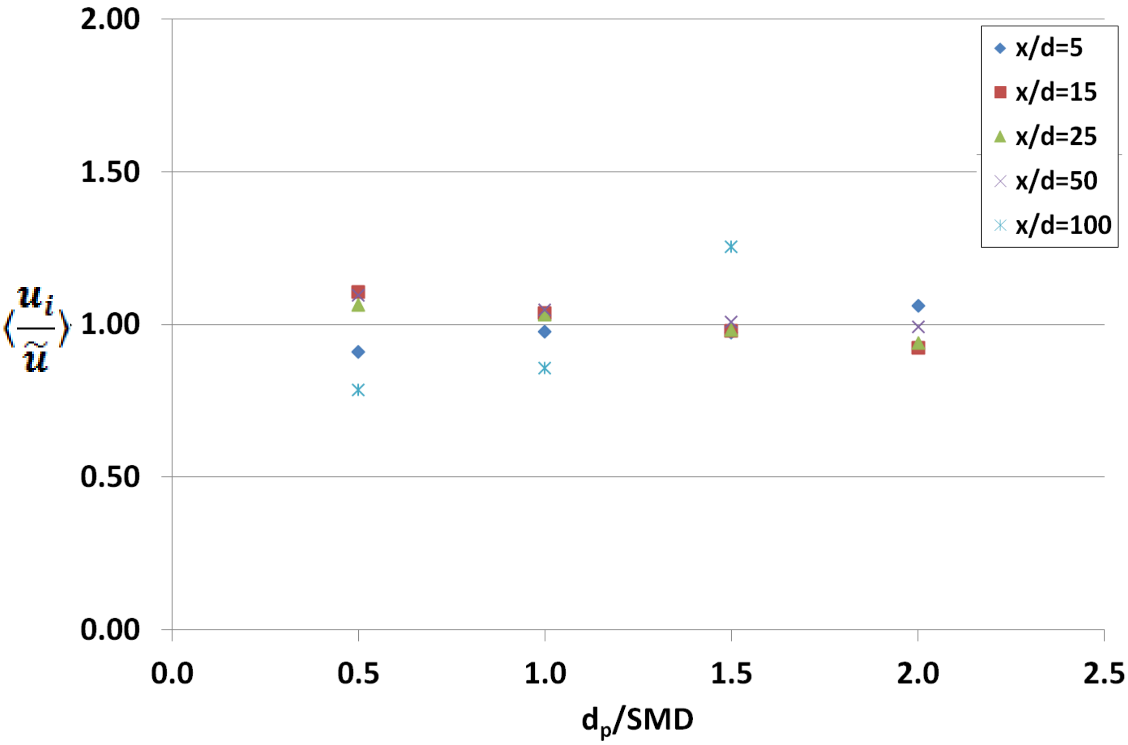

Figure 5.23 Mass Averaged Velocity for Test Case C
(M = 0.3, GLR = 8%, q = 10, d = 1mm).

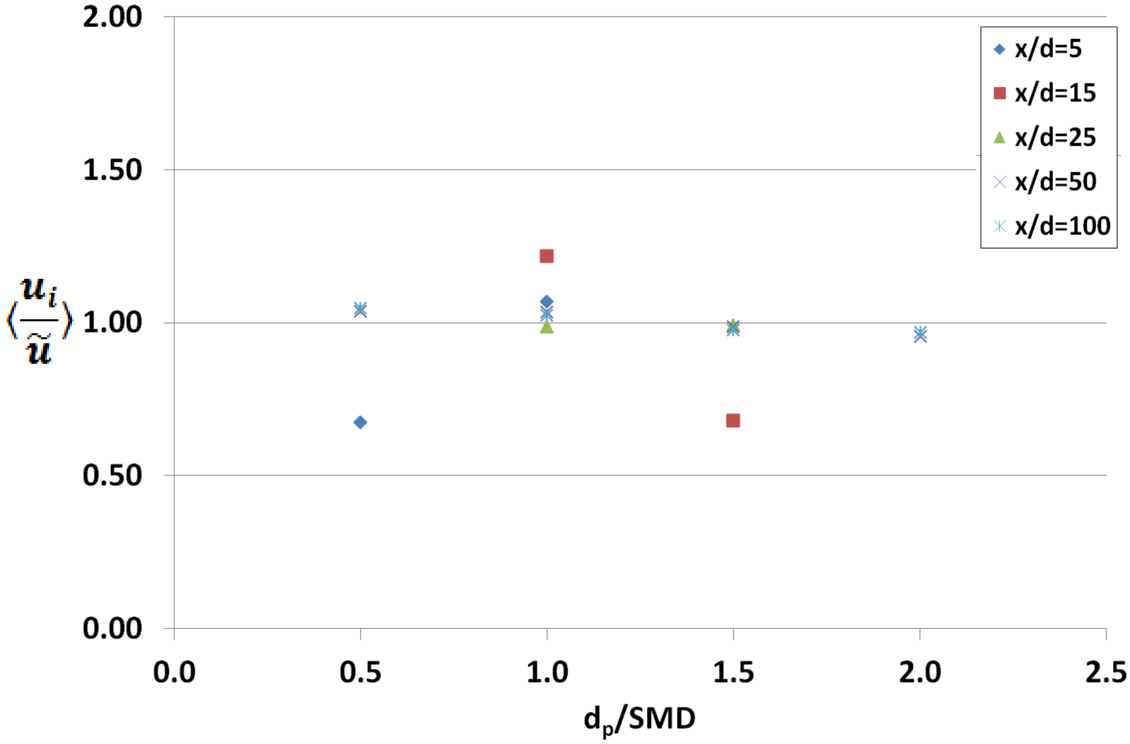

Figure 5.24 Mass Averaged Velocity for Test Case D
(M = 0.6, GLR = 0%, q = 10, d = 1mm).

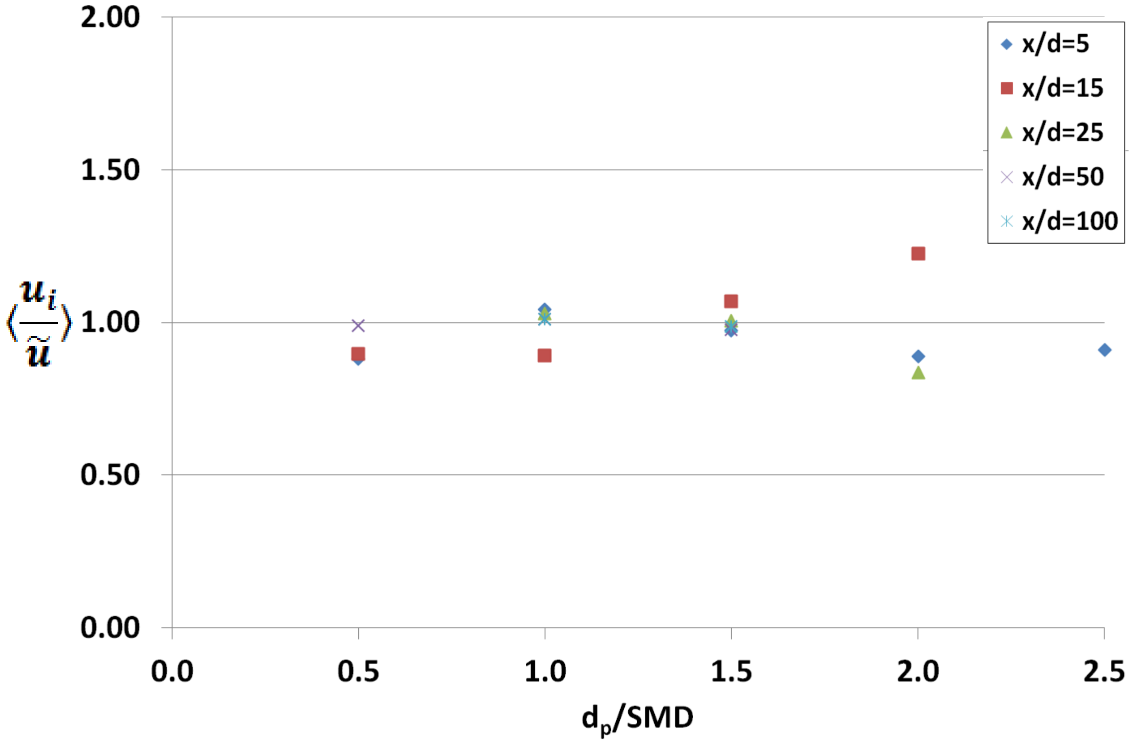

Figure 5.25 Mass Averaged Velocity for Test Case E
(M = 0.6, GLR = 4%, q = 10, d = 1mm).

5.2.3.2 Vertical Mass Averaged Velocity

Here the previous data from the test matrix is re-plotted in Figures 5.26 through 5.30 for the vertical velocity. Again, the rapidly changing nature of the near injector region leads to a wide velocity distribution. But the locations further downstream converge to a single value. Also, because of their inherent momentum, the largest drops are the slowest to take on the freestream velocity value.

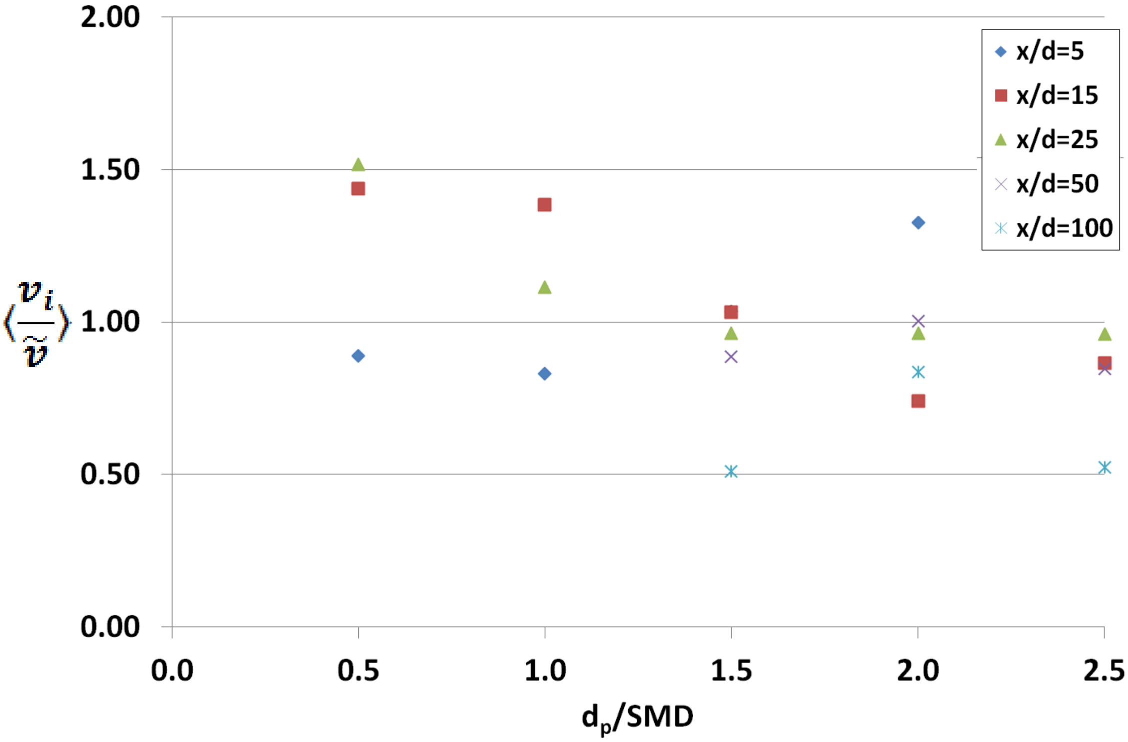

Figure 5.26 Mass Averaged Velocity for Test Case A
(M = 0.3, GLR = 0%, q = 10, d = 1mm).

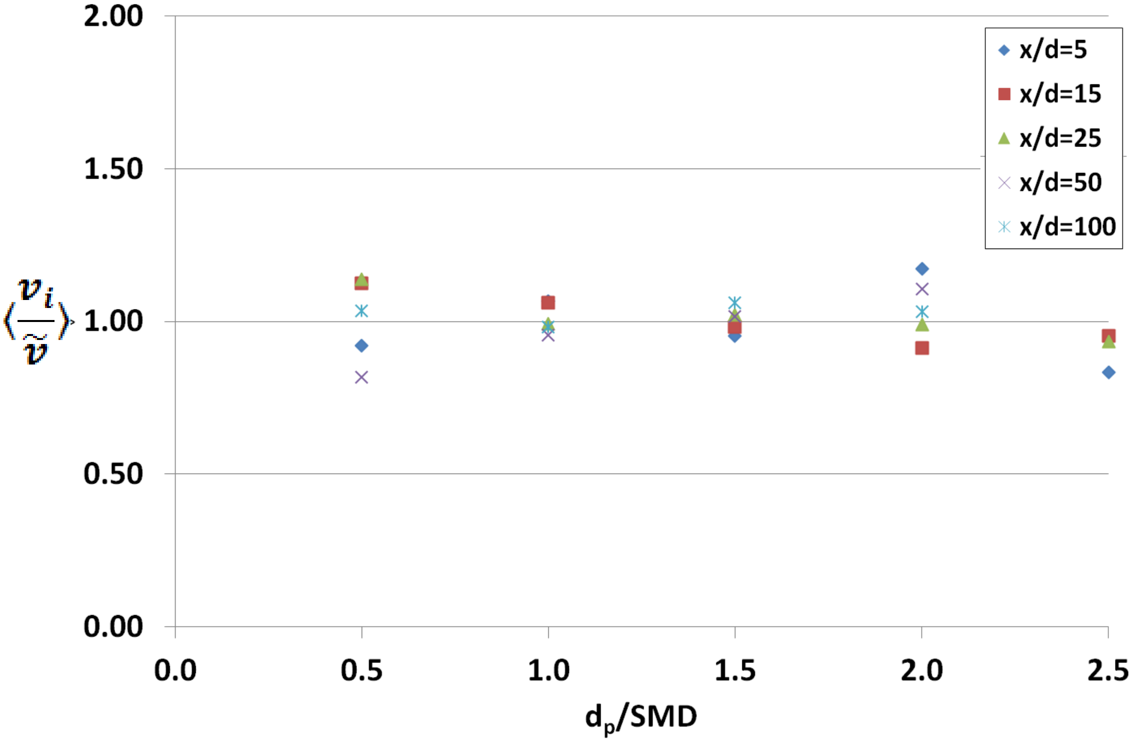

Figure 5.27 Mass Averaged Velocity for Test Case B
(M = 0.3, GLR = 4%, q = 10, d = 1mm).

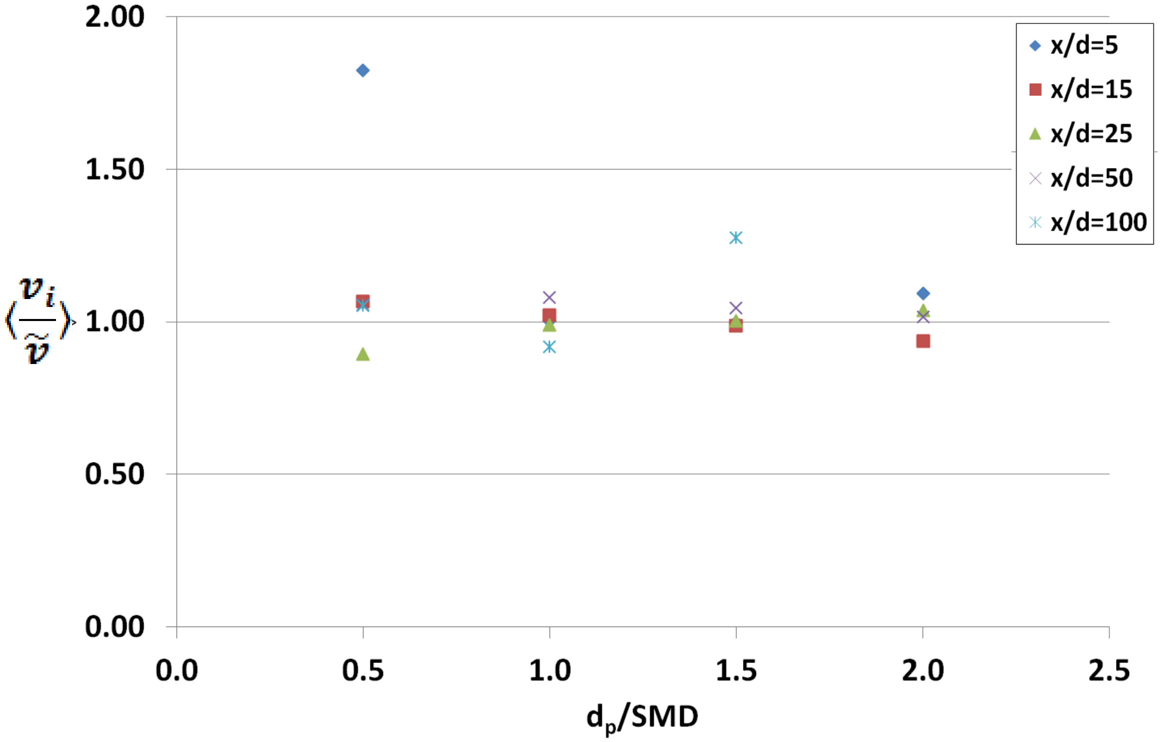

Figure 5.28 Mass Averaged Velocity for Test Case C
(M = 0.3, GLR = 8%, q = 10, d = 1mm).

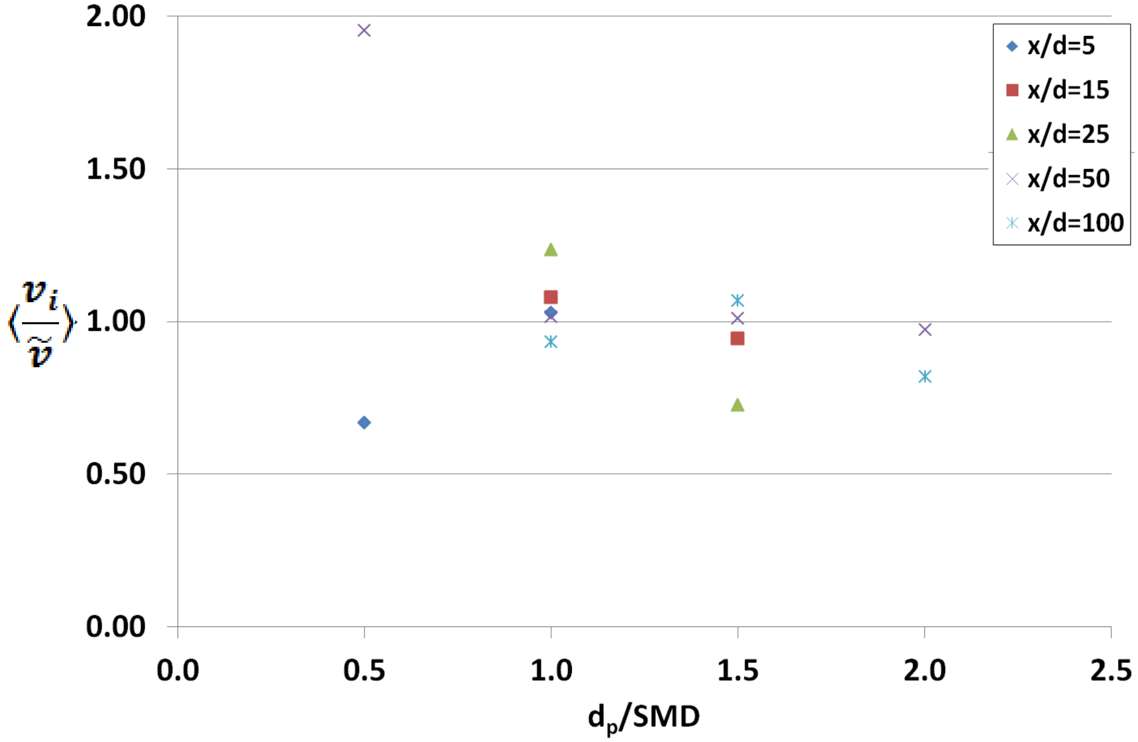

Figure 5.29 Mass Averaged Velocity for Test Case D
(M = 0.6, GLR = 0%, q = 10, d = 1mm).

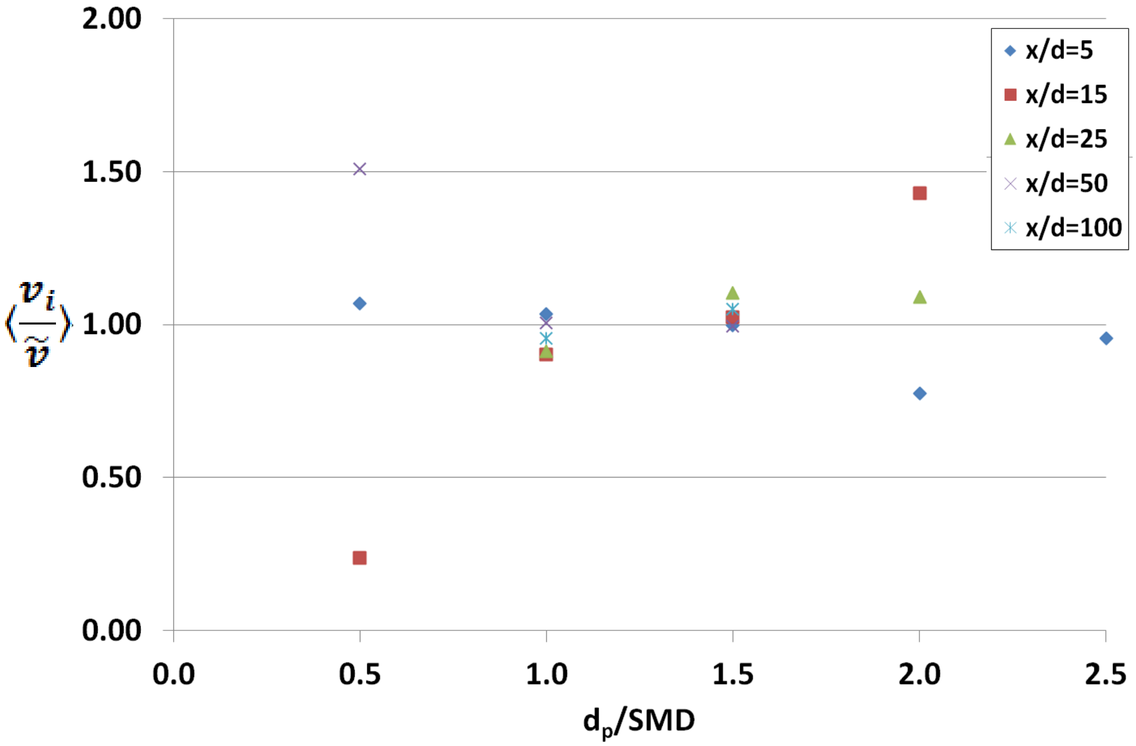

Figure 5.30 Mass Averaged Velocity for Test Case E
(M = 0.6, GLR = 4%, q = 10, d = 1mm).

5.2.3.3 Velocity Distribution by Global Values

The streamwise and vertical velocities evolve with downstream location. Table 5.4 and Figures 5.31 and 5.32 demonstrate the experimental velocity profile at various downstream locations. Each series represents a location from the test matrix. Figure 5.31 gives the mass averaged streamwise velocity normalized by the freestream velocity. At increasing downstream locations (x/d), an increasing percentage of the spray will approach the freestream velocity. As expected n Figure 5.32, the trend is for the vertical velocity to decrease with distance, as the vertical momentum is dissipated.

Table 5.4 Horizontal and Vertical Mass Averaged Velocity Distributions, Normalized by Crossflow Velocity at Downstream Locations.

Test Condition	x/d_j=5		x/d_j=15		x/d_j=25		x/d_j=50		x/d_j=100	
	<ũ/u∞>	<ṽ/u∞>	<ũ/u∞>	<ṽ/u∞>	<ũ/u∞>	<ṽ/u∞>	<ũ/u∞>	<ṽ/u∞>	<ũ/u∞>	<ṽ/u∞>
A(M=.3,GLR=0%)	0.55	0.72	0.74	0.34	0.81	0.27	0.93	0.25	0.92	0.32
B(M=.3,GLR=4%)	0.45	0.67	0.61	0.61	0.71	0.55	0.70	0.70	0.83	0.69
C(M=.3,GLR=8%)	0.44	0.68	0.71	0.73	0.81	0.64	0.78	0.60	0.82	0.69
D(M=.6,GLR=0%)	0.61	0.80	0.48	0.62	0.69	0.50	0.76	0.15	0.90	0.10
E(M=.6,GLR=4%)	0.50	0.88	0.65	0.63	0.68	0.52	0.81	0.29	0.87	0.19

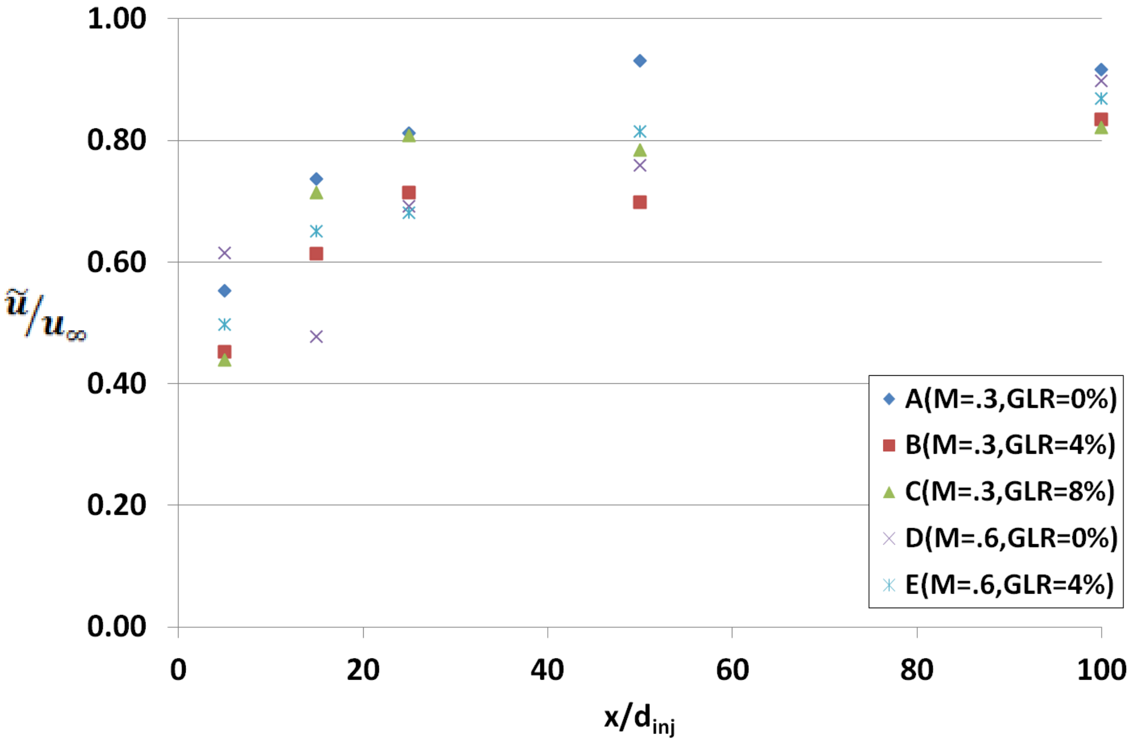

Figure 5.31 Streamwise Velocity Progression.

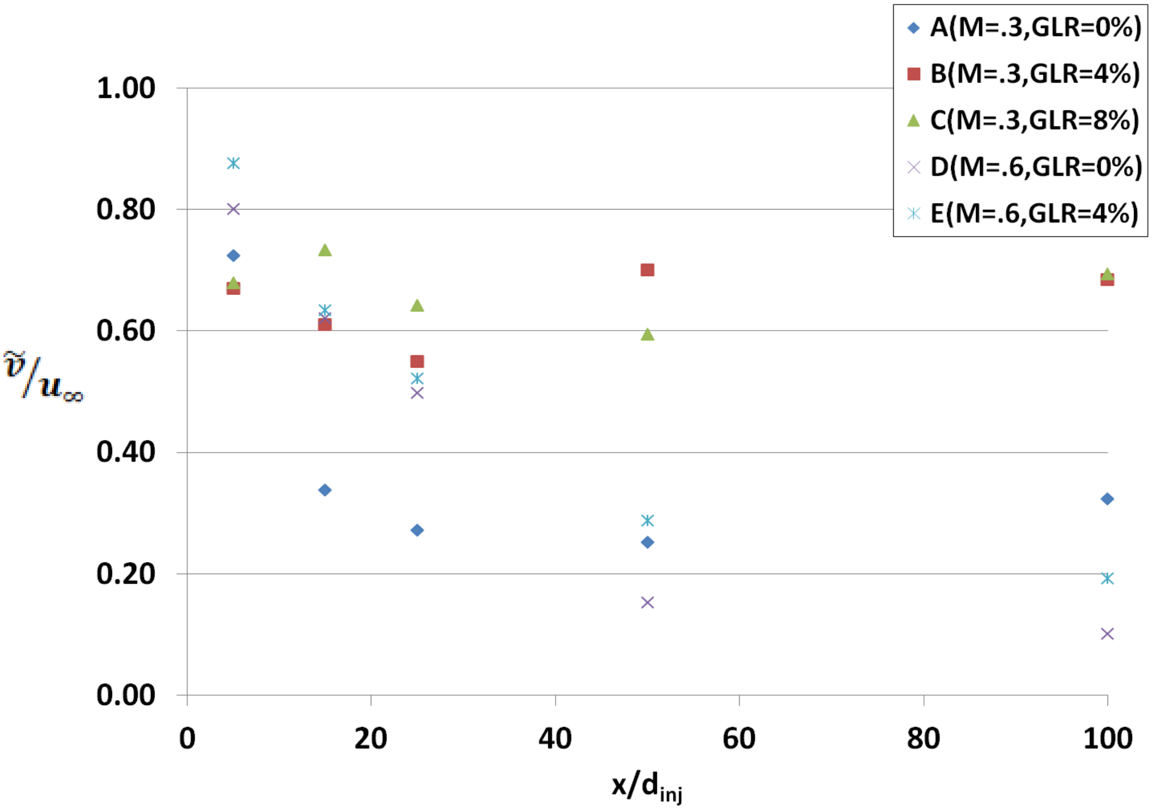

Figure 5.32 Vertical Velocity Progression.

Chapter VI. Conclusions

6.1 Summary

This report has discussed the potential advantages that holography has over other spray diagnostic approaches; namely, holography is a volumetric measure as opposed to a point measurement and drops are not limited to a particular shape. This project has advanced holographic spray analysis by automating the image processing algorithms. Importantly:

- Near field droplet detection within a reconstructed slice has been successfully implemented.
- Advances have been made to locate the droplet's distance from the CCD sensor and to integrate an algorithm for the 3D distribution of droplets.
- The primary thrust was to develop the program so that near field sprays could be studied in a methodical, repeatable manner that would enable the analysis of a large number of holograms.
- Alternatives were assessed to evaluate the optimal algorithm that accurately analyzed the spray hologram with sufficient speed.
- The program error was quantified.
- The success of the approach taken has been demonstrated with graphs of results and tabulated data.

The program was then applied to sprays in a realistic testing environment. Aerated liquid jets (GLR = 0%, 4%, 8%) in a high subsonic crossflow (crossflow Mach number = 0.3 and 0.6) were analyzed, including the rarely investigated near injector region (from the injector to the far field, x/d = 0..100). Usable data was presented in a variety of figures. These results demonstrate that practical 3D analysis of sprays has been pushed well into the near injector region, specifically up to x/d ~ 15. Additional data was obtained even closer to the injector, but its confidence drops significantly.

6.2 Conclusions

The primary conclusions to this project follow the two major thrusts of the work, algorithm development and experimental results analysis.

6.2.1 Algorithm Development

Concerning the computer program and the experiments performed:

- The accuracy of the algorithm is quantified by the drop detection rates:
- false positive rate: FP = 6%
- false negative rate: FN = 20%
- the detection rates are independent of equivalent diameter for drops greater than six pixels (~20μm). A greater laser expansion angle would result in smaller drops for the same six pixel threshold.
- the uncertainty of the equivalent diameter is: $\varepsilon_{deq} / d_{eq} = \pm 17\%$ (see Eqn. 4.17)
- the uncertainty of the spanwise location is: $\varepsilon_{z} / d_{eq} = \pm 2.97$ (see Eqn. 4.18)
- Background subtraction is not worth the investment in processing time or tunnel time for typical holograms. Holography demands such a clean optics setup that the background noise should not be a factor. In near field sprays, the difficulty lies in distinguishing real drops from interfering artifacts that are generated by out of focus drops and nearby interference fringes.
- It is better to use large expansion angles to minimize the out of focus artifacts and use a separate reference beam to strengthen the signal to noise ratio.
- If the required resources and optical access are available, double view holography will be worth the added difficulty. The double views will greatly improve the spanwise accuracy from +/- 3 diameters to less than one. Double view image analysis would also allow a coarser reconstruction interval, potentially cutting overall all processing time. Finally, double views offer an extra check for noise, reducing the number of false positives.

- The image processing approach used on individual reconstructions was to segment the image such that pixels with a value 80% of their backgrounds were treated as possible drops. These locations are then filtered if a neighboring reconstruction is not also a possible drop. This readily vectorizable approach then lends itself to calculating a 3D centroid.

- Alternate methods were investigated for filtering false positive droplets and calculating their 3D location. While the 80% thresholding method was effective given the desire to process a large quantity of images, the FFT filter is very effective if extra accuracy is required.

6.2.2 Experimental Results

Regarding the structures of the aerated liquid jets under investigation:

- The area near the injector floor in the figures are composed of a high number density, wide span of very small droplets separated from the main, high density core. This region immediately downstream of the injector, under the jet core, features a continuous distribution of drops. Hence, while a wake of relatively large drops forms downstream of the injection site, the wake is not completely empty.

- The majority of the spray mass is concentrated at higher penetration heights in the spray field. This trend is evident in all of the test cases.

- Also, the droplet size steadily increases with increasing distance from the wind tunnel floor to the jet central core.

- As the width and the height of the plumes increase (due to decreasing crossflow Mach number or increasing aeration), the number density of fine droplets decreases. Furthermore, no large drops are found in or near the wake.

- The downstream location is important to the Sauter Mean Diameter in the near field; larger drops break up during secondary atomization. However, even with the near field data, the influence of x is much less than GLR or M for the given data set. SMD is inversely proportional to all three factors.

6.3 Recommendations for Future Work

Opportunities exist to further the current work. As with most image processing problems, increasing processing speed will always be an issue. To that end, the algorithm should be extended to run on a dedicated cluster. The program was designed to be inherently parallelizable, and it has been run on parallel mode on multi-core computers; however, it has not been set up on a cluster. To do so would greatly expand the magnitude of possible test matrices.

The algorithm was also designed to incorporate double view holography, and it was demonstrated in test cases. However, “real” experiments on double view near field holography were not available. The spanwise location drop accuracy could be greatly improved by taking advantage of this capability.

The velocity calculations could be improved by increasing the matching rate. The flowfield vector used to calculate expected drop locations could be refined to match regions within the 3D image space. The morphology of drops could be used match drop images, enabling less restrictive size and location criteria. Because of the smaller magnitudes, and fewer pixels traveled, vertical component calculations have higher uncertainty. This could be reduced by using greater expansion angles for the hologram light source.

Finally, additional near field experiments, across a broader test range using Design of Experiments, need to be run to build even more useful correlations. Likewise, with simple adjustments to the hologram reconstruction process, the program could be expanded to analyze other multi-phase systems (i.e. holographic-PIV, micro-scale fluids, particulate flows, bubbles, etc.).

References

- Alfieri, D., Coppola, G., De Nicola, S., Ferraro, P., Finizio, A., Pierattini, G., and Javidi, B. (2006), "Method For Superposing Reconstructed Images From Digital Holograms Of The Same Object Recorded At Different Distance And Wavelength," Optics Communication, Vol. 260, 2006, Pp 113-116.

- Ara, M.H. and Sirohi, R.S. (2006), "Speckle Interferometry Methods for Displacement and Strain Measurements Using Photorefractive Crystal," Optics, *Article In Press.*

- Ashgriz, N. (ed.) (2011), "Handbook of Atomization and Sprays," Springer Science and Business Media, LLC 2011.

- Asundi, A. (2002), MATLAB for Photomechanics: A Primer, Elsevier Science Ltd, Oxford 2002.

- Baldi, P., Brunak, S., Chauvin, Y., Andersen, C.A.F., and Nielsen, H. (2000), "Assessing the Accuracy of Prediction Algorithms for Classification: An Overview," Bioinformatics Review, Vol. 16, no. 5, pp 412-424, 2000.

- Bates, D.M. and Watts, D.G. (1988), "Nonlinear Regression Analysis and Its Applications," Wiley Series in Probability and Mathematical Sciences, New York, 1988.

- Choi, C.W. and Puri, I.K. (2000), "Flame Stretch Effects on Partially Premixed Flames," Combustion and Flame, Vol. 123, 2000 pp 119-139.

- Choi, C.W. and Puri, I.K. (2001), "Contribution of Curvature to Flame-Stretch Effects on Premixed Flames," Combustion and Flame, Vol. 126, 2001 pp 1640-1654.

- Choo, Y.J., and Kang, B.S. (2006), "The Characteristics of the Particle Position Along an Optical Axis in Particle Holography," Measurement Science Technology, Vol. 17, pp. 761-770, 2006.

- Conley, E. and Robillard, J. (1992), Industrial Applications for Optical Data Processing and Holography, CRC Press, Inc., Mexico 1992.

- Corvaro, F. and Paroncini, M. (2006), "Experimental Analysis of Natural Convection in Square Cavities Heated From Below with 2D-PIV and Holographic Interferometry Techniques," Experimental Thermal Fluid Science, doi:10.1016/j.expthermflusci.2006.07.006 (*article in press*).

- Crowe, C., Sommerfeld, M., and Tsuji, Y. (1998), Multiphase Flows with Droplets and Particles, CRC Press, Boca Raton, 1998.

- Demoli, N., Mestrovic, J., and Sovic, I. (2003), "Subtraction Digital Holography," Applied Optics, Vol. 42, No. 5, 2003, pp 798 – 804.

- Dension, D.G.T., Homes, C.C., Mallick, B.K., and Smith, A.F.M. (2002), "Bayesian Methods for Nonlinear Classification and Regression," John Wiley & Sons, Ltd., Great Britain, 2002.

- Elavarasan, R. and Meng, H. (2000), "Flow Visualization Study of Role of Coherent Structures in a Tab Wake," Fluid Dynamics Research, Vol. 27, 2000, pp 183-197.

- Forsyth, D.A. and Ponce, J. (2003), "Computer Vision: A Modern Approach", Prentice Hall, New Jersey, 2003.

- Gabor, D. (1948), "A New Microscope Principle," Nature, Vol. 161, 1948, pp 777-778.

- Garcia-Sucerquia, J., and Ramirez, J., Prieto, D. (2005), "Reduction of Speckle Noise in Digital Holography by Using Digital Image Processing," Optics, Vol. 116, 2005, pp 44-48.

- Gelman, A. and Meng, X.-L., Applied Bayesian Modeling and Causal Inference from Incomplete Data Perspectives, John Wiley & Sons, Ltd., West Sussex, England, 2004.

- Gire, J., Denis, L., Thiebaut, E. Soulez, F., and Ducottet, C. (2008), "Digital Holography of Particles: Benefits of the 'Inverse Problem' Approach," Measurement Science and Technology, Vol. 19, pp. 1-13, 2008.

- Gombkoto, B., Kornis, J., and Fuzessy, Z. (2002), "Difference Displacement Measurement Using Digital Holography," Optics Communications, Vol. 214, 2002, pp 115-121.

- Gonzales, R.C., Woods, R.E., and Eddins, S.L. (2004), Digital Image Processing Using Matlab, Pearson Prentice Hall, New Jersey, 2004.

- Goodman, J.W. (1996), Introduction to Fourier Optics, McGraw-Hill, USA, 1996.

- Grant, I. (1997), "Particle Image Velocimetry: A Review," Proc. Instn. Mech. Engrs., Vol. 211 Part C, pp 55-76.

- Grant, I. and Thompson, B. J. (1999) (eds.) "Selected Papers on Particle Image Velocimetry", SPIE Milestone Series, Vol. MS99, 1999, pp 609-617.

- Hariharan, P. (1992), Basics of Interferometry, Academic Press, Inc., San Diego, 1992.

- Hariharan, P. (2002), Basics of Holography, Cambridge University Press, Cambridge, 2002.

- Hassan, Y. and Blanchat, T. (1999), “Full-Field Bubbly Flow Velocity Measurements by Digital Image Pulsed Laser Velocimetry,” *printed in:* Grant, I. and Thompson, B. J. (editors) Selected Papers on Particle Image Velocimetry, SPIE Milestone Series, Vol. MS99, 1999, pp 609-617.

- Hsiang, L.-P., and Faeth, G.M. (1993), “Drop Properties After Secondary Breakup,” International Journal of Multiphase Flow, Vol. 19, No. 5, pp. 721-735, 1993.

- Jones, A.R., Sarjeant, M., David, C.R., and Denham, R.O. (1978), “Application of In-Line Holography to Drop Size Measurement in Dense Fuel Sprays,” Applied Optics, Vol. 17, No. 3, pp. 328-330, 1978.

- Kastengren, A.L., Powell, C.F., Arms, D., Dufresne, E.M., and Wang, J. (2010), “Spray Diagnostics at the Advanced Photon Source 7-BM Beamline”, ILASS Americas, 22ndAnnual Conference on Liquid Atomization and Spray Systems, Cincinnati, OH May 2010.

- Katz, J., Donaghay, P.L., Zhang, J., King, S., and Russell, K. (1999), “Submersible holocamera for detection of particle characteristics and motions in the ocean,” Deep-Sea Research Part 1, Vol. 46, 1999, pp 1455-1481.

- Kline, S.J. (1985), “The Purposes of Uncertainty Analysis” ASME Journal of Fluids, Vol. 107, pg. 153-160.

- Kreis, T.M., Adams, M., and Jueptner, W.P.O. (1997a), “Methods of Digital Holography: A Comparison,” *SPIE* Vol. 3098, 1997, pp 224-233.

- Kreis, T.M., and Juptner, W.P.O (1997b), “Suppression of the DC Term in Digital Holography,” Optical Engineering, Vol. 36, 1997, pp 2357-2360.

- Lauterborn, W. and Hentschel, W. (1986), “Cavitation Bubble Dynamics Studied by High Speed Photography and Holography: Part Two,” Ultrasonics, March, 1986, pp 59-65.

- Lee, J., Miller, B., Sallam, K.A., and Bingabr, M. (2007), “Digital Double-Pulsed Microscopic Holography Diagnostics for Sprays Using Commercial Grade CCD,” 6th International Conference on Multiphase Flows, ICMF 2007, Leipzig, Germany, July 9-13, 2007, Paper No. 57_Thu_C_54.

- Lee, J., Miller, B., and Sallam, K.A. (2009), “Demonstration of Digital Holographic Diagnostics for the Breakup of Liquid Jets Using a Commercial-Grade CCD Sensor,” *Atomization Sprays*, Vol. 19, 2009, pp. 445-456.

- Leith, E.N. and Upatnieks, J. (1965). "Holograms - Their properties and uses (Hologram photography, principles, techniques and application." SPIE JOURNAL 4: 3-6.

- Lin, K.-C., Kirkendall, K.A., Kennedy, P.J., and Jackson, T.A. (1999), “Spray Structures of Aerated-Liquid Fuel Jets in Supersonic Crossflows,” AIAA Paper 99-2374, June 1999.

- Lin, K.-C., Kennedy, P.J., and Jackson, T.A. (2002), "Penetration Heights of Liquid Jets in High-Speed Crossflows," AIAA Paper 2002-0873, January 2002.

- Liu, H. (1999), Science and Engineering of Droplets: Fundamentals and Applications, Noyes Publications, N.J., 1999.

- Malkeil, E., Abras, J., and Katz, J. (2004), "Automated Scanning and Measurements of Particle Distributions Within a Holographic Reconstructed Volume," Measurement Science Technology, Vol. 15, 2004, pp 301-612.

- Meng, H., Anderson, W.L., Hussain, F., and Liu, D. (1993), "Intrinsic Speckle Noise in In-line Particle Holography," J. Opt. Soc. Am., Vol. 10, 1993, pp 2046-2058.

- MIL-STD-150, "Photographic Lenses", ASSIST Quick Search, https://assist.daps.dla.mil/

- Miller, B.D. (2006), "Digital Holographic Diagnostics of Aerated-Liquid Jets in a Subsonic Crossflow," *Oklahoma State University* Masters Thesis, 2006.

- Miller, B., Sallam, K.A., Lin, K.-C., and Carter, C. (2006), "Digital Holographic Spray Analyzer," Proceedings of FEDSM2006, 2006 ASME Joint U.S.-European Fluids Engineering Summer Meeting, July 17-20, Miami, FL.

- Miller, B., Sallam, K.A., Bingabr, M., Lin, K.-C., and Carter, C. (2008), "Breakup of Aerated Liquid Jets in Subsonic Crossflow," Journal of Propulsion and Power, Vol. 24, No. 2, 2008, pp. 253-258.

- Muller, J., Kebbel, V., and Juptner, W. (2004), "Characterization of Spatial Particle Distributions in a Spray-Forming Process Using Digital Holography," Measurement Science and Technology, Vol. 15, pp. 706-710, 2004.

- Myers, R.H., Montgomery, D.C., and Vining, G.G. (2002), "Generalized Linear Models, with Applications in Engineering and Science," John Wiley, New York, 2002.

- Nelleri, A., Gopinathan, U., Joseph, J., and Singh, K. (2006), "Three-Dimensional Object Recognition from Digital Fresnel Hologram by Wavelet Matched Filtering," Optics Communication, Vol. 259, 2006, pp 499-506.

- Nicolas, F., Coetmellec, S., Brunel, M., and Lebrun, D. (2006), "Digital In-Line Holography with a Sub-picosecond Laser Beam," Optics Communications, Vol. 268, 2006, pp 27-33.

- Ovryn, B. (2000), "Three-Dimensional Forward Scattering Particle Image Velocimetry Applied to a Microscopic Field-of-view," Experiments in Fluids [Supplement], 2000, pp S175-S184.

- Pan, G. and Meng, H. (2003), "Digital Holography of Particle Fields: Reconstruction by Use of Complex Amplitude," Applied Optics, Vol. 42, No. 5, 2003, pp 827-833.

- Pedrini, G. and Tiziani, H.J. (1995), “Digital Double-Pulse Holographic Interferometry Using Fresnel and Image Plane Holograms,” Measurement, Vol. 15, 1995, pp 251-260.

- Pereira, F. and Gharib, M. (2002), “Defocusing Digital Particle Image Velocimetry and the Three-Dimensional Characterization of Two-Phase Flows,” Measurement Science and Technology, Vol. 13, 2002, pp 683-694.

- Palero, V., Arroyo, M.P., and Soria, J. (2007), “Digital Holography for Micro-droplet Diagnostics,” Exp. Fluids, Vol. 43, pp. 185-195, 2007.

- Pu, Y., Cao, L., and Meng, H. (2002), “Fundamental Issues and Latest Development in Holographic Particle Image Velocimetry,” Proceedings of IMECE2002: 2002 ASME International Mechanical Engineering Congress and Exposition, New Orleans, LA, Nov. 17-22, 2002.

- Pu, Y., and Meng, H. (2000), “An Advanced Off-Axis Holographic Particle Image Velocimetry (HPIV) System,” Experiments in Fluids, Vol. 29, 2000, pp 184-197.

- Pu, Y., Song, X., and Meng, H. (2000), “Off-axis Holographic Particle Image Velocimetry for Diagnosing Particulate Flows,” Experiments in Fluids [Supplement], 2000, S117-S128.

- Pu, Y. and Meng, H. (2005), “Four-Dimensional Dynamic Flow Measurement by Holographic Particle Image Velocimetry,” Applied Optics, Vol. 44, No. 36, 2005, pp 7697-7708.

- Rao, S.S. (1996), Engineering Optimization: Theory and Practice, 3rd Ed., John Wiley & Sons, Inc., Toronto, 1996.

- Roth, G., Hart, D., and Katz, J. (1995), “Feasibility of Using the L64720 Video Motion Estimation Processor (MEP) to Increase Efficiency of Velocity Map Generation for Particle Image Velocimetry (PIV),” FED, Vol. 229, 1995, pp 387-393.

- Royer, H. (1977), “Holographic Velocimetry of Submicron Particles,” Optics Communications, Vol. 20, No. 1, January, 1977, pp. 73-75.

- Sallam, K.A., Aalburg, C., Faeth, G.M., Lin, K.-C., Carter, C. and Jackson, T.A. (2006), “Primary Breakup of Round Aerated-Liquid Jets in Supersonic Crossflows”, Atomization and Sprays, Vol. 16, No. 6, pp. 657-672.

- Santangelo, P. J. and Sojka, P.E. (1995). "A holographic investigation of near-nozzle structure of an effervescent atomizer-produced spray." Atomization and Sprays**5**: 137-155.

- Schnars, U. and Jueptner, W. (2005), Digital Holography: Digital Hologram Recording, Numerical Reconstruction, and Related Techniques, Springer-Verlag, Berlin, 2005.

- Sheng, J., Malkiel, E., Katz, J. (2003), “Single Beam Two-Views Holographic Particle Image Velocimetry,” Applied Optics, Vol. 42, 2003, pp. 235-250.

- Sheng, J., Malkiel, E., and Katz, J. (2006), “Digital Holographic Microscope for Measuring Three-Dimensional Particle Distributions and Motions.” Applied Optics, Vol. 45, No. 16, 1 June 2006, pp. 3893-3901.

- Simmons, H.C. (1977), “The Correlation of Drop-Size Distributions in Fuel Nozzle Sprays, Part 1: The Drop-Size/Volume-Fraction Distribution,” Journal of Engineering for Power, pp. 309-314, July 1977.

- Skarman, B., Wozniak, K., and Becker, J. (1999), “Digital In-Line Holography for the Analysis of Bernard-Convection,” Flow Measurement and Instrumentation, Vol. 10, 1999, pp 91-97.

- Soria, J. and Atkinson, C. (2008), “Towards 3C-3D Digital Holographic Fluid Velocity Vector Field Measurement-Tomographic Digital Holographic PIV (Tomo-HPIV),” Measurement Science and Technology, vol 19, pp 1-12, 2008.

- Sovani, S.D., Sojka, P.E., and Lefebvre, A.H. (2001), “Effervescent Atomization,” Progress in Energy and Combustion Science, Vol. 27, 2001, pp. 483-521.

- Taylor, B.N. and Kuyatt, C.E. (1994) “Guidelines for Evaluating and Expressing the Uncertainty of NIST Measurement Results” NIST Technical Note 1297, 1994 Ed., National Institute of Standards and Technology, U.S. Dept. of Commerce, Washington, DC.

- van Hout, R. and Katz, J. (2004), “A method for measuring the density of irregularly shaped biological aerosols such as pollen,” Aerosol Science, Vol. 35, 2004, pp 1369-1384.

- Virant, M. and Dracos, T. (1997), “3D PTV and its Application on Lagrangian Motion,” Measurement Science and Technology, Vol. 8, 1997, pp 1539-1552.

- Xu, W., Jericho, M.H., Kreuzer, H.J., and Meinertzhagen, I.A. (2003), “Tracking Particles in Four Dimensions with In-Line Holographic Microscopy”, Optics Letters, Vol. 28, pp. 164-166.

- Yang, W., Meng, H., and Sheng, J. (2001), “Dynamics of Hairpin Vorticies Generated by a Mixing Tab in a Channel Flow,” Experiments in Fluids, Vol. 20, 2001, pp 905-722.

- Yang, Y., Kang, B.-S., and Choo, Y.-J. (2008), “Application of the Correlation Coefficient Method for Determination of the Focal Plane to Digital Particle Holography,” Applied Optics, Vol. 47, No. 6, pp. 817-824, 2008.

- Zhang, Y., Lu, Q., and Ge, B. (2004), “Elimination of Zero-Order Diffraction in Digital Off-Axis Holography” Optics Communications, Vol. 240, 2004, pp 261-267.

VITA

David Simon Olinger

Candidate for the Degree of

Doctor of Philosophy

Thesis: AUTOMATIC DIGITAL HOLOGRAPHIC ANALYSIS OF NEAR FIELD AERATED LIQUID JETS IN CROSSFLOW

Major Field: Mechanical and Aerospace Engineering

Biographical:

Education:

Completed the requirements for the Doctor of Philosophy in Mechanical and Aerospace Engineering at Oklahoma State University, Stillwater, Oklahoma in May 2012.

Completed the requirements for the Master of Science in Mechanical and Aerospace Engineering at Oklahoma State University, Stillwater, Oklahoma in December 2004.

Completed the requirements for the Bachelor of Science in Mechanical Engineering at Colorado State University, Fort Collins, Colorado in December 2002.

Experience:

Aerospace Engineer at Tinker AFB, Oklahoma since August 2008.

Professional Memberships:

Society of Automotive Engineers

American Society of Mechanical Engineers

American Institute of Aeronautics and Astronautics

Name: David Simon Olinger Date of Degree: May 2012

Institution: Oklahoma State University Location: Stillwater, Oklahoma

Title of Study: AUTOMATIC DIGITAL HOLOGRAPHIC ANALYSIS OF NEAR FIELD AERATED LIQUID JETS IN CROSSFLOW

Pages in Study: 138

Candidate for the Degree of Doctor of Philosophy

Major Field: Mechanical and Aerospace Engineering

Scope and Method of Study:

This report has discussed the advantages that holography has over other spray diagnostic approaches; namely, holography is a volumetric measurement as opposed to a point measurement and drops are not limited to a particular shape. This project has advanced holographic spray analysis by automating the image processing algorithms. The program was then applied to sprays in a realistic testing environment. Aerated liquid jets in a high subsonic crossflow were analyzed, including the rarely investigated near injector region (from the injector to the far field, x/d = 0..100). Usable data was presented in a variety of figures. These results demonstrate that practical 3D analysis of sprays has been pushed well into the near injector region, specifically up to x/d ~ 15. Additional data was obtained even closer to the injector, but its confidence drops significantly.

Findings and Conclusions:

The hologram image processing algorithm has been validated and its uncertainty quantified. The drop detection false positive rate is 6% and false negative rate is 20%. These detection rates are independent of the drop size, for drop images with a diameter greater than six pixels.

The area near the injector floor in the figures are composed of a high number density, wide span of very small droplets separated from the main, high density core. This region immediately downstream of the injector, under the jet core, features a continuous distribution of drops. Hence, while a wake of relatively large drops forms downstream of the injection site, the near-field wake is not completely empty.

The downstream location is important to the Sauter Mean Diameter in the near field; larger drops break up during secondary atomization. However, even with the near field data, the influence of x is much less than GLR or M for the given data set. SMD is inversely proportional to all three factors.

ADVISER’S APPROVAL: Khaled Sallam